Fakultät für Elektrotechnik und Informationstechnik
Technische Universität München

Visual Quality Enhancement in Optoacoustic Tomography

Methods in Multiscale Imaging and Image Processing

Subhamoy Mandal

Vollständiger Abdruck der von der Fakultät für Elektrotechnik und Informationstechnik der Technischen Universität München zur Erlangung des akademischen Grades eines

Doktor-Ingenieurs (Dr.-Ing.)

genehmigten Dissertation.

Vorsitzender:
Prof. Dr.-Ing. Eckehard Steinbach

Prüfende der Dissertation:
Prof. Dr. Vasilis Ntziachristos
Prof. Dr. Jörg Conradt

Die Dissertation wurde am 30.03.2017 bei der Technischen Universität München eingereicht und durch die Fakultät für Elektrotechnik und Informationstechnik am 11.03.2018 angenommen.

सर्वधर्मान् परित्यज्य मामेकं शरणं व्रज
अहं त्वां सर्वपापेभ्यो मोक्षयिष्यामि मा शुचः

Arthashrayatvam shabdasya
drashtur lingatvam eva ca
tan-matratvam ca nabhaso
lakshanam kavayo viduh ...

"Persons who are learned and who have true knowledge define sound as that which conveys the idea of an object, indicates the presence of a speaker and constitutes the subtle form of ether. (Translation)"

– Srimad Bhagavatam (3.26.33)

Abstract

Optoacoustic (or photoacoustic) imaging can simultaneously deliver anatomical, functional and molecular information with unprecedented spatio-temporal resolution and deep-tissue imaging capabilities. To quantitatively recover maps of the local optical absorbance using optoacoustic imaging, multiple parameters related to both light and ultrasound propagation characteristics of the medium need accurate calibration. The dissertation brings together diverse domains of imaging physics and multiscale image processing to achieve improved optoacoustic imaging performance in terms of automation and accurate reconstruction, better mapping of optical and acoustic parameters and improved resolution. Specifically, algorithms for automatic speed-of-sound calibration in cross-sectional optoacoustic tomography were investigated and efficient hybrid focusing metrics for enhancing the focusing performance were designed. An entropy maximization based non-negative constraint was developed, which enables accurate representation of the optoacoustic reconstructions. Further, multi-resolution and scale-space based signal-processing techniques were employed for optoacoustic image segmentation to improve the accuracy of the image reconstruction routines. The image resolution was improved with an innovative geometric pixel super-resolution method, which integrates information from multiple optoacoustic images acquired at sub-diffraction steps into one high-resolution image by means of an iterative registration algorithm. The developed algorithms address the common goal of improving the *visual image quality* of optoacoustic images, using computer vision and image analysis techniques. Extensive experimentation has been performed on target phantoms as well as on *ex vivo* and *in vivo* tissue samples in order to validate the developed methods. In particular, the application of these methods in two biomedical imaging case studies was demonstrated, i.e. for *in vitro* fertilization and intravital imaging in oncology.

Significant improvements in optoacoustic image quantification and resolution enhancement was demonstrated without introducing major alterations into the signal acquisition hardware or inversion algorithms. Overall, the innovations introduced in this work are expected to be instrumental in aiding the interpretation of optoacoustic images and enhancing its powerful features, which can help in the translation of this technology from the laboratory to clinical practice.

Zusammenfassung

Die optoakustische (oder photoakustische) Bildgebung kann gleichzeitig anatomische, funktionale und molekulare Informationen mit beispielloser räumlich-zeitlicher Auflösung und tiefen Gewebe-Imaging-Fähigkeiten liefern. Zur quantitativen Wiederherstellung von Karten der lokalen optischen Absorption mittels optoakustischer Bildgebung benötigen mehrere Parameter, die sowohl die Licht- als auch die Ultraschallausbreitungseigenschaften des Mediums betreffen, eine genaue Kalibrierung. Die Dissertation vereint vielfältige Domänen der Bildgebungsphysik und der multiskalen Bildverarbeitung, um eine verbesserte optoakustische Bildgebungsleistung in Bezug auf Automatisierung und genaue Rekonstruktion, eine bessere Abbildung optischer und akustischer Parameter und eine verbesserte Auflösung zu erzielen. Speziell wurden Algorithmen zur automatischen Geschwindigkeits-Klang-Kalibrierung in der Querschnitts-Optoakustischen Tomographie untersucht und effiziente hybride Fokussierungs-Metriken zur Verbesserung der Fokussierleistung wurden entworfen. Eine Entropie-Maximierung basierte nicht-negative Einschränkung wurde weiterentwickelt, was eine genaue Darstellung der optoakustischen Rekonstruktionen ermöglicht. Ferner wurden für die optoakustische Bildsegmentierung Multifunktions- und skalenraumbasierte Signalverarbeitungstechniken verwendet, um die Genauigkeit der Bildrekonstruktionsroutinen zu verbessern. Die Bildauflösung wurde mit einem innovativen geometrischen Pixel-Super-Auflösungsverfahren verbessert, das Informationen aus mehreren in Unterbeugungsschritten erfassten optoakustischen Bildern in ein hochauflösendes Bild mittels eines iterativen Registrierungsalgorithmus integriert. Die entwickelten Algorithmen befassen sich mit dem gemeinsamen Ziel, die visuelle Bildqualität von optoakustischen Bildern zu verbessern, indem sie Computerbild- und Bildanalysetechniken verwenden. Umfangreiche Experimente wurden sowohl an Zielphantomen als auch auf Ex vivo und in vivo Gewebeproben durchgeführt, um die entwickelten Methoden zu validieren. Insbesondere wurde die Anwendung dieser Methoden in zwei biomedizinischen Imaging-Fallstudien gezeigt, d.h. für die In-vitro-Fertilisation und die intravitale Bildgebung in der Onkologie. Signifikante Verbesserungen in der optoakustischen Bildquantifizierung und Auflösungserhöhung wurden gezeigt, ohne wesentliche Änderungen in die Signalerfassungshardware oder Inversionsalgorithmen einzuführen. Insgesamt werden die in dieser Arbeit eingeführten Innovationen dazu beitragen, die Interpretation optoakustischer Bilder zu unterstützen und ihre kraftvollen Funktionen zu verbessern, die bei der Übersetzung dieser Technologie vom Labor bis zur klinischen Praxis helfen können.

Acknowledgements

My PhD thesis is a culmination of a long journey from being school kid with a fervent curiously to understand the state of nature, to a (almost) independent researcher who can engineer new solutions for improving medical imaging. During this period stretching over a decade. I have encountered several wonderful souls who have showed me the roadmap and guided me along, sometimes even distracted a bit - but all of their contributions have been vital in my genesis and I owe all of them my sincerest gratitude. As much as I would like to tell the long story, I need to limit to the ones who specially influenced my last four years of existence as a doctoral candidate.

First and foremost I would like to thank my supervisors, Prof. Dr. Daniel Razansky, and Prof. Dr. Vasilis Ntziachristos. It has been an privilege to work with the Prof. Razansky as his Ph.D. student. He has not only taught me about optoacoustics but also successfully guided me to obtain the DAAD fellowship to fund my research. I appreciate his support, encouragement and guidance to make my Ph.D. experience productive and fulfilling. I would thank Prof. Ntziachristos for hosting me at the institute and providing the excellent facilities and support which made the thesis possible. I would like to express my sincere gratitude towards the members of Multiscale Functional and Molecular Imaging Laboratory, a group of dynamic young researchers whose participation and comments provided the intellectual ingredients for the projects. I attribute lots of my technical knowledge gained to Xose Luis Dean-Ben, Steven Ford and Jayaprakash.
Interdisciplinary research is often made possible by a group of helpful collaborators, as in the case of my thesis, and i am indebted to them. In regards to the technical collaborations, I must mention the methods for non-negative and generalized image reconstruction developed under the leadership of Jayaprakash, and the development of a framework for pixel super-resolution with Hailong He and Andreas Bühler. For the collaborative projects, I thank Vladimir Ermolayev for his support in the cancer studies, Rahul Dutta and Amy Lin for coordinating the investigative studies to establish optoacoustic imaging as an non-destructive imaging method for in-vitro fertilization practice. Further, I applaud the support and contribution from out corporate partner, iThera Medical with special mention to Elena Nasanova and Neal Burton who are also my co-authors. I am lucky to have wonderful friends and philosophers in Yury, Sandy, Hrushikesh, Supriya, Vishnuvardhan, Karthick, Ruhi, Vipul and Kristen who supported me at various stages of the dissertation.
I thank the thesis reviewers and examiners for critically reviewing the manuscripts and checking the integrity of the work, which enriched the work greatly.
Finally, I offer my humble regards to my parents and love for my sister, who are the driving force behind my quest into science and technology, and have stood beside me in rain and in shade.

Contents

1 Introduction

Optoacoustic (OA) imaging is a noninvasive, nonionizing imaging technique based on the photoacoustic effect, and has emerged as a leading new hybrid bioimaging modality. In OA imaging acoustic waves are generated by the absorption of a short pulsed electromagnetic waves, and the produced acoustic waves are detected using acoustic sensing elements (e.g. Piezoelectric detectors, hydrophones, micro-machined detectors etc.). The term optoacoustic (or photoacoustic) imaging is generally used when one uses visible or near infrared light pulses [1], while using electromagnetic waves in the radio-frequency or microwave range is referred to as thermo-acoustic imaging. So far, the research efforts in OA have been directed towards the development of new hardware components and inversion methodologies allowing increase in imaging speed, depth and resolution, as well as on investigating potential biomedical applications. The unique capabilities of the recently developed whole-body small animal scanning systems (InVision TF-256, iThera GmbH) [2] and volumetric scanners has opened up the unexplored domain of post-reconstruction image analysis. The aim of the current dissertation is to use image analytics in conjunction with imaging and inversion techniques to recover better OA images and enable optimized workflows for biological, pre-clinical and translational imaging.
OA imaging not only provides structural but also functional information of biological tissues [3]. Improving upon the OA imaging (single laser wavelength) technique, Multi-Spectral Optoacoustic Tomography (MSOT) was developed by irradiating a tissue with pulsed light of time-shared multiple wavelengths and establishing transient photon fields in tissue[4]. The state-of-the-art MSOT scanners are now capable of high resolution three dimensional (3D) visualizations of molecular probes located deep in scattering living tissues, with resolution and speed representative of ultrasound [5]. This method can simultaneously deliver anatomical, functional and molecular information with both high resolution and penetration capabilities.

1.1 Development of Optoacoustic imaging

History of the genesis

Shãbda-brahman embodies the transcendental or the supreme sound, which is manifested as an entity which has innate power to convey a particular sense or meaning. Though

Parts of this chapter have been adopted from the tutorial article : **S. Mandal**, X. L. Dean-Ben, N. C. Burton and D. Razansky, "Extending Biological Imaging to the Fifth Dimension: Evolution of volumetric small animal multispectral optoacoustic tomography.," in *IEEE Pulse*, vol. 6, no. 3, pp. 47-53, May-June 2015.

the ancient Rigvedas had hinted at the interplay of sound and light, the modern scientific discovery of photoacoustic effect came as early as 1880, when it was demonstrated by Alexander Graham Bell through his invention of the photophone. In his famous Boston presentation he illustrated how sound can be generated by focusing shuttered sunlight onto a selenium cell. Despite the ancient discovery of the basic physical phenomenon underlying OA imaging and tomography [1], the lack of suitable laser sources, ultrasound detection technology, data acquisition and processing capacities had long hindered realization of efficient imaging devices. In fact, first high-quality images from living animals were obtained about a decade ago, which was followed by an exponential growth of technical developments in instrumentation, algorithms and biomedical applications surrounding this fascinating field (Fig 1.1) [6]. The ability of OA to probe optical

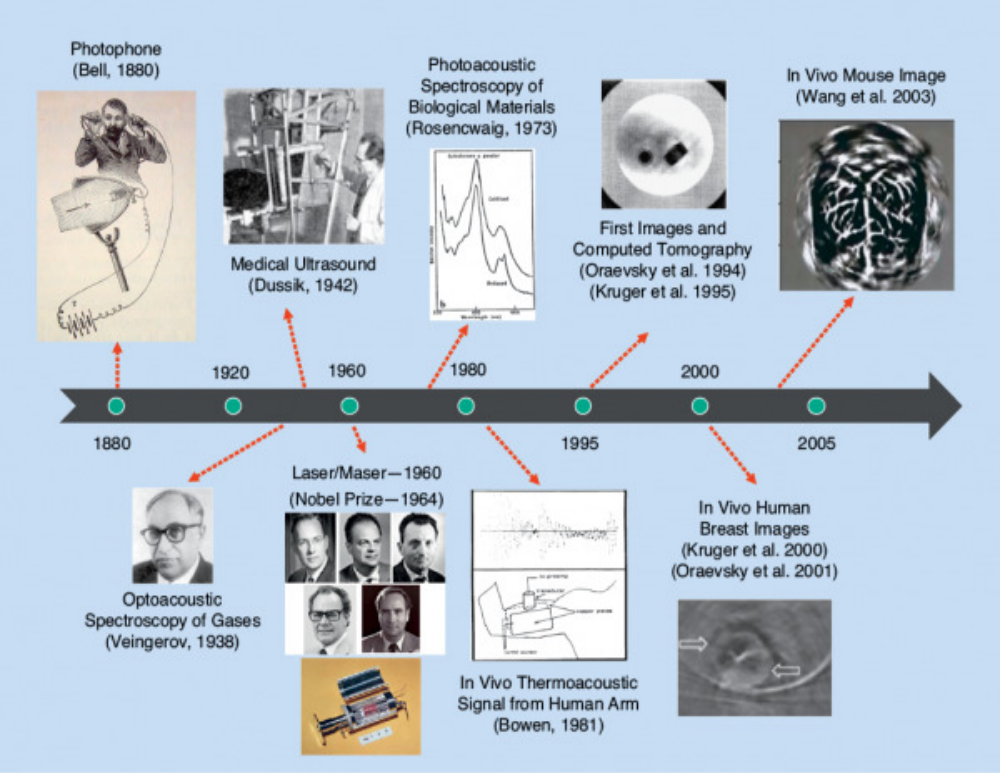

Figure 1.1: A historical time line of the development of optoacoustic imaging technology. (Images in the time line reprinted courtesy of AAAS, AAPM, the IEEE, Nobel Media AB, NPG, RSNA, and the Wellcome Library for the History and Understanding of Medicine.) *Reprinted with permissions from* [6]

contrast along a wide domain of penetration scales while maintaining excellent spatio-temporal resolution representative of ultrasound imaging is unparallel among the other optical imaging modalities [5, 7]. State-of-the-art implementations of MSOT are based on multi-wavelength excitation of tissues to visualize specific molecules located deep within opaque living samples, which further allows to simultaneously deliver anatomical, func-

tional and molecular information from depths of several millimeters to centimeters in scattering tissues (as shown in Fig 1.2). Thereby, MSOT has been widely employed for

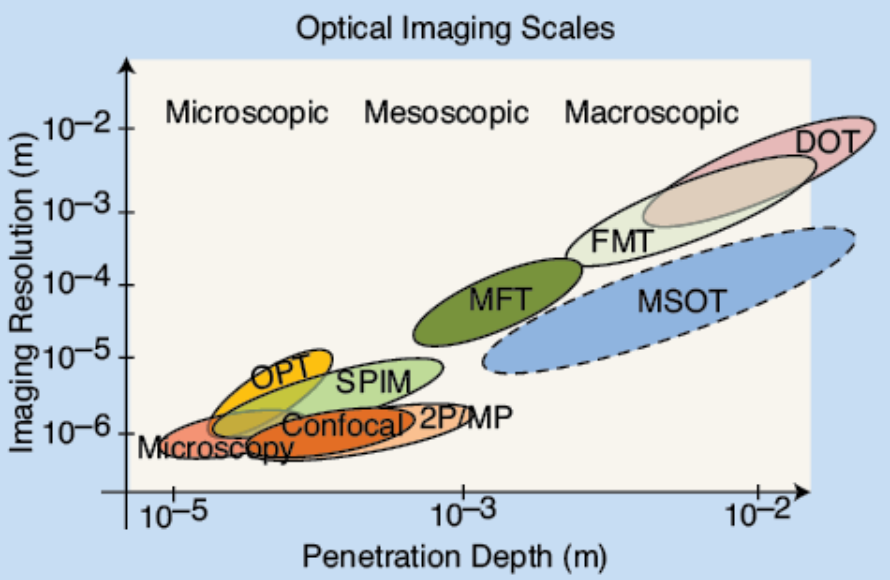

Figure 1.2: The penetration depth and resolution of modern photonic imaging techniques. For living tissues, the methods at the left of the graph are primarily limited by light scattering, whereas the methods to the right are primarily limited by light attenuation in tissue, a parameter that depends on both absorption and scattering, or by ultrasound attenuation. Note that optical projection tomography (OPT) and selective plane illumination microscopy (SPIM) can operate deeper than the range shown in naturally transparent or chemically cleared samples. (2P/MP: two-photon/ multiphoton microscopy; DOT: diffuse optical tomography; FMT: fluorescence molecular tomography; MFT: mesoscopic fluorescence tomography.)

pre-clinical imaging, including in models of cancer, neurodegenerative and cardiovascular diseases, functional neuroimaging, kinetic and biodistribution studies, lymph node staging, imaging of arthritis and inflammation. The main intrinsic tissue contrast at the visible and near-infrared wavelengths stems from the highly absorbing blood hemoglobin, however other major tissue chromophores, such as melanin and fat also have shown to yield spectroscopic OA contrast. Moreover, a large variety of photo-absorbing probes are explored as contrast agents for attaining specific extrinsic contrast. Altogether, these key advantages have prompted development of high throughput MSOT imaging systems for *in vivo* whole-body small animal imaging, further providing high sensitivity and spatial resolution, portability, as well as real time operation capacity.
Small animal *in vivo* imaging is crucial in pre-clinical research to study changes in organs at the cellular and molecular level – shedding light on the frontier of biomedical and pharmaceutical imaging research [8]. An ever growing number of scientific articles related to small animal OA imaging attests, above all, that MSOT is emerging as a preferred non-invasive whole body small animal imaging modality for a number of key applications. The new realm of 5-dimensional imaging, which consists of the 3 spatial

dimensions, the time and the spectral (optical wavelength) dimension, has revolutionized the modern functional and molecular imaging by using the synergistic combination of ultrasound- and light-related advantages, such as high spatio-temporal resolution and powerful spectrally-enriched contrast [9].

The theoretical and physical basis

The photoacoustic effect refers to the induction of acoustic radiation following temperature elevation caused by absorption of light radiation in matter [10]. The OA signal can be generated by various methods, e.g. pulsed laser sources (time-domain) [11], using modulated continuous wave sources (frequency domain) [12], or by wavelength modulated diode lasers [13]. The magnitude of the acoustic wave created by light absorption is proportional to the local light intensity, optical absorption coefficient, and thermoelastic properties of the imaged tissue. The induced acoustic wave spectrum is mainly dependent upon the spatial frequency of optical absorption variations and duration of the light pulse. In most of the current systems used the laser pulse durations in the nanosecond range ($8 - 20ns$), the spectrum of optoacoustically induced signals from biological materials is typically of ultrawideband nature with useful information present in the ultrasonic spectrum between several hundreds of kilohertz and several tens of megahertz [14].

For the OA signal generation we assume the conditions of heat confinement, i.e., the thermal diffusion is insignificant during the pulse given the pulse length is short enough (typically 10s of nanoseconds). Given such boundary condition, the spatiotemporal dependence between thermoacoustically induced pressure $p(\vec{r}, t)$, absorbed energy density $H(\vec{r}, t)$ in W/m^3, and local temperature elevation $T(\vec{r}, t)$ can be expressed in a form of the OA equation [15],

$$\frac{\partial^2 p}{\partial t^2} - c^2 \rho_m \nabla \cdot \left(\frac{1}{\rho_m} \nabla p \right) = \rho_m \beta \frac{\partial^2 T}{\partial t^2} = \frac{\beta}{C_T} \frac{\partial H}{\partial t} \tag{1.1}$$

where c, ρ_m, β, and C_T are the corresponding speed of sound, mass density, isobaric volume expansion, and specific heat coefficients of the medium, respectively. In biological tissues the values of the parameters have very less variations, except for bones, lungs, and other air-containing body cavities. Laser pulses with duration lower than 1 μs can suitably fulfil the thermal confinement criterion and guarantee that the acoustic sources created in the object are proportional to the absorbed optical energy [16]. By representing the absorbed energy density as a product between its spatial and temporal components, i.e., $H(\vec{r}, t) = H_r(\vec{r}) H_t(t)$, while assuming acoustically homogenous medium, (1.1) takes the form of,

$$\frac{\partial^2 p}{\partial t^2} - c^2 \nabla^2 p = \frac{\beta}{C_T} H_r \frac{\partial H_t}{\partial t}. \tag{1.2}$$

OA imaging is a time-resolved modality reminiscent of ultrasound imaging, i.e., time of arrival of the (initial) pressure wave directly indicates the distance to the (acoustic) source in the imaged object. Thus, to enable better sensing and imaging, we place the

ultrasonic detectors in the vicinity of the imaged object (as shown in 1.3). In most practical cases, the duration of the optical pulse is short enough to be approximated by a delta function, i.e., $H_t(t) = \delta(t)$. This simplification leads to an analytical solution of Eq. 1.2, providing expression for the integrated pressure wave $p(\vec{r}', t)$ sensed by a acoustic detector located at $\vec{r}'$, given via a Poisson-type integral [17],

$$p\left(\vec{r}', t\right) = \frac{\beta}{4\pi c^2 C_T} \frac{\partial}{\partial t} \int_{R=ct} \frac{H_r\left(\vec{r}\right)}{R} dA \tag{1.3}$$

where $R = \mid r - r' \mid$ and, for each time point t, the spatial integration is performed over a spherical shell with a radius of $R = ct$ (see Fig. 1.3).

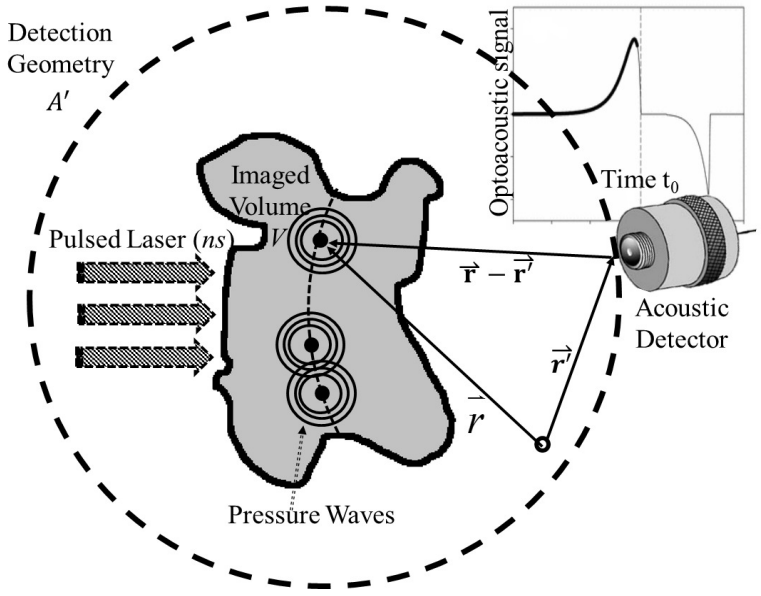

Figure 1.3: Schematic representation of optoacoustic signal detection

A more detailed discussion of the image reconstruction methods and the mathematical framework of OA inverse problem is included in Sec 2.1.

Dimensionality in Optoacoustic imaging

A large variety of approaches have been proposed for *in vivo* small animal OA imaging. Naturally, a single OA waveform represents one-dimensional information along the axis of the ultrasound detection element. Thus, two- or three-dimensional images can be rendered by raster scanning the detector in the two remaining spatial dimensions, as performed in acoustic or optical resolution OA microscopy [18]. Another technique consists in scanning an optical probe beam along a Febry-Pérot interferometric film to tomographically detect optoacoustically generated sound using an all-optical approach [19]. An alternative method for whole-body OA tomography was reported by Brecht et al.[20], which was able to render the three-dimensional distribution of vascular structures

and blood-rich organs such as the liver, spleen, and kidney by rotating a matrix array transducer around the imaged mouse. The real-time imaging capacity in whole-body observations was demonstrated by a cross-sectional MSOT system based on an array of cylindrically focused transducers [21]. This imaging geometry enabled capture of two-dimensional slices representing an entire cross section of living mouse at video rate (see Fig 1.4, configuration shown in Fig 1.4(a)) [22, 2].

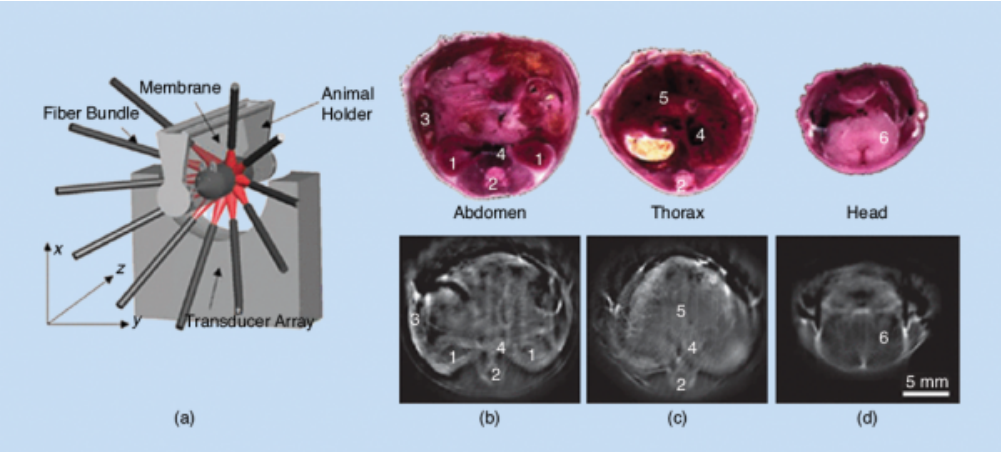

Figure 1.4: (a) A schematic drawing of the cross-sectional MSOT system. A curved array of wideband and cylindrically focused ultrasound transducers enables parallel data acquisition. Optical fibers are used to homogeneously illuminate the object. (b)–(d) MSOT images of mouse anatomy taken at 750 nm. 1: kidneys; 2: spine; 3: spleen; 4: vena cava; 5: liver; and 6: brain.*(Figure adapted in parts from [2])*

The capabilities of OA imaging were extended to four-dimensional imaging (three spatial dimensions + time) through the implementation of the spherical arrays of detectors [2, 23]. Finally, the recently developed portable spherical array probe, combined with a fast wavelength tuning laser, real-time data acquisition, graphics processing unit (GPU)-based volumetric image rendering, and spectral unmixing, has enabled for the first time volumetric real-time spectrally enriched (five-dimensional) OA imaging at centimeter-scale depths [24]. This portable system allows for convenient (handheld) handling of both preclinical experiments and clinical measurements in human subjects [25]. The utility of the five-dimensional imaging approach can be further enhanced by tracking the kinetics and biodistribution of contrast agents with unique absorption spectra [26, 27], such as the U.S. Food and Drug Administration (FDA) approved Indocyanine green (ICG) dye that can be employed during *in vivo* studies to visualize vasculature [23], excretion through the liver or clearing through kidney, and retention in tumors [28].

The temporal dimension

MSOT is based on the detection of acoustic signals created through the thermoelastic expansion of tissue under the influence of light, which is subject to three orders of magnitude less scattering per unit length in tissue as compared to ultrasound. Thereby, the

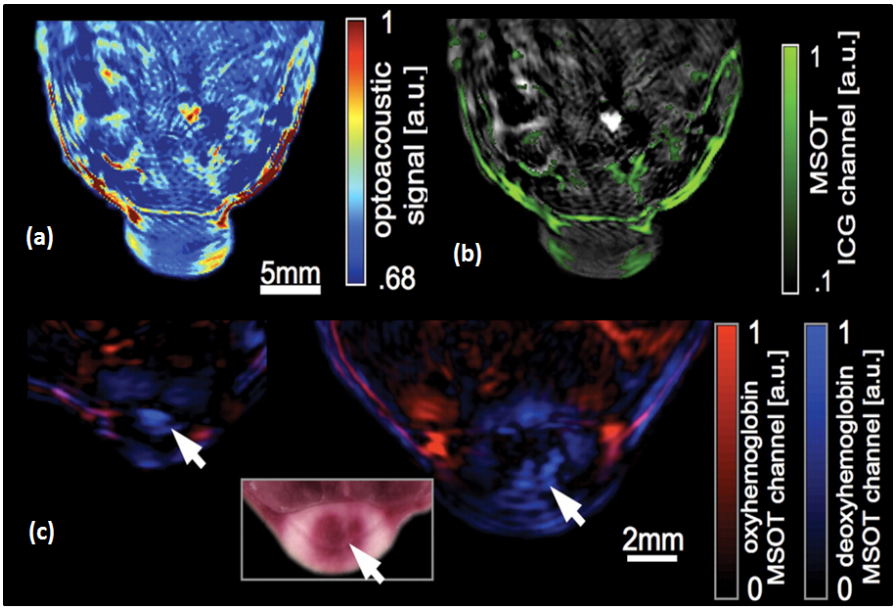

Figure 1.5: Dynamic contrast enhancement in nude mice with 4T1 tumor. (a) Single-pulse images obtained at 790 nm approximately 30 sec after ICG injection, the (b) multispectrally resolved ICG signal is overlayed in green (right). The spectrally resolved oxyhemoglobin (red) and deoxyhemoglobin (blue) within the tumor on days 6 (left) and 13 (right) demonstrate the label free imaging capabilities of MSOT. Insert shows a photograph of the cryoslicing through tumor, arrows indicate hypoxic regions of the tumor core. *Reprinted with permissions from* [23]

spatial resolution is significantly higher than that of diffuse optical imaging techniques [29]. Imaging the distribution of light absorbers in three dimensions with high resolution is, however, not the only asset of MSOT. Indeed, other imaging dimensions may provide independent information regarding the imaged object.
Time represents a key dimension in imaging technologies, although it is often overshadowed by the spatial resolution performance of the modality as the latter is held responsible for "nice-looking images." Yet, it is the high imaging speed that may enable artifact-free handheld imaging [30], visualization of a beating heart [31], or real-time imaging of perfusion profiles in tumors [28] and the internal organs (e.g., the kidneys and brain) of small animals [9]. Fast imaging performance is greatly supported by the development of suitable algorithmic software capable of performing inversion and image/signal processing in real time, which is key for the successful implementation of four- and five-dimensional OA imaging. To this end, the use of Graphics processing units (GPU) has enabled visualization at frame rates of tens of volumes per second.

Optical wavelengths

Multispectral (or multicolor) imaging confers molecular specificity and, thus, provides the capability to quantitatively investigate biological conditions such as hypoxia and nutritional gradients as well as cell viability, proliferation, and drug response potentials.

These parameters are essential in understanding the dynamics of living tissues and disease prognosis and progression (as shown in 1.5). In multispectral imaging, different wavelengths are used for illuminating the tissue in a time-shared fashion [26]. Fast-tuning optical parametric oscillator (OPO)-based lasers enable an entire multispectral scan to be performed in a subsecond time frame, where the wavelengths are chosen in a way to best sample the absorption spectrum characteristics of the specific chromophores and the contrast agent of interest. Spectral unmixing algorithms are then required to isolate the contributions of the individual chromophore(s) of interest to the OA signals representing the distribution of the total absorbed energy.
Multispectral imaging is based on tissue excitation at multiple optical wavelengths. For a given wavelength, the absorbed optical energy corresponds to a linear combination of the absorbed energy of all absorbing substances (chromophores) present in the sample, i.e.,

$$H\left(r', \lambda\right) = \sum_{i} \Phi\left(r'\right) \varepsilon_i\left(r'\right) C_i\left(r'\right) \tag{1.4}$$

where $\varepsilon_i\left(r'\right)$ and $C_i\left(r'\right)$ are the molar extinction coefficient and molar concentration of each chromophore. Spectral unmixing consists in estimating the spatial distribution of the concentrations of different chromophores from the OA images acquired at different wavelengths. For example, this can be achieved by considering images at different wavelengths, Eq. 1.4 can be expressed in a matrix form as,

$$\mathbf{H_{msot}} = \mathrm{E}\mathbf{C}, \tag{1.5}$$

where E is the linear operator (matrix) relating the concentrations of the chromophores C to the optical absorption at different wavelengths H_{msot}. As E is generally affected by local variations in the light fluence, accurate unmixing requires proper estimation of the light fluence distribution at the excitation wavelengths and inversion of (1.5) going a per-pixel (per-voxel) basis. Notably, blood offers a rich intrinsic contrast for label-free functional biological imaging as it is possible to distinguish between oxygenated (HbO2) and deoxygenated (Hb) hemoglobin (Fig 1.5). As an example of the five-dimensional OA imaging capabilities, Fig 1.6 displays the perfusion of brain vasculature in mice with ICG as a contrast agent. The wavelength dimension enables isolating contribution of the contrast agent through fast multispectral data acquisition and the subsequent reconstruction of agent distribution in real time. Yet, one inherent challenge in spectral unmixing is the so-called spectral coloring effect associated with the wavelength-dependent light attenuation. The algorithms accounting for this effect are, thus, crucial to increase the accuracy and quantitativeness of the measurements

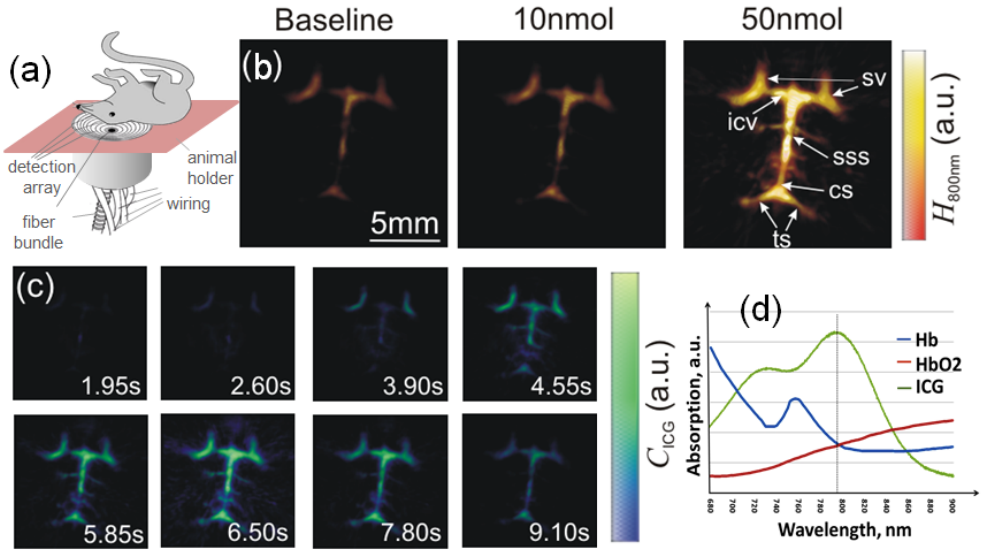

Figure 1.6: Five-dimensional imaging of mouse brain perfusion in vivo. (a) Layout of the experimental set-up. (b) Single-wavelength images (maximal intensity projection along the depth direction) acquired before and after injection of the ICG contrast agent. Results for two different concentrations are shown. When 10 nmol of ICG was injected, the contrast agent cannot be easily distinguished from the background blood absorption. Different structures in the mouse brain are indicated in the figure, supraorbital veins (SV), inferior cerebral vein (iCV), superior sagital sinus (SSS), confluence of sinuses (CS) and transverse sinus (tS). (c) Time series of images after spectral unmixing of multiwavelength data, taken for the 10 nmol experiment, clearly reveals the inflow of the agent in vivo and in real time. ICG, indocyanine green, (d) spectral excitation profile of several chromophores used for linear unmixing operations for identify the molecular constitution of tissue and presence of contrast medium. *Adapted in parts with permission from* [9].

1.2 Scope and objectives

In the dissertation project, we aim is to bring together the physics of imaging and image analysis to enhance the visual quality of OA images. To satisfy our goal, we undertook development of multiple algorithms to engineer an entire image analysis framework. Given the interdisciplinary nature of research, it is vital to apply to developed methods to pre-clinical and/or translational imaging. To this effect we demonstrated the capabilities of MSOT system and related methods for non-destructive imaging in assisted reproductive technologies and oncology imaging. Overall, the dissertation harmoniously bring together medical imaging and image analysis in unison and illustrate its application through biomedical imaging applications, potentially opening up new vistas in pre-clinical and translational OA imaging and image processing.

Research aims and achievements

The primary focus of the work is to develop an information theoretic framework for visual quality enhancement of OA images and demonstrate its applications to biological imaging. The predefined goals are as follows:

- Development of algorithms to enhance reconstruction performance and image quality, with emphasis on speed of sound auto-calibration, and reduction of negative values in reconstructed images.(Chapter 2)
- Using segmented priors to enhance accuracy and efficacy of OA reconstructions, e.g. mapping of multiple speeds of sound and mapping optical fluence. (Chapter 3)
- Improving resolution of reconstructed images using 'pixel super-resolution' method(s), which uses information from multiple geometrically distinct acquisitions to obtain high resolution image reconstruction. (Chapter 4)
- Demonstrating the efficacy of MSOT in biomedical imaging applications, through multiscale imaging of *in vivo* dynamics and multispectral imaging *in vivo* and *in vitro* in animal models. (Chapter 5)

We have conducted in-depth experimentation on automated speed of sound (SoS) fitting and segmentation of cross-sectional 2D images, real time 3D visualization and dynamic imaging based on single wavelength and multispectral data. Both phantom studies and animal imaging were conducted to develop and validate the algorithms as indicated.
We aimed to automate the parameter selection of OA image reconstruction to enable unsupervised real-time imaging and visualization, and used autofocusing metrics to automatically calibrate the SoS. In an attempt to reduce erroneous reconstruction which contains negative (spurious) values, we proposed a new entropy based non-negative image reconstruction algorithm. Going further, we introduced segmented image priors to correct for the small variations in SoS and optical fluence distribution within the tissues. We developed methodologies for segmentation of whole body small animal images with applications to achieve this goal. In our effort to improve image resolution, we evolved the intrinsic geometric scanning properties of the transducer arrays to achieve 'pixel super resolution' and thereby recover better images using existing system setups. The employed methods uses information from different scanning location to overcome the limitations in resolutions caused due to size of pixels, and should not be confused with recent literature on super resolution with aim to break the diffraction limit of light or of acoustic waves.
Focusing on the biological applications of MSOT, we demonstrated the non-destructive nature of MSOT through *in vitro* fertilization studies using a new intravital contrast agent Brilliant Cresyl Blue (BCB). Additionally, we reported the results of the newly developed v-MSOT system in four dimensional (4D) optoacoustic imaging of perfusion in preclinical breast tumor model *in vivo*. The study investigated the blood perfusion

and extravasation profile in heterogenic solid tumors, vital for analyzing hypoxia and cell nutrition gradients as well as viability, proliferation and drug response potentials.
We strongly believe that the dissertation contributes significantly to theoretical development of OA tomography, by bringing together imaging physics and image analysis. In terms of biological imaging the roadmaps illustrated in artificial reproductive technology and oncology are pioneering, and might prove to have far reaching impact.

1.3 Structure of the thesis

This thesis presents a set of algorithms for self-calibration of image reconstruction parameters and non-negative image reconstruction. Thereafter, it introduces the concept of segmented priors and shows it usage for improving reconstruction image quality. Then it discusses an algorithm to improve the image resolution without hardware additions. Finally, it shows the application of the developed systems and algorithms to two preclinical imaging protocols, viz. in vitro fertilization and oncological imaging.
Essentially, the thesis has been structured into six independent chapters highlighting both development of algorithms and pre-clinical imaging applications. The current chapter introduces the readers to the history and evolution of OA imaging, and outlines the scopes and objectives of the thesis.
Chapter 2 focuses on the issue of image reconstruction, in particular on automated calibration of reconstruction parameters and non-negative image reconstruction. We outline seven different autofocusing matrices and evaluate their performances to find the most suitable image, which in turn gives us a correct estimate of the speed of sound. In the second part of the chapter (2.3) we have present an entropy maximization based approach that employs a logarithmic regularization term for the tomographic inversion. The method enables accurate representation of the OA reconstruction. Further, we have experimentally validate the entropy maximization scheme on phantoms and *in vivo* samples.
Chapter 3 shows that multiscale segmentation algorithms and active contour models can be employed for boundary segmentation in OA tomographic images. The segmented boundary information is thereafter employed for automated fitting of multiple SoS values, and mapping of the optical absorption coefficient by means of light fluence normalization. The performances of the segmentation algorithms and their usefulness in improving image reconstruction was demonstrated using phantoms and small animal imaging experiments.
Chapter 4 outlines the theory and implementation of a pixel super-resolution algorithm in OA imaging and illustrate its effects on image resolution and contrast enhancement. The study includes simulations and experimental measurements on phantoms and ex-vivo murine organs.
Chapter 5 is focused solely on biological application of multiscale OA imaging and reports two independent studies that were conducted. In the first study, we employ a new contrast agent for *ex vivo* ovarian imaging, and demonstrates the capability of OA for non-destructive molecular imaging of intact ovarian follicles. The study hold great

potential for *in vitro* fertilization (IVF) and might be clinically useful as an assisted reproductive technology. In the second application study, we explored the capabilities of vMSOT for cancer imaging in pre-clinical models. We interpreted intrinsic tissue properties, such as blood oxygenation gradients, along with visualization of externally administered nanoparticle distribution in order to study vascularization, probe penetration and extravasation kinetics in solid tumors. The study highlights v the clinical potential of this technology in skin or breast diagnostics and therapy monitoring.
Finally, Chapter 6 summarizes the novel contributions made by the dissertation and outlines the future scope of the work. All chapters of the thesis is linked with one of more peer-reviewed (or in review) research publication(s), the relevant publications are suitably cited and indicated in the connected chapter.

2 Optimization of image reconstruction and self-calibration of parameters

Optoacoustics (OA) offers unique *in-vivo* imaging capabilities for preclinical research [18]. However, achieving optimal resolution and contrast as well as associated quality measures in OA tomographic images requires accurate representation and calibration of the reconstruction parameters. In tomographic OA imaging, multiple parameters related to both light and ultrasound propagation characteristics of the medium need to be adequately selected in order to accurately recover maps of local optical absorbance. In the current chapter, we focus on two important issues that are needed to be solved to improve OA imaging performance, viz. calibration of essential reconstruction parameters, and non-negative OA reconstructions.

Speed of sound (SoS) in the imaged object and surrounding medium is a key parameter conventionally assumed to be uniform. Mismatch between the actual and predicted SoS values may lead to image distortions but can be mitigated by manual or automatic optimization based on metrics of image sharpness. Although some simple approaches based on metrics of image sharpness may readily minimize distortions in the presence of highly contrasting and sharp image features, they may not provide an adequate performance for smooth signal variations as commonly present in realistic whole-body OA images of small animals. In this chapter, we illustrate a class of new hybrid methods, which are shown to outperform well-established autofocusing (AF) algorithms for small animal OA imaging *in vivo*. Further, tomographic OA reconstructions are ideally expected to represent maps of the initial pressure rise induced by the absorption of pulsed light in tissue. In practice, due to inaccurate modeling assumptions and a variety of unpredictable experimental factors, the images are often afflicted with negative values and erroneous pixel intensities. We present an entropy maximization based approach that employs a logarithmic regularization term for the tomographic inversion. In this way, a non-negative constraint is intrinsically imposed on the rendered images, thereby enabling accurate representation and quantitative imaging performance of the OA reconstructions.

Parts of this chapter has been adapted with modifications from:

S. Mandal, E. Nasonova, X. L. Deán-Ben, and D. Razansky, "Optimal self-calibration of tomographic reconstruction parameters in whole-body small animal optoacoustic imaging," Photoacoustics, vol. 2, pp. 128–136, Sep. 2014.

2.1 Optoacoustic reconstruction and instrumentation

2.1.1 Image reconstruction (inversion) methods

In Section 1.1 we have discussed the OA signal generation problem in OA imaging, in the current section we will discuss the methods for reconstruction of optical absorption distribution from a set of measured ultrasonic pressures. There are numerous inversion methods used by researchers, which depend of several factors, including shape of the transducer (or detector geometry), nature of the detector, computation time, intended resolution of reconstruction etc. Given the most simplistic scenario, we assume using spherically focused transducer and reduce the problem to a simple one-dimensional detection of signal along a straight line [32]. The detector when scanned along other dimensions, the reconstruction problem essentially becomes a planer (2D) or a spherical (3D) triangulation problem. The solution for the same can be readily obtained by using algorithms like the delay-and-sum algorithms etc. Similarly, reduction into a 2-D imaging problem could be done by using cylindrically shaped detection elements, focused onto a certain plane [33]. In general, the strategy adopted for tomograpic OA systems is to collect OA signals from as many locations (viewing angles) around the imaged volume as possible (typically 256 in our case). Thereafter, the most widely used image reconstruction (or inversion) method is the filtered backprojection algorithm (FBP), which is a closed-form formulation expressed in two or three dimensions and are analogues to the inverse-Radon transform reminiscent of X-ray computed tomography. Several approaches to solve the backprojection formulas has been proposed for different detection geometries and are implemented either in the spatiotemporal domain [34] or in the Fourier domain [35]. Assuming a circular scanning geometry and exact inversion formula for 2D imaging was introduced by [36], and later generalized using the universal backprojection method [34]. The inversion formula calculates a 2-D integral over sum of an infinite function series. The first-order approximation is conventionally used to reduce the numerical complexity of the calculation, leading to the backprojection formula given by,

$$H_r(\vec{r}) = \frac{C_T}{4\pi c^2 \beta} \int_{t=|\vec{r}\,'-\vec{r}|c} \frac{1}{t} \left[\frac{p(\vec{r}\,', t)}{t} - \frac{\partial p(\vec{r}\,', t)}{\partial t} \right] dA' \tag{2.1}$$

The backprojection algorithms are simple, convenient and fast, thus they are widely used. However, the accuracy of such algorithms is limited and they suffer from substantial artifacts and are more susceptible to limited view problems. The methods suppress the slowly varying image components and accentuate the fast changes (small details), which often gives rise to negative optical-absorption values that have no physical interpretation [37]. Additionally, the hypothesis behind backprojection algorithms assumes an ideal description of the acoustic wave propagation and detection as well as on specific detection geometries. Therefore, generalizing the formulation for more realistic OA illumination-detection models by incorporating configuration of detectors and instrumentation-dependent factors becomes non-trivial.

To overcome the challenges of backprojection based methods and to reduce the artifacts, the model-based methods were suggested [38, 39]. The iterative algorithms have been

used in X-ray images for decades and solves the forward problem numerically in an iterative optimization algorithm. The aim of the model-based method is to minimize the error between its corresponding acoustic signals and the measured signals [39]. In this dissertation work, we have primarily used the numerically efficient interpolated model-matrix inversion (IMMI) proposed by Rosenthal *et. al.* [15]. The IMMI algorithm represents an exact numerical model-based reconstruction method and offers quantitative results by taking into account the various experimental imperfections, preserving the low frequency information and reducing image artifacts. The IMMI solves Eq. 1.3 in a highly efficient semi-analytical manner by applying linear interpolation to $H_r(\vec{r})$ and performing the integral analytically. This leads to a discretization of Eq. 1.3, given by the following matrix relation:

$$p = \mathbf{M}z \tag{2.2}$$

where p represents pressure fields measured at different positions (projections), z are values of OA image on the defined grid, and M is the acoustic forward-model matrix. The OA image is obtained by inverting Eq.2.1 by employing Moore–Penrose pseudoinverse [40] and/or the least squares decomposition (LSQR) algorithm [41]. The pseudoinverse of $\mathbf{M}$ is given by,

$$\mathbf{M}^{+} = (\mathbf{M}^{H}\mathbf{M})^{-1}\mathbf{M}^{H} \tag{2.3}$$

while the reconstructed OA image is subsequently obtained via,

$$z = \mathbf{M}^{+}p \tag{2.4}$$

The pseudoinverse needs to be calculated for a given system only once, and it enables fast inversion. Thus researchers have been able to achieve near real-time reconstruction using the method, and has opened up new possibilities in functional imaging. The LSQR, on the other hand, is an iterative algorithm for solving linear equations . It is highly efficiency in the case of sparse matrices, and since it only saves the nonzero elements of the matrix, it can operate on smaller memory footprints [42].
The IMMI algorithm [15] (as used in Chapters 3,4,5 of the thesis) represents an exact numerical model-based reconstruction method and offers quantitative results by taking into account the various experimental imperfections, preserving the low frequency information and reducing image artifacts. In this method, the difference between the measured pressure at a set of locations and instants(expressed in a vector form as $\mathbf{p}$), and the equivalent theoretical pressure is iteratively minimized using least square minimization techniques. The optical absorption at the pixels of the ROI, expressed as vector form $\mathbf{F}$, is calculated as follows,

$$\mathbf{F} = \mathrm{a}rgmin_{\mathbf{F}}\|\mathbf{A}\mathbf{f} - \mathbf{p}\|^2 + \lambda^2\|\mathbf{L}\mathbf{f}\|^2 \tag{2.5}$$

where $\mathbf{A}$ is the linear operator(or model matrix) mapping the optical absorption to the acoustic pressure. We use standard Tikhonov regularization [43] to minimize the high-frequency noise and reduce the effects on limited view in the inversion process. The matrix $\mathbf{L}$ represents a high-pass filter operation. For all practical purposes we use a Butterworth band-pass filter between 0.1–7 MHz to filter the acquired signal. Since the

model matrix M is sparse, LSQR is an extremely efficient method for inverting Eq. 2.5 when the number of grid points is high.
There have been several other interesting and efficient inversion algorithms that has been proposed and each presents its unique benefits [44], viz. time-reversal [45], quantitative signal extraction method using sparse reconstruction [46], high-throughput sparsity-based inversion [47], wavelet packet based OA reconstruction, polar coordinate based expedited model-based reconstruction [48], curve driven acoustic inversion [49] etc. However, a detailed study of the vast domain of inversion methods is beyond the scope and requirements of the current thesis.

2.1.2 Instrumentation

For acquisition of the data for the experimentations in Chapters 2-5. we used the cross-sectional OA acquisition geometry [2] using a commercial small animal MSOT scanner (Model: MSOT256-TF, iThera Medical GmbH, Munich, Germany). The scanner consists of a custom-made 256-element array of cylindrically focused piezocomposite transducers with 5 MHz central frequency for simultaneous acquisition of the signals generated with each laser pulse. The transducer array covers an angle of approximately 270° and has a radius of curvature of 40 mm. To offer real-time (video rate) imaging capacity, it optimizes light energy delivery that avoids the need for data averaging and offers parallel detection of OA signals around the area of maximal light deposition. Light excitation is provided with the output laser beam from a wavelength-tunable optical parametric oscillator (OPO)-based laser, which is shaped to attain ring-type uniform illumination on the surface of the phantoms by means of a custom-made fiber bundle.The system houses a custom-made semiarc multielement-focused piezocomposite ultrasonic array and ring-type illumination, delivered via a fiber bundle. The detected OA signals are simultaneously digitized at 40 Msps, the system diagram is available in Fig. 1.4. To facilitate *in vivo* measurements, the system contains an imaging chamber with integrated animal holder with a water-impenetrable membrane that averts animal contact with water, and simultaneously enable delivery of vital air and anesthesia (isoflurane in vapor form) through a mouthpeice to the experimental animal. The temperature of the entire water bath with which the imaging chamber is inundated is maintained at $34°C$ using heating coils and stirrers to distribute heat equitably. The scanner is capable of rendering 10 cross-sectional images per second, but for our experiments the images were averaged 10 times in order to improve SNR performance in acquiring entire mouse cross-sections.
We further developed a 3D real-time acquisition system with a spherical acquisition geometry, detailed description of the same is available in section 5.2.1.

2.2 Self-calibration of speed of sound

The position and orientation of the ultrasound sensors, spatial variations of the SoS, attenuation and other acoustic properties of the propagation medium may all significantly affect the collected OA responses [7] and therefore must be correctly accounted

for in the image reconstruction process. For example, cross-sectional OA systems based on single-element [50, 33] or arrays of cylindrically-focused transducers [2, 51] are commonly employed due to important advantages derived from reducing the OA problem into two dimensions. For accurate tomographic reconstructions, the location of all detection points in the imaging plane needs to be precisely known or determined experimentally, the latter by e.g. imaging a calibration phantom having a uniform and known SoS. Once the acquisition geometry is properly calibrated, the correct values of the acoustic propagation parameters must still be taken into consideration, ideally with the use of an algorithm accounting for acoustic heterogeneities [52, 53, 54, 55, 56]. In many practical cases, the map of SoS variations in the imaged medium is not available a-priori nor can be extracted experimentally so representative reconstructions are obtained by considering a uniform heuristically fitted SoS [55, 57].
Dependence of SoS on the temperature of the surrounding matching medium is yet another uncertainty that must be accounted for, e.g. by continuously monitoring the temperature throughout duration of the experiment [58]. Indeed, even subtle temperature variations lead to substantial changes of SoS in water of 2.6 $ms^{-1}/^{\circ}C$ [59]. Consequently, if the water temperature cannot be properly controlled during a prolonged experiment, dynamic calibration of the SoS becomes essential. In addition, local discrepancies between sound propagation velocity in the water and the imaged sample, even under assumption of uniform acoustic properties, may raise the necessity in additional SoS calibration on a per-slice basis. Moreover, fast automatic calibration of the SoS is of high importance in real-time imaging systems, where GPU-accelerated reconstruction algorithms now allow for real-time OA visualization of the sample in the course of the experiment [24]. Determining AF parameters for biological images has been a wide area of research and diverse families of methods have been reported for digital microscopy [60, 61, 62], shape from focus [63], cytogenetic analysis [64]. Some simple AF approaches based on sharpness metrics [65] may perform equally well for OA, especially when high frequency strongly contrasting image features such as high resolution subcutaneous are present in the images. However, they may not provide an adequately robust performance for smooth or ultrawideband signal variations as commonly present in realistic whole-body OA images from small animals, especially when considering quantitative model-based reconstructions that preserve low-frequency information [15].
In the dissertation work, we propose novel and efficient hybrid focusing metrics employing pre-processing to enhance the focusing performance. The proposed methods incorporate key improvements, viz. edge detection and diffusion, making them optimal for application in OA SoS self-calibration. Further, we investigated the performance of a developed AF algorithms for automatic SoS calibration in cross-sectional OA tomography vis-à-vis several benchmark (previously mentioned in literature and used in OA reconstructions) .

2.2.1 Autofocusing algorithms

The workflow for a typical SoS calibration procedure is depicted in Fig. 2.1. OA images corresponding to selection of different values of the SoS in a certain reasonable range

are tomographically reconstructed from the recorded signals. Thereafter, the reconstructed images are processed with the AF algorithm and focus measures are employed to determine the best matching SoS. The fitted SoS, as obtained from the calibration method, is then fed back as a parameter for the reconstruction of the dataset/frame. The algorithms described in this section can be classified into three main groups, namely intensity-based (2.2.1.1 and 2.2.1.2), gradient-based (2.2.1.3 and 2.2.1.4) and edge-based (2.2.1.5-2.2.1.7) measures, where the last group of metrics simultaneously correspond to the hybrid approaches suggested in this work. In order to enable comparison between the different methods, all focus measures are readjusted so that the global minima represent the most focused image. The focus measure is normalized to the maximum value in the SoS range considered. Focus metrics were calculated on the interval from 1460 to 1580 m/s, corresponding to a typical range of SoS in water and soft tissues, with step size of 1 m/s, and processed with smoothing Savitzky-Golay denoising filter (with polynomial order of 0 and window size of 5 points) [66]. The algorithms tested are presented as follows.

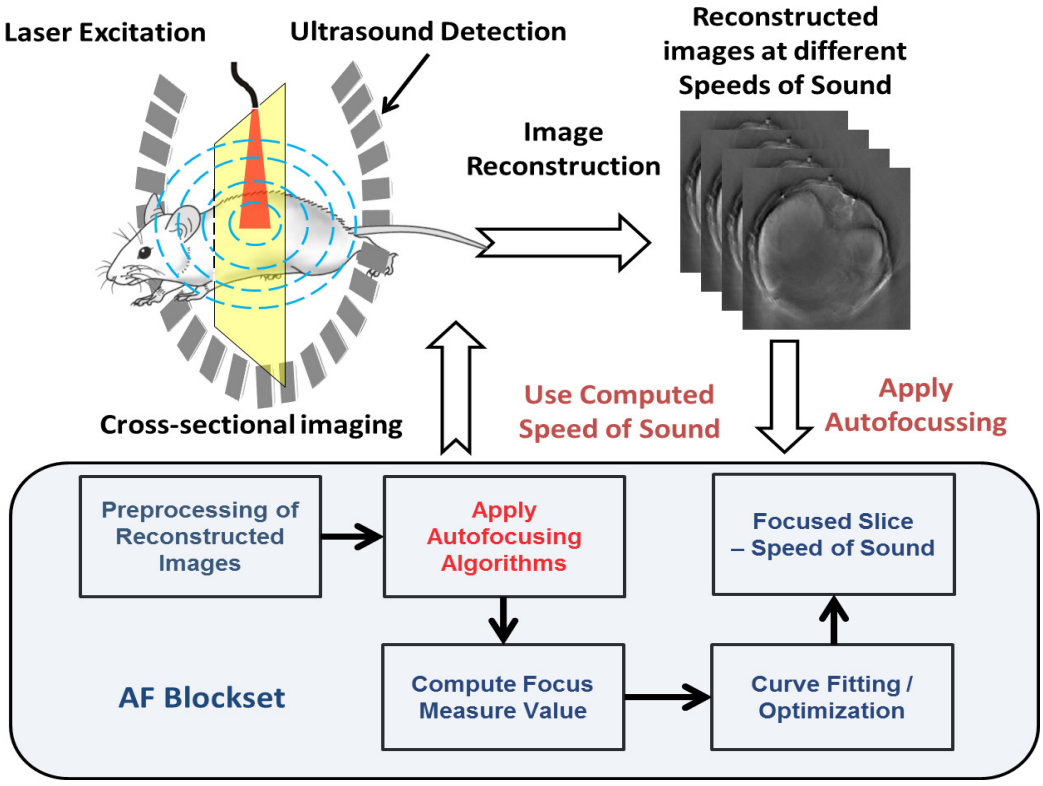

Figure 2.1: Basic principle of the application of the autofocusing in the optoacoustic reconstruction workflow. The AF blockset illustrates the post-reconstruction autofocusing algorithm employed to automatically calibrate speed of sound.

2.2.1.1 Maximum pixel intensity

The maximum pixel intensity represents the most intuitive and computationally efficient focus measure. The method is inspired by the tendency of the user to look for the brightest spots in the focused image as well as the largest image contrast so that it is assumed that a given structure has the highest intensity value when it is focused. As such, this metric is expected to perform better with high signal-to-noise-ratio (SNR) images rich with high-contrast features, but is the most artifact-prone if noise and other image artifacts yield these high-intensity features. The focus measure is defined as,

$$F_{MI} = -max_{(x,y)}[f(x,y)] \tag{2.6}$$

where $f(x,y)$ is a function of two variables representing the grey level intensity in the cross-sectional image. The negative sign is added so that the global minimum represents the most focused image, as mentioned above.

2.2.1.2 Maximum intensity range

The maximum intensity range is a modified version of the previous method [61]. In this case, the difference between the maximum and minimum pixel intensity is calculated, i.e., the focus measure is defined as,

$$F_{MIR} = -\{max_{(x,y)}[f(x,y)] - min_{(x,y)}[f(x,y)]\} \tag{2.7}$$

2.2.1.3 Brenner's gradient

The Brenner's gradient provides a quantitative measure of image sharpness. It is based on computing the difference between the intensity values for pixels separated by two times the pixel size. In two dimensions, it can be expressed as,

$$F_{BG} = -\left\{\sum_{x,y}\left[f\left(x+2,y\right)-f\left(x,y\right)\right]^2+\sum_{x,y}\left[f\left(x,y+2\right)-f\left(x,y\right)\right]^2\right\} \tag{2.8}$$

The Brenner's gradient is a widely used metric and it has been shown to oFutperform other methods for SoS calibration in three-dimensional OA imaging [65].

2.2.1.4 Tenenbaum's gradient

The Tenenbaum's gradient uses an edge-detection-based approach (sharper edges correspond to higher frequencies). The gradient is determined by a convolution between the Sobel operator (and its transpose) with the image pixels. This focus measure is calculated as,

$$F_{TG} = -\left\{\sum_{x,y}\left[G*f\left(x,y\right)\right]^2+\left[G^T*f\left(x,y\right)\right]^2\right\} \tag{2.9}$$

where $G = \begin{bmatrix} -1 & 0 & +1 \\ -2 & 0 & +2 \\ -1 & 0 & +1 \end{bmatrix}$ represents the Sobel operator and '*' denotes two-dimensional convolution. While the Tenenbaum's gradient has been reported to be superior in microscopy [62], its performance in OA imaging has been shown to be comparable to that of the Brenner's gradient [65].

2.2.1.5 Normalized sum of edge pixels (Edge+Sum)

The normalized sum of edge pixels calculates the sum of pixels corresponding to strong edges, subsequently normalized by the total number of pixels in the image. The Sobel approximation to the derivative is used as edge detection algorithm. This metric aims at minimizing the influence of thin circles and 'crossing-arcs' artifacts typically present in unfocused cross-sectional OA images. The method then aims at maximizing clearly defined edges, i.e., it represents, to some extent, an opposite approach to the traditional camera focusing. The focus measure is then expressed as,

$$F_{ES} = \frac{1}{N} \sum_{x,y} e\left(x,y\right) \tag{2.10}$$

being N the number of pixels in the image and
$e\left(x,y\right) = \begin{cases} 1, & g\left(x,y\right) > threshold \\ 0, & otherwise \end{cases}$,
with $g\left(x,y\right) = \sqrt{\left[G * f\left(x,y\right)\right]^2 + \left[\left(G^T\right) * f\left(x,y\right)\right]^2}$
The value of the threshold was determined automatically by computing the root mean squared (RMS) estimate of noise [67].

2.2.1.6 Normalized variance of the image gradient magnitude using Sobel operator (Sobel+Var)

The normalized variance of the image itself has been previously reported as focus measure in computer microscopy [60, 68] and later in OA imaging. Herein, we suggest an additional step consisting in computing the variance of the gradient magnitude obtained by convolution with the Sobel operator. This metric belongs to hybrid approaches being combination of statistics-based and derivative-based algorithms, leading to an enhanced performance in OA images having a relatively low contrast compared to natural images. The focus measure is expressed as,

$$F_{SV} = -\frac{1}{N\mu} \sum_{x,y} \left(g\left(x,y\right) - \mu\right)^2, \tag{2.11}$$

where μ is the mean value of g(x,y), as defined in earlier subsection.

2.2.1.7 Anisotropic diffusion enhanced energy of image gradient using consistent gradient operator (Ad-CG)

We have developed a hybrid methodology based on a combination of anisotropic diffusion and consistent gradient (CG) operator with is customized for our current OA image datasets. Anisotropic diffusion is an iterative scale-space approach, which enhances the edges while smoothing the rest of the information in the image [68]. The purpose of this pre-processing step is twofold, namely, to remove noise and intensity fluctuations on the one hand, on the other - to reduce the ripples in focus measure as a function of the SoS. The continuous form of the non-linear partial differential equation (PDE) as proposed by Perona and Malik [69] for diffusing an image is given by, [70],

$$\begin{cases} \frac{\partial I}{\partial t} = div\ \left[d\left(|\nabla I|\right) \bullet \nabla I\ \right] \\ I\ \left(t = \ 0\right) = f_0\left(x, y\right) \end{cases} \tag{2.12}$$

where ∇ and div are the gradient and divergence operators, respectively, $C(x)$ is the diffusion coefficient, and $f_0(x, y)$ is the initial image. Eq. 2.12 is solved iteratively as explained by [69], where the diffusion coefficients is taken as $c\left(x\right) = \frac{1}{1+(x/k)^2}$ with k being an edge magnitude parameter.
A Consistent Gradient (CG) operator is thereafter applied as a second step to compute the energy of the image gradient which is translated as focus measure scores [71]. This approach has been reported to have more stable AF performance under varying illumination conditions for microscopic imaging [72, 73]. The use of a CG operator ensures the exactness of gradient direction in a local one-dimensional pattern irrespective of orientation, spectral composition, and sub-pixel translation. The energy of the image gradient is defined as,

$$E = \int_{-\infty}^{\infty} \int_{-\infty}^{\infty} \left|\nabla f\left(x, y\right)\right|^2 dx\, dy. \tag{2.13}$$

The actual focus measure including all intermediate steps can be expressed in a form:

$$F_{ADCG} = \frac{1}{N} \sum_{x,y} w \bullet I_H + (1 - w) \bullet I_V \tag{2.14}$$

where N is the total number of image pixels and w is an additional factor allowing for flexibility in assigning more weight to horizontal I_H or vertical I_V derivative approximations defined as,

$$I_H = CG * I_{AD};\ I_V = CG^T * I_{AD} \tag{2.15}$$

being I_{AD} the OA image after anisotropic diffusion filtering, and CG is the 5x5 consistent gradient operator expressed as,

$$CG = \begin{bmatrix} -0.003776 & -0.010199 & 0 & 0.010199 & 0.003776 \\ -0.026786 & -0.070844 & 0 & 0.070844 & 0.026786 \\ -0.046548 & -0.122572 & 0 & 0.122572 & 0.046548 \\ -0.026786 & -0.070844 & 0 & 0.070844 & 0.026786 \\ -0.003776 & -0.010199 & 0 & 0.010199 & 0.003776 \end{bmatrix}$$

2.2.2 Experimental results and statistical analysis

To test the impact of reconstruction methodologies on the outcome of the calibration procedure, back-projection and model-based inversion methods were compared, and the results for the ex-vivo murine kidney experiment are displayed in Fig. 2.2. Even though all images were manually thresholded to attain best visual appearance, the image quality is generally improved with the model-based approach over the back-projection reconstructions, the latter exhibiting generally unreasonable distribution of the optical absorption with pronounced negative value artifacts across the imaged sample. The calculated focus measures as a function of the SoS are showcased in Fig.2.2a and 2.2b for back-projection and model-based reconstruction, respectively. All focus measures are normalized to the maximum value in the SoS range. A Savitzky-Golay denoising filter was further applied as a valuable additional step for removing spikes from the focus measure plots, thus avoiding ambiguity and locking up into local minima.
The focus measures are expected to have a minimum for the value of the SoS corresponding to the best focused image. Indeed, most of the metrics reach the same calibration SoS regardless of the reconstruction method. Examples of reconstructed images with back-projection and model-based reconstruction of the ex-vivo murine kidney for several equally spaced SoS values are displayed in Fig.2.2c and 2.2d respectively, where the subjectively best-looking images correspond approximately to the minimum of most focus measures. The metrics generally show sharper focusing performance with back-projection reconstruction, probably due to higher frame-to-frame variability when the SoS was changed. On the other hand, the focus scores were generally more consistent for the model-based reconstructions. The focusing curves were less noisy for the Ad-CG method, where 2 iterations were used in the anisotropic diffusion step, as determined empirically.

The results of the *in vivo* mouse imaging studies are displayed in Fig. 2.3. In particular, the focus measures for the head, liver and kidney/spleen regions as a function of the SoS are showcased in Fig. 2.3a, 2.3b and 2.3c, respectively. Representative images for these three regions of the mouse body obtained by considering different values of the SoS are accordingly shown in Figs. 2.3d, 2.3e and 2.3f. All images were reconstructed with the back-projection approach. The numbers of iterations in the anisotropic diffusion procedure were heuristically chosen as 4, 12 and 18 for the liver, brain and kidney/spleen regions, respectively. The iterations ensures that a sufficient level of smoothening is achieved without blurring edges, thus different number of iterations were determined for each region imaged based on observation and inherent nature of the images. Further, a fixed edge weight w (see eq. 2.14) of 0.95 was used for all the experiments with Ad—CG method. The choice of number of iteration is thus critical for the good performance of the algorithm, effects of weighting is limited for the current modality but might have greater applicability in presence of strong limited view problems.
A higher variability in the focus measures was noticed for the brain images, primarily due to the lack of well-defined structures and edges to focus on. For example, the Tenenbaum measure yielded a minimum at the upper limit of the SoS range, where the reconstructed image for this particular selection (Fig.2.3d) is clearly deteriorated. The performance of

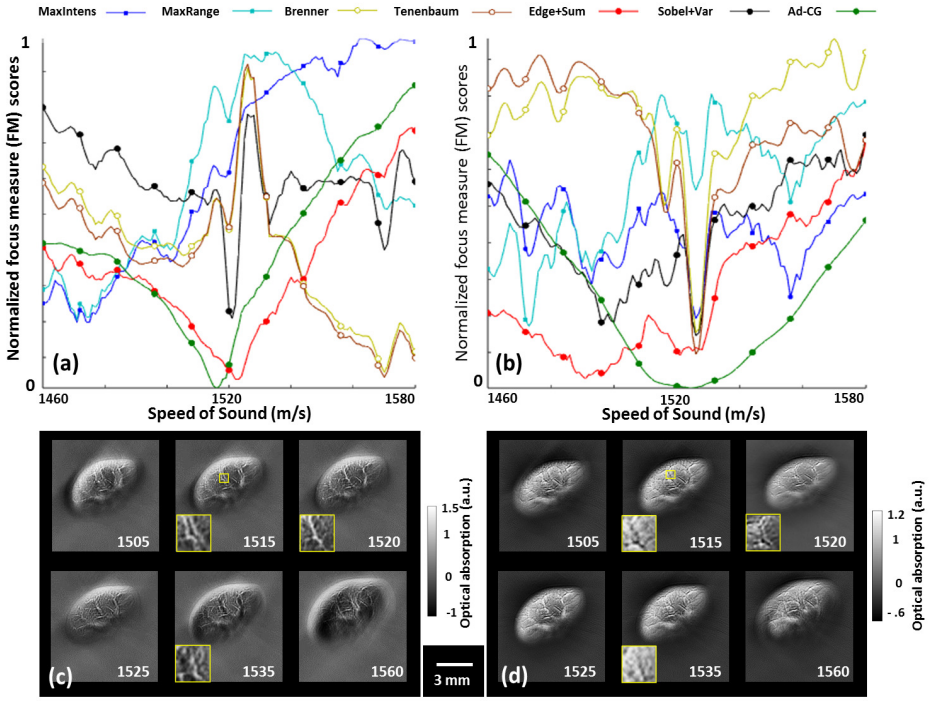

Figure 2.2: Speed of sound calibration for an ex-vivo murine kidney. The graphs show the normalized focus measures versus the speed of sound for 7 different focus measures using (a) back-projection and (b) model-based reconstruction methods. For all focus measures the global minima determines the most focused image. Panels (c) and (d) show the images at six different speeds of sound reconstructed with back-projection and model-based algorithms, respectively (values are stated in [m/s]). A zoom-in of a representative region inside the object is showcased for a better visual evaluation of the image quality enhancement achieved with the proper value of the speed of sound.

the metrics was better for the kidney/spleen and the liver regions given higher intrinsic contrast and defined vascular structures found in these areas. As a first approach, the temperature of the coupling medium (water) can be used for referencing the SoS and using it for reconstructing the data. However, as clearly shown in Figs. 2.3d-f (first column), the resulting images obtained for this value of the SoS are not optimal. Indeed, the average SoS in soft tissues is approximately 1540 m/s, and can have variations of up to 10% with respect to the SoS in water [15]. A different (generally higher) SoS must then be used for the reconstruction, and the AF algorithms provide a suitable platform for this purpose. The manually selected values of the SoS are highlighted in the second column of Fig. 2.3. The manual calibration values were decided based on subjective testing using feedback from three independent volunteers experienced in reading animal anatomy but with no prior knowledge of the SoS calibration values. SoS retrieved with the proposed AF algorithms fits best the one selected manually using the subjective testing. It is worth noticing that only the three last hybrid focus metrics, especially the

Ad-CG, have the sharp peak on the entire interval, probably due to the diffusing (or smoothing) processing of the image. This in turn minimizes the chances for secondary local minima to appear, which may lead to misinterpretation of the results. It is to be noted that, anisotropic diffusion is a well-known image processing technique that successfully reduces image noise without compromising significant parts of the image content, typically edges, lines or other details that are essential for image interpretation and analysis [69].

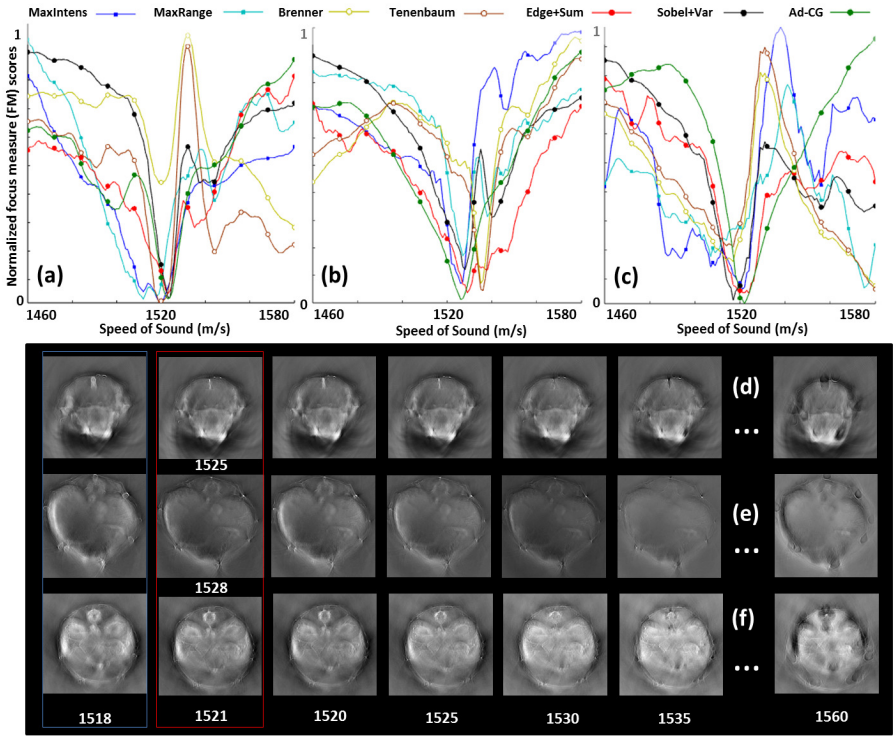

Figure 2.3: Focus measure (FM) plots for 7 different metrics in three different anatomical regions of the mouse during in-vivo imaging of (a) brain, (b) liver, and (c) kidney/spleen. The global minima of the focus measure score represents the calibrated speed of sound. Reconstructed images at different speed of sound values for the respective regions are shown in (d), (e) and (f), where the first and second column correspond, respectively, to the speed of sound in water (at $34°C$) and the speed of sound manually fitted.

To quantify the overall efficacy of the results, tests on 10 datasets for each of the designated regions in mice were conducted. The boxplots of the resulting values of the SoS are shown in Fig. 2.4. The gradient-based methods, i.e. Brenner's and Tenenbaum's gradients, generally performed satisfactorily, in agreement with earlier publications [74], although secondary drifting peaks often appear, which severely offset the global minima value. The effects of such secondary fluctuations were reduced with the filtering process and by considering only a SoS range between 1480 and 1560 m/s. Secondary peaks also appeared in some cases when considering the Edge+Sum algorithm, although the

resulting variability is lower. On the other hand, the performance of the two proposed metrics Sobel+Var and Ad-CG are consistent (no secondary peaks appeared) and provide variability similar to that obtained by manual selection. The worst performance in terms of variability and fitted SoS value have been obtained by the intensity-based methods, presumably due to the highest susceptibility to noise and artifacts.

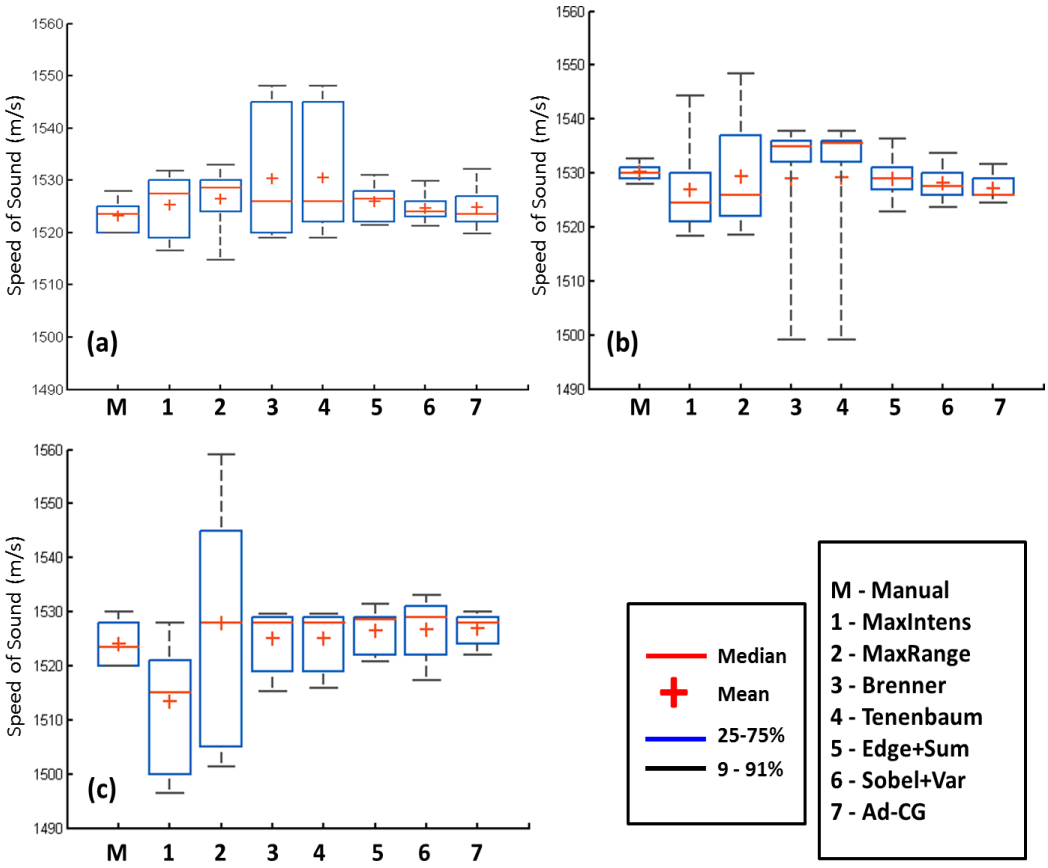

Figure 2.4: Boxplots indicating the speed of sound variability for 10 independent datasets for (a) brain, (b) liver, and (c) kidney/spleen regions.. User feedback was taken for the manual calibration and the 7 automated metrics were compared against it.

2.2.3 Effect of temperature on SoS and use of temperature priors

In most of the present OA scanning methods water is used as an interface or coupling medium between the scanning objects and ultrasound detectors. The protocols assume that temperature is uniform and constant throughout the experiment and the same is ensured by heating the water till the body temperature of the animals (or other scanning object). However, in practical experimental setups often the heating circuit is turned off during scanning to prevent formation of bubbles and water currents. This causes a temporal variation in the water temperature, which in turn changes the SoS

producing image artifacts during reconstructions [58]. Image quality in OA tomography is strongly conditioned by the reconstruction algorithms employed, and the SoS is an intrinsic parameter contributing to the same. During the experiment, it is observed that the variations in temperature of the medium (and the object) cause notable degradation of image qualities, if unaccounted for. Two tissue-mimicking agar phantoms (1.3% agar powder by weight) were used in the experiments. To provide more uniform illumination, 1.2% by volume of Intralipid was added to the solution. Inside the phantom black polyethylene microspheres with an approximately diameter of 200 μm (Cospheric BKPMS $180 - 210$ μm) were embedded (3 in number). We applied the SoS calibration methods to correct for the effects of variations of temperature in reconstruction image quality, using the designated focus measures. The effects of variations in SoS caused

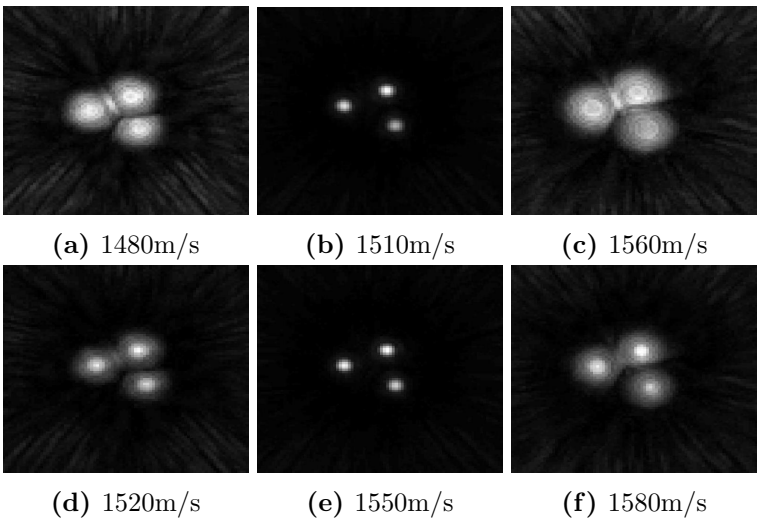

(a) 1480m/s **(b)** 1510m/s **(c)** 1560m/s

(d) 1520m/s **(e)** 1550m/s **(f)** 1580m/s

Figure 2.5: Phantoms with microparticles (approx. 200μm) reconstructed at various speeds of sound (a-c) given temperature = 27.5°C;corrected against varying temperature with time (b)the calibrated speed of sound is 1505 m/s, Sub-figures(d-f) shows the divergence in SoS with variation of temperature (temperature = 40.5°C;calibrated speed of sound is 1550 m/s after temporal correction with varying temperature.

by the changes in the temperature of the water bath are clearly observed in Fig 2.5. We see that the ideal SoS is 1520 m/s (Temperature = 27.5°C) and there are visible distortion for when the image is reconstructed with an incorrect value of SoS. Further, it is observed that given the temperature changes the SoS calibration varies, e.g. as in Fig. 2.5b the correct SoS is 1510 m/s whereas for Fig. 2.5e the calibrated SoS is 1550 m/s for temperatures $T = 27.5$°C and 40.5°C respectively. A comprehensive experiment was conducted with drop in temperature of approximately 20°C over a time-frame of 142 minutes. It was observed that even a change of 0.8°C caused a significant alteration of SoS thus affecting the quality of the reconstructed image. The failure to factor for these intra-scan variations in SoS causes image artifacts which impairs the structural information in the scans. Thus, we can infer that changes in temperature of the coupling medium results in varying SoS which impacts the quality of the reconstructed images.

Image analysis based SoS auto-calibration method can suitably be used for for better image reconstruction performance by reducing the intra-scan drifts.
The temperature of the coupling medium is constantly monitored by a thermocouple capable of tracking 0.1°C changes in the water temperature. Any changes over 0.5°C is sampled and factors for image correction and re-calibration purposes. Ideally, a uniform temperature of 34°C is attempted to be maintained, for which the SoS in water is 1510m/s. Using this as a priori information, the optimization is done in a range of ±25 m/s with respect to SoS in water. This drastically reduces the total search spaces from 200 SoS as earlier searched to a narrow band. The usage of GPU processing in image reconstruction and AF further improves the time footprint of the calibration step. The temperature of the coupling medium (water) is thus used for referencing the SoS and reconstructing the data. Manually fitted SoS, demonstrates that considering the SoS of the medium is not optimal, as the imaged tissue can have variations of up to 10% with respect to the SoS in water. The computational time of back-projection for generating a stack of 100 images at different SoS (200 x 200 pixels) are approximately 8.818 s, and for a windowed 50 SoS is 5.321s. Thus, we have an effective gain in efficiency by introducing the prior. A workstation with Intel i7-480 CPU operating at 3.70 GHz and with 32 GB of RAM was used for the experimentation. The back-projection reconstruction is further accelerated using the OpenGL platform on an AMD Raedeon GPU (Clock speed- 1100 MHz, Memory size 3072 MB, Shaders 2048).

2.2.4 Discussion

We have systemically analyzed the applicability of focusing techniques for automatic calibration of a uniform speed of sound value in OA tomographic reconstructions. For the particular implementation in cross-sectional whole body OA small animal imaging, efficacy of two of the suggested methods, namely, the normalized variance of the image gradient magnitude using Sobel operator and the algorithm employing anisotropic-diffusion-enhanced energy of the image gradient using consistent gradient operator, was found superior to the other established focus measures.
The need for AF in OA tomographic imaging stems from the fact that the average SoS in the region covered by the measuring locations is unknown. Even if the geometrical distribution of the tomographic detection points is accurately calibrated and the water temperature is known, the corresponding SoS in water for such temperature generally does not lead to the optimum results. This effect has been illustrated in this work, where the self-calibrated SoS was generally higher than the SoS in water. This result is consistent with the fact that the average SoS in soft tissues is slightly higher than that in water, with variations reaching up to 10% [58]. The SoS in water can, however, be used as an initial guess that may serve as the central SoS of the search interval and thus ease the optimization of the focus measures [75]. On the other hand, although representative images can be rendered with algorithms assuming a uniform SoS, more accurate reconstructions may require considering a heterogeneous distribution, and AF may also play a similar role in fitting the SoS of defined regions.
A good performance of the methods analyzed in this work has been demonstrated for

images reconstructed with two different reconstruction algorithms. Indeed, whereas back-projection reconstruction highlights the high spatial frequency components of the image, model-based inversion generally renders more quantitative images by accurate estimation of the low-frequency background. On the other hand, the computational burden for back-projection reconstructions is usually significantly lower so this approach is more convenient for fast (dynamic) calibration of the SoS during real-time operation. Essentially, the best performing metrics would not only show good performance in phantoms or imaging of subcutaneous vasculature but also in cases of *in-vivo* imaging of entire animal cross-sections. A good performance was obtained in mouse experiments in-vivo for three representative regions corresponding to the location of the brain, liver and kidney/spleen. However, secondary peaks in the focus measures led in some cases to erroneous interpretations, which increase variability of the results. The best results in terms of consistency (as compared with manual fitting) and low variability were achieved with the hybrid approaches suggested in this work. Even though the current paper only showcases self-calibration in the case of SoS, AF approaches may readily find broader applicability in calibrating other parameters in OA tomographic imaging systems. For instance, the position and orientation of ultrasound sensors is generally unknown, especially in self-developed systems, and must be calibrated in a first place. Selecting the most focused plane in the elevation direction around certain structures may also represent a potential application in the case of cross-sectional (two-dimensional) imaging systems. Finally, the behavior of the methods in three-dimensional OA imaging needs to be further analyzed.

In conclusion, similarly to optical microscopy techniques, focusing techniques are expected to play a fundamental role in the calibration of OA reconstruction parameters, particularly the SoS. The showcased performance of the suggested methods in cross-sectional imaging systems anticipates their general applicability for preclinical and clinical imaging with other geometrical configurations. Furthermore, the self-calibration of reconstruction parameters allows one to reliably reconstruct large datasets of whole animal imaging with minimal operator intervention – thus effectively addressing the problems of processing larger volumes of data, especially as OA progresses towards high throughput biological imaging applications [54].

2.3 Non-negative reconstruction using entropy measures

We have discussed in details the generation of OA signal in details in section 1.1. Based on our knowledge of OA signal generation, we may opine that, the optical absorption coefficient indicates the amount of light being absorbed by the tissue per unit length, the coefficients should take a positive value since negative values indicates light emitting materials not naturally occurring in biological tissues. Most state of the art reconstruction methods produce negative values arising due to different factors, such as the use of inaccurate inversion schemes, numerical errors, unknown or unpredictable experimental artifacts, or randomly generated noise in the imaging system. The presence of negative values in the reconstruction does not have physical relevance and ideally should be suppressed in the reconstruction process [76]. OA reconstruction is a source reconstruction problem; the standard image reconstruction involves minimizing the data-model misfit along with a smoothness constraint, which is popularly known as l2-norm based image reconstruction that employs a least-square QR (LSQR) based iterative inversion scheme [41]. Recent work has shown that applying a non-negativity constraint along with the smoothness constraint provides more accurate initial pressure rise distribution [77]. However, these methods rely on externally imposed non-negative constraint rather than on intrinsic image content. In an earlier attempt, Lu *et.al.* [77] has demonstrated that algorithms imposing non-negative constraints in model-based OA inversion and analyzed state-of-the-art non-negative constrained algorithms, *including* fast non-negative least squares, reflective Newton, projected quasi Newton and conjugate gradient methods, However, most of these implementations apply an additional non-negative constraint in the minimization. Researchers in the field of Positron Emission Tomography (PET) have demonstrated information theoretic approaches based on entropy for accurate image reconstruction in the context of multi-modal imaging [78, 79] and similar algorithms have been used extensively in the area of astronomical imaging [80]. Further, researchers have performed quantitative OA imaging by using a Bayesian image reconstruction [81].
In the current work, we propose a new entropy maximization approach for non-negative OA image reconstruction, and test its efficacy in providing enhanced reconstruction results in combination with nonlinear conjugate gradient minimization [82]. Entropy is the measure of randomness in the signal, and maximizing the entropy indicates least informative distribution [83]. The method relies on utilizing entropic measure (having a log parameter, which restricts the negative values) and outperforms current non-negative implementations in terms of actual quantification of OA tomographic data, i.e. in reconstructing absorption parameter. The proposed method allows us to obtain a correct absorption coefficient distribution, which could further aid the development of more accurate spectral unmixing algorithms [84, 85] to improve on quantitative representation of different chromophores within the imaged volume [76] .

Parts of the section is available as: Prakash, J.*, Mandal, S.*, Razansky, D. and Ntziachristos, V., 2017. Maximum entropy based non-negative optoacoustic tomographic image reconstruction. *arXiv preprint arXiv:1707.08391.*

2.3.1 Details of the method and experiments

Mathematical methods

The propagation of the acoustic pressure wave generated due to the short-pulsed light absorption is governed by the following inhomogeneous wave equation [86],

$$\frac{\partial^2 p(r,t)}{\partial t^2} - c^2 \rho \nabla . (\frac{1}{\rho} \nabla p(r,t)) = \Gamma \frac{\partial H(r,t)}{\partial t} \tag{2.16}$$

where the instantaneous light power absorption density in $\mathrm{W/m^3}$ is indicated by H and Γ represents the medium-dependent dimensionless Grüneisen parameter. In Eq. 2.16 the tissue density is represented by ρ while c indicates the SoS. For our experiments, a uniform SoS of 1520 m/sec was heuristically estimated using image AF methods [87, 74]. The solution for the wave equation can then be obtained using a Green's function by assuming $H(r,t) = H_r(r)\delta(t)$, which results in [86],

$$p(r,t) = \frac{\Gamma}{4\pi c} \frac{\partial}{\partial t} \int_{R=ct} \frac{H_r(r^{'})}{R} dA' \tag{2.17}$$

where $R{=}ct$ represents the radius of the integration circle. The above solution is subsequently discretized into the following matrix equation [88, 83],

$$b = \mathbf{A}x \tag{2.18}$$

where b is the boundary pressure measurements, $\mathbf{A}$ is the interpolated model matrix and x is the initial (to be reconstructed) pressure rise distribution. The above formulation represents the forward model, i.e. given the initial pressure rise one can estimate the pressure at the boundary locations detected by the transducers. Thus, the acoustic inverse problem involves reconstructing the initial pressure rise given the boundary pressure data. Typically the inverse problem is solved by minimizing the data model misfit along with a smoothness constraint given as,

$$\Omega = ||\mathbf{A}x - b||_2^2 + \lambda ||x||_2^2 \tag{2.19}$$

where the regularization parameter is represented as λ and is automatically chosen using the L-curve method. The objective function (given in Eq. 2.19) is minimized using an iterative LSQR based method, which has the closed form solution indicated as,

$$x \approx x_{l2-LSQR} = V_k((B_k^T B_k + \lambda I_k)^{-1} \beta_0 B_k^T e_1) \tag{2.20}$$

where B_k, V_k, β_0, and e_1 can be obtained in the Lanczos diagonalization procedure with A and b. The obtained solution contains negative values which could be thresholded to 0, as negative values do not have any physical relevance. Mathematically, entropy maximization is similar to maximizing the log likelihood of the function. It is a non-linear convex maximization problem and the equivalent minimization is described via
,

$$\Omega = ||\mathbf{A}x - b||_2^2 + \lambda x^T log(x) \tag{2.21}$$

where $-x^T \log(x)$ indicates the entropy function [from duality maximizing $-x^T \log(x)$ indicates minimizing $x^T \log(x)$]. The objective function given in Eq. 2.21 is minimized using a non-linear conjugate gradient type method and the step-length for the conjugate gradient method is computed using a line search[89]. The derivative used in the conjugate gradient scheme is computed as,

$$\nabla\Omega = 2A^T(\mathbf{A}x - b) + \lambda(1 + log(x)) \tag{2.22}$$

The minimization is presented in more details in the *Algorithm-1.*

As mentioned earlier, the reconstructed initial pressure distribution is proportional to the absorption coefficient distribution and the fluence (light intensity distribution). The fluence distribution has a smooth variation in the image domain; moreover it has a non-linear relation to the optical absorption and optical scattering, which can be modeled using a diffusion equation [90]. Since the fluence is varying with depth, the reconstructed initial pressure rise does not have a direct correlation to the absorption coefficient value, hence it is necessary to model the light propagation and to correct for the depth-dependent fluence. By assuming the Grüneisen coefficient to be constant and normalized to 1, the relation between the absorbed energy distribution $H_r(r)$ and optical absorption coefficient $\mu_a(r)$ can be formulated as,

$$p_0(r) = H_r(r) = \mu_a(r).\Phi(r) \tag{2.23}$$

where $p_0(r)$ is the initial pressure rise distribution and $\Phi(r)$ indicates the local light fluence density in J/m^2. The light propagation is modeled using the diffusion equation, further assuming that scattering dominates over absorption [90] (true for most biological tissues) as,

$$-\nabla.[D(r).\nabla\Phi(r)] + \mu_a(r)\Phi(r) = S_0(r) \tag{2.24}$$

where $D(r) = \frac{1}{3(\mu_a + \mu_s^{'})}$ is the diffusion coefficient and $\mu_s^{'}(r)$ indicates the reduced scattering coefficient at position r. $S_0(r)$ indicates the light source at the boundary of the imaging domain. Eq. 2.24 is used for fluence estimation, and the diffusion equation is solved using the finite volume method (FVM) with known values of absorption and scattering coefficients [91]. Further, we obtain absorption coefficient maps by canceling out the calculated fluence distribution [92].

Application of traditional fluence correction measures often produces discrepancies in image contrast, especially between the conductive medium (background) and tissue (region of interest). These anomalies can be attributed to inaccurate modeling as the same wave equation and diffusion equation are employed for performing the correction. In reality, the light fluence in conducting medium (water) is significantly higher compared to the light fluence in the tissue (high absorption, signal attenuates with depth). To correct for this effect we introduce a hybrid two compartment model (Beer-Lambert Law and diffusion Equation solution) by incorporating segmented image priors. We assign a low attenuation (high fluence) to the background in accordance to the Beer–Lambert law, and apply the light propagation model (as in Eq. 2.24) within the segmented tissue sample. The entire workflow of segmentation and fluence correction (as shown in 2.6)

Algorithm 1 Entropy Maximization Algorithm

Inputs: Obtain boundary pressure data b, Build the interpolated model matrix A, Regularization Parameter λ, Maximum Iteration *max_iter,* Iteration Number $iter = 0$, Initial Guess x_0 *Output:* Reconstructed initial pressure rise x

1. Compute Gradient g(x) = $2A^T(Ax_0 - b) + \lambda(1 + log(x_0))$, Residue r = $Ax_0 - b$, p = -g, $\Phi_0 = p^T\ g$; $x_{prev} = x_0$; $g_{prev} = g$
2. Repeat until *iter*<*max_iter*
   a) $A_p = A * p, \gamma = {A_p}^T A_p, v = A^T A_p$
   b) Perform line search based on secant method to estimate optical α by having minimum of $p^T g(x + \alpha p)$ (At the end of iteration)
      - $\Phi = \Phi_0 + \alpha\gamma + \lambda p^T(1 + log(1 + \frac{\alpha p}{x_{prev}}))$; optimal αis determined using root finding. $g_{temp} = g_{prev} + \lambda(1 + log(1 + \frac{\alpha p}{x_{prev}})) + \alpha A^T A_p$
      - $\beta = (g_{temp}^T g_{temp} - g_{prev}^T g_{temp})/(\Phi - \Phi_0)$
      - $u = -g_{temp}^T g_{temp} + \beta\Phi$
   c) $g_{prev} = g_{temp}$; $\Delta x = \alpha * p$; $x_{prev} = x_{prev} + \Delta x$; $p = -g_{prev} + \beta * p$; $r = r + \alpha * Ap$; $\Phi_0 = p^T g$
3. Solution is given as x=x_{prev}

is integrated with the proposed non-negative entropy maximization algorithm to render improved image quality. More details of the method and a discussion about its use OA imaging is illustrated in the section 3.4.

Experimental methods

Experimental data were acquired using the commercial MSOT scanner (MSOT256-TF, iThera Medical GmbH, Munich, Germany) [2]. To verify the quantitative reconstruction capabilities of the proposed entropy maximization scheme, a star shaped (irregular) phantom was created. The phantom constituted of a tissue mimicking (7% by volume of Intralipid and calculated volume of diluted India ink added) agar core having the optical density of 0.25. Two tubular absorbers made up of India-ink with the absorption coefficient values of 2.5 OD (calibrations done with Ocean Optics USB 4000) were inserted in the phantom. The absorber were placed at two different depths within the phantom (one at the center and the other at the edge of the imaging domain) to test the sensitivity of the proposed scheme in reconstructing the absorbers at different imaging distances from the sensing arrays. Under normal operating conditions, the fluence at the center of the imaging domain is significantly lower as compared to the edge of the imaging domain owing to the optical attenuation of the incident irradiation. Hence, performing fluence

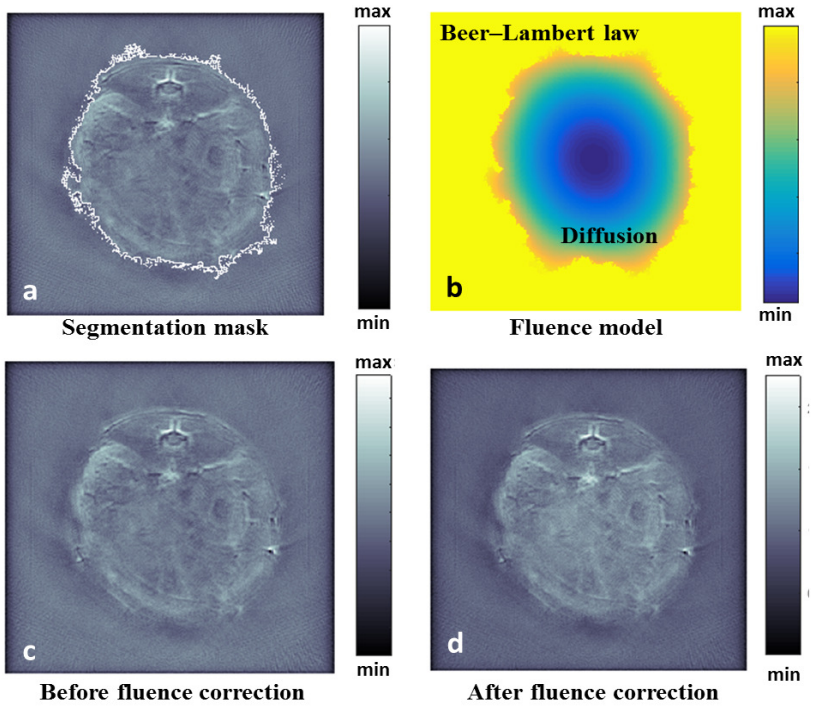

Figure 2.6: Workflow of prior based fluence correction using non-negative image reconstruction (a) segmentation mask generated by active contour method, (b) optical fluence field generated by using FVM model and application of bi-compartment Beer-Lambert Law and Diffusion equation; images reconstructed using entropy based non-negative method (c) before fluence correction and (d) with integrated imaging prior based fluence correction.

correction becomes indispensable to assign appropriated intensity to the absorber at the center of the imaging domain. The proposed methods were further validated on the *in-vivo* mouse abdomen and brain datasets drawn from a standardized *in-vivo* murine whole body imaging database (10 mice/30 anatomical datasets) previously developed by Mandal *et. al* [87]. The selected images were obtained at a laser wavelength of 760 nm, and the water (coupling medium) temperature was maintained at $34°C$ for all experiments. All animal experiments were conducted under supervision of trained technician in accordance with institutional guidelines, and with approval from the Government of Upper Bavaria.

2.3.2 Reconstruction results: Phantom and in vivo imaging

Fig. 2.7 shows reconstructions of the star phantom, which reveal the efficacy of the proposed method vis-à-vis traditional LSQR based reconstruction in generating positive values for both the initial pressure rise and absorption coefficient distribution. The reconstructed initial pressure rise and absorption coefficient distribution using the l2-norm based reconstruction is shown in Fig. 2.7(a) and 2.7(d) respectively. The reconstructed

initial pressure rise and absorption coefficient distribution using the l2-norm based reconstruction (with non-negative constraint) is indicated in Fig. 2.7(b) and 2.7(e) respectively. The reconstructed initial pressure rise and absorption coefficient distribution using the entropy maximization based approach is represented in Fig. 2.7(c) and 2.7(f) respectively. The non-negative based LSQR reconstruction is able to generate reconstruction results with positive values, but is not able to correctly reconstruct the internal volume of the star (tissue mimicking agar) phantom. Fig. 2.7 clearly demonstrates that the maximum entropy based scheme is able to deliver better contrast than the standard LSQR based reconstructions. The fluence correction was performed by using segmented (boundary) priors obtained automatically using deformable active contour models [93].

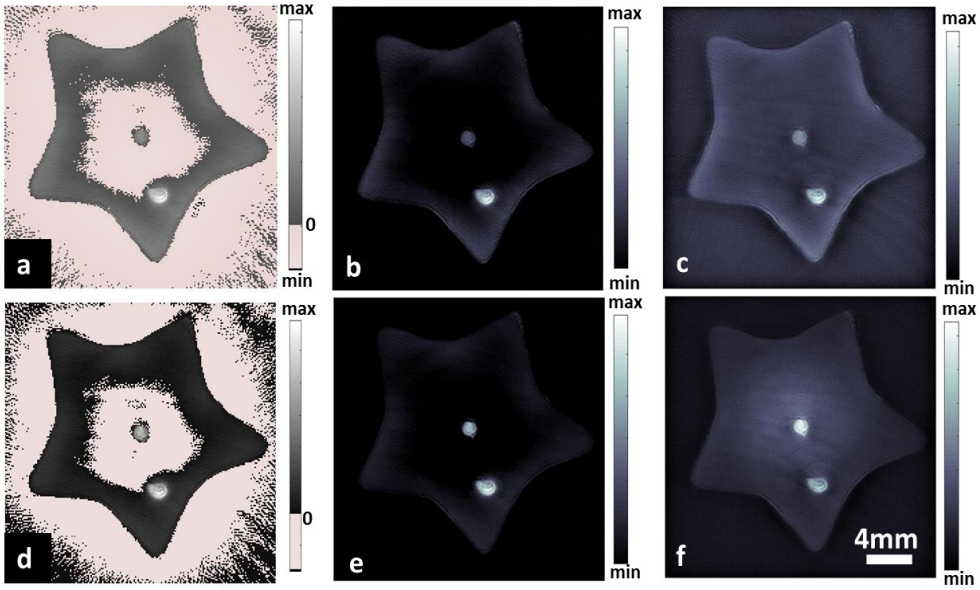

Figure 2.7: Reconstructed OA image of star phantom using the (a) l2-norm based reconstruction, (b) l2-norm based reconstruction with thresholding, (c) entropy based reconstruction. Absorption coefficient distribution after fluence correction using (d) l2-norm based reconstruction, (e) l2-norm based reconstruction with thresholding, (f) entropy based reconstruction. The negative values are plotted in a different colormap (a and d) for visualization and normalized colormaps indicate initial pressure rise (in a.u).

The maximum entropy based scheme depends on the initial guess given to the nonlinear conjugate gradient scheme. The maximum entropy constraint involves a nonlinear logarithmic term, and logarithm of a negative value results in an imaginary term, therefore having a positive value at the initial guess always generates positive reconstruction distributions and thus plays an important role in intrinsically obtaining non-negative reconstruction. The reconstruction results corresponding to the initial guess ($A'b$) is indicated in Fig. 2.8(a). The reconstruction results corresponding to the initial guess $((||b||2/||A||1) * ones(N, 1))$ is indicated in Fig. 2.8(b). Fig. 2.8 clearly indicates that the negative values in the reconstructions arises because of ini-

tial guess i.e. $(||b||2/||A||1) * ones(N,1)$ gives non-negative results while $A'b$ results in negative values. Hence, in all the reconstructions the initial guess was chosen to be $||b||2/||A||1) * ones(N,1)$ and the regularization parameter was set at 10. Note that reconstructions in Fig. 2.8 did not involve performing additional fluence correction steps.

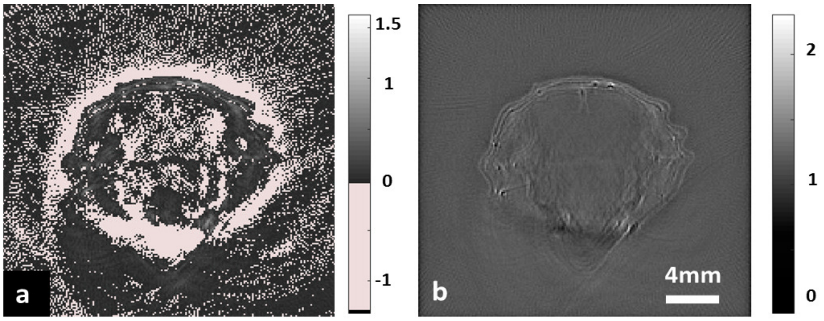

Figure 2.8: Reconstructed OA image of mouse brain (head scanned *in vivo*) using two different initial guesses,(a) A'b (-ve values exists at initial guess) generates negative values and (b) $(||b||2/||A||1) * ones(N,1)$ (only +ve value exist at initial guess) yields non-negative image. The negative values are plotted in a different colormap in (a) for visualization, colorbars indicates the rise of initial pressure (in a.u).

The reconstruction results pertaining to the mouse head and mouse abdominal regions using the standard and proposed method are shown in Fig. 2.9. The reconstruction result corresponding to l2-norm based scheme (solved using LSQR method) for the mouse head and abdominal region is indicated in Fig. 2.9(a) and 2.9(d) respectively, and the corresponding results for l2-norm based non-negative scheme (solved using LSQR method with thresholding) are given by Fig. 2.9(b) and 2.9(e) respectively. The reconstruction results using the maximum entropy maximization approach (*Algorithm-1* with the integrated hybrid fluence correction) for the same anatomical regions is shown in Fig. 2.9(c) and Fig. 2.9(f) respectively. All the reconstructions were performed on a 200x200 pixel imaging domain which corresponds to a physical field of view of 20mm x 20mm. The regularization parameter was set to 10 in all the maximum entropy based reconstructions. Also the optical properties was assumed to be homogeneous inside the tissue and taken from literature [91].

2.3.3 Discussion

The reconstruction results for the star-shaped phantom and *in vivo* mouse scans indicate that the proposed entropy maximization scheme renders strictly positive image values that are comparable to the a-priori known absorption values in the phantom. Employing a segmented image prior can effectively reduce the aberrations in image contrast by suitably mapping the light propagation pathway in two optically diverse domains (background and tissue), and enhance the performance of (optical) fluence correction methods [92, 93], as demonstrated in Fig 2.7(f) and 2.9(f). Moreover, when a global SoS is attribute to the entire imaging domain, small SoS variation causes aberration at the

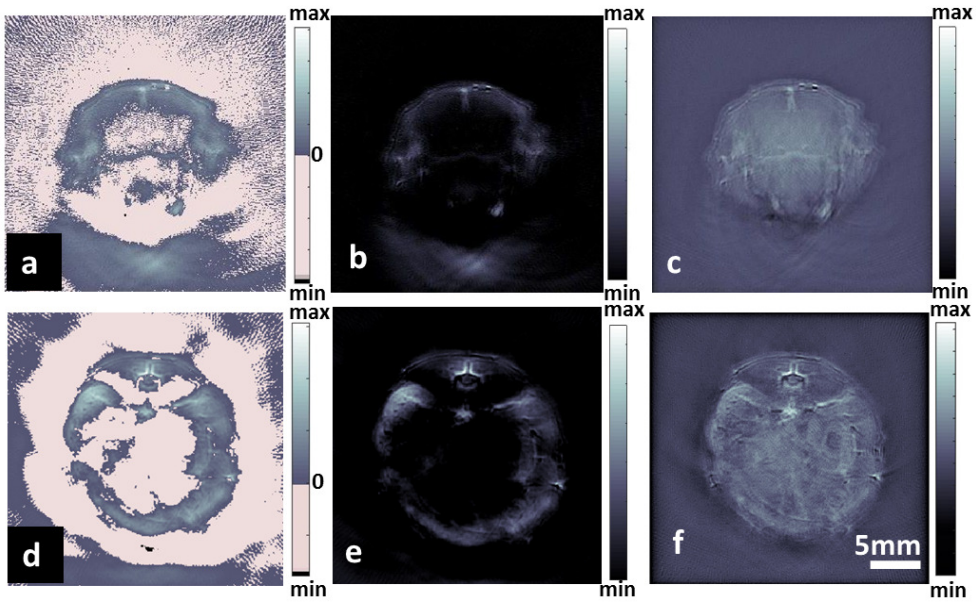

Figure 2.9: Reconstructed OA images using the (a) l2-norm based reconstruction, (b) l2-norm based reconstruction with thresholding, (c) entropy based reconstruction and fluence correction (using segmented prior) of murine head region; and (d) l2-norm based reconstruction, (e) l2-norm based reconstruction with thresholding, (f) entropy based reconstruction (using segmented prior) for the mouse abdominal region imaged in vivo. The negative values appearing in l2-norm based reconstruction scheme (a and d) are plotted in a different colormap (negative values marked in pink) for visualization, colorbars indicates the initial pressure rise (in a.u). An 8 week old nude mice (CD-1® Nude, Charles River Laboratories, Germany) used imaged at an wavelength of 760 nm (brain) and 800nm (abdomen).

edge of the surfaces of the imaged object, the same two compartment model can be used to remove SoS mismatch if needed.

The proposed method preserved the structural integrity (star phantom) and the anatomical structures (mouse data), and was successful in correcting the effects of variations in optical fluence. Moreover, the entropy maximization scheme performs faster than the standard LSQR based image reconstruction. For a typical case (200 x 200 px) the maximum entropy based scheme converges in 3 seconds versus 5 sec for the LSQR based scheme. As part of future work, we aim to integrate the entropy maximization with more accurate light propagation modeling, such as Monte Carlo based schemes, to obtain better representation of the absorption coefficient with the reconstruction process accelerated by means of graphics processing units. The proposed scheme demonstrates superior reconstruction performance with no visible distortion of anatomical structures associated with delivering of non-negative pixel values. Entropy maximization reconstruction thus tends to be physically relevant and more accurate, and has the potential to emerge as a suitable data processing tool for quantitative OA imaging.

2.4 Conclusion

In this chapter, we have outlined the OA image reconstruction algorithms used for the dissertation work, viz. backprojection and model-based (IMMI) methods. Thereafter, we have developed novel multipurpose AF algorithms which can be employed not only for self- calibration of SoS in OA reconstructions, but also to correct for SoS anomalies caused by drifting temperature with time, and slice selection for image evaluation. Further, we presented an entropy maximization based approach that employs a logarithmic regularization term for non-negative tomographic OA inversion. Experimental validation of both the algorithms was carried out on phantoms and *in vivo* samples was carried out on benchmark datasets.The developed methods are instrumental in automating reconstruction procedures for large image datasets, and enabling quantitative imaging.

3 Improving image reconstruction using segmentation priors

Segmentation has emerged as one of the most important tools in medical imaging and image analysis, and has been widely used for various purposes ranging from improving image reconstruction to target volume delineation for pathological conditions. Accurate image segmentation is generally considered a challenging task in image processing [94]. In spite of the difficulties, segmentation represents an efficient tool to improve inversion algorithms. For example, segmented X-ray computed tomography (XCT) priors have been used to improve fluorescence molecular tomography (FMT) reconstructions [95]; segmented magnetic resonance (MR) images have been used as priors for attenuation correction in positron emission tomography (PET) [96], and for improved stability and faster convergence of optical tomography [97].

Research efforts in OA have been directed towards the development of new hardware components and inversion methodologies allowing increasing imaging speed and resolution, as well as on investigating potential biomedical applications. Recently developed cross-sectional tomographic OA systems enable whole-body small animal *in-vivo* imaging, and the unique capabilities opened up the unexplored domain of post-reconstruction image analysis for the modality[2]. Researchers have shown that manual segmentation of images is useful to improve the quantification performance of OA reconstructions under heterogeneous illumination conditions [46] and in presence of strong acoustic reflections [98]. However there exists a gap in development of automated segmentation methods and its integration with OA inversion methods, which we aim to address in this dissertation.

3.1 Motivation

Segmentation of OA images is essential for both anatomical characterization and enhancement of the image reconstruction performance. For instance, properly selected focus measures applied to the different parts of the reconstructed image can be used as a feedback mechanism to adjust the speed of sound (SoS) of the medium or other reconstruction parameters. Image segmentation further enables identification of areas

This chapter has been adapted with minor modifications from the following published articles:

[1] **S. Mandal**, X. L. Deán-Ben and D. Razansky, "Visual Quality Enhancement in Optoacoustic Tomography Using Active Contour Segmentation Priors," in IEEE Transactions on Medical Imaging, vol. 35, no. 10, pp. 2209-2217, Oct. 2016.

[2] **S. Mandal**, P. Viswanath, N. Yeshaswini, X. Deán-Ben and D. Razansky, "Multiscale edge detection and parametric shape modeling for boundary delineation in optoacoustic images," 2015 37th Annual International Conference of the IEEE Engineering in Medicine and Biology Society (EMBC), Milan, 2015, pp. 707-710.

corresponding to different acoustic or optical properties. Mandal *et. al.* [87] have previously shown that accounting for differences of SoS and attenuation between the imaged tissues and surrounding coupling medium (water) can improve imaging performance. Researchers have used hybrid measurement approaches (passive ultrasound and optoacoustics) to account for acoustic heterogeneities [53], and accurately reconstruct OA images. However, the methods render non-uniform resolution and require additional instrumentation. Born ratio-based OA image normalization has been suggested to correct for the heterogeneous light fluence distribution [99, 100], but the approach is not applicable for accounting for small SoS variations. Accounting for strong acoustic heterogeneities can mitigate image artifacts associated with acoustic reflections and scattering in biological tissues [101]. Additionally, identifying boundaries of regions with different optical properties is important for estimation of the light fluence distribution, which is essential for a quantified assessment of chromophore concentration in deep tissues [92]. An automated segmentation process can thus be integrated with advanced inversion algorithms to obtain more accurate reconstructions of the actual distribution of chromophores. In OA imaging, the task of segmentation is oftentimes exacerbated by the relatively low intrinsic contrast of large anatomical structures, having a much lower haemoglobin concentration than in major blood vessels, and is further impaired by the limited angular coverage of some commonly employed tomographic imaging configurations. Yet, proper segmentation of boundaries is essential to improve the quantitative performance and overall image quality of OA reconstructions. Even when considering relatively homogeneous tissue samples, accurate identification of the outer boundaries is essential for a proper assignment of acoustic and optical properties of the imaged region of interest and the background (coupling) medium [55].
The dissertation work investigates the applicability of multiscale segmentation algorithms and active contour models [102, 103] for boundary segmentation in OA tomography (OAT). Specifically, the segmented boundary information is used to aid automated fitting of the SoS values in the imaged sample and the surrounding water. A reconstruction mask is further used for quantified mapping of the optical absorption coefficient by means of light fluence normalization. The performances of segmentation proposed algorithms for cross-sectional OA images and the associated benefits in image reconstruction are demonstrated in phantom and small animal imaging experiments.

3.2 Multiscale segmentation and parametric curve fitting

Segmentation is one the most challenging tasks in image processing, and the relatively low intrinsic contrast of background structures (compared to natural images) and limited view problems of OAT increase the complexity involved. Classical experiments on non-human primates demonstrate that complex objects are perceived by vision system in a multiscale manner, and are tuned from course scale to finer scales [104], we use the information as a basic assumption in our study. For the edge detection at individual scales, the Sobel operator, which approximates the gradient of the image intensity function, or the Canny edge detector [105] which uses a feature synthesis step from fine to

course scales, are commonly employed. Multiscale edge detection, a rich area of interest in itself, can enhance the performance of edge detection in a fixed (original) scale. For example, the Perona-Malik flow (anisotropic diffusion)[69] gives a successful formulation of scale-space adaptive smoothing function, leading to better preservation of edges while achieving a better noise performance. These edge detection methods have been demonstrated to be useful for OA images and employed for calibration of reconstruction parameters by Mandal et.al.[87]. More sophisticated techniques were proposed by Tabb and Ahuja [106] and followed by Ma and Manjunath [107]who developed the concept of designing a vector field for edge detection. In [106] the vector field is created by analyzing the neighborhood of a pixel, where the size and spatial scale of the neighborhood were determined heuristically by an homogeneity parameter, and is adaptively determined on a pixel to pixel basis. The edge flow method suggested by [107] utilizes the color and textural information of images to track changes in directions, creating a vector flow. This method detects boundaries when there are two opposite directions of flow at a given location in a stable state. However, it depends strongly on color information and requires a user defined scale to be input as a control parameter. In a follow up work by [104], a methods was demonstrated which eliminates the need of scale selection and potentially works with gray-scale images. Given the nature of OAT images, this method indeed serves as a foundation for the edge detection algorithm introduced herein. The suggested multiscale edge detection method and morphological image processing is described in 3.2.1, and the processing results of OAT images are displayed in 3.2.2.

3.2.1 Segmentation algorithm

3.2.1.1 Edge-flow vector field and edge detection

The general trend in multiscale edge detection is to define a scale a-priori and then estimate the scale locally, however, Sumengen and Manjunath [104] suggested a geometrically inspired method that estimates the edges that exists both in course and fine scales, and localize them in the fine scale. We redesigned the algorithm outlined in [107, 104] for convenient application in OAT images. The edge flow algorithms define a vector field, such that the vector flow is always directed towards the boundary on both its sides. The classical edge flow model utilizes a vector propagation stage. In the current method, similarly to [104], the relative directional differences are considered for computing gradient vector. The gradient vector strengthens the edge locations and tracks the direction of the flow along x and y directions. The search function looks for sharp changes from positive to negative signs of flow directions and whenever it encounters such changes, the pixel is labeled as an edge point. The magnitude of the change is the deciding factor behind the edge strength, which is reflected as edge intensity in the final edge map. The vector field is generated explicitly from fine to course scales, whereas the multiscale vector conduction is implicitly from course to finer scales. Thus, the algorithm is suitable for localizing the edges in the finer scales, which is achieved by preserving only the edges and neighborhoods that exists in several scales (depending on the threshold employed),

and suppressing features that disappear rapidly with increment of scales. The workflows for the vector field generation and morphological processing are illustrated in the Algorithm 2. The pseudocode further outlines the process of geometric curve fitting. In the current implementation, the Gaussian offset (σ) is also lowered for the gray-scale OAT images. For the acquired *in vivo* OAT images, optimum performance was achieved with $\sigma = 3$. We analyze the images between scales s=1, and s=3, where s=1 is the starting (finest) scale (Fig. 3.1). The interval is sampled at sub-pixel resolution [$\Delta s = 0.5$] for tracing the dislocation of edges in subsequent edges, as used by Berghold [108].

Algorithm 2 Multiscale Edge Detection and Curve Fit

$I(x,y) \leftarrow$ image
$s_1, s_n \leftarrow$ smallest and largest scale of the image respectively
$\Delta s = 0.5$ be the sampling interval for each scale
$s = s_1$ ▷ initialize book keeping
$\vec{U}, \vec{U}_{new} \leftarrow \nabla I(x,y)$ ▷ Gradient Vector
while $s_1 < s_n$ **do**
  $s \leftarrow s + \Delta s$
  $M \leftarrow max(\| \vec{U} \|)$
  $\vec{U}_{new} \leftarrow \nabla I(x,y)$ at scale s
  for `<each pixel in image>` **do**
    if $\| \vec{U}(x,y) \| < M/C$ **then** ▷ C is thresholding constant
      $\vec{U}(x,y) = \vec{U}_{new}(x,y)$
    else if $abs(arctan(\vec{U}(x,y), \vec{U}_{new}(x,y))) < \pi/4$ **then**
      $\vec{U}(x,y) = \vec{U}(x,y) + \vec{U}_{new}(x,y)$
    else
      $\vec{U}(x,y) = \vec{U}(x,y)$
end {if, for, while}
The final $\vec{U}$ is the edge flow vector we are interested in
$\vec{U} \leftarrow Binarize(\vec{U})$
Enhance $\vec{U}$ by performing morphological operations
for `gradient magnitude image in scale` s_n **do**
  if $n \geq 2, use\ strel- > 0px, disc$
  else ▷ structural element(strel)
    $strel- > 1px, disc$ **then**
  Apply **Erosion** operation; **Close** to recover edges
end for
Obtain centroids from *binary* edge-map
Outliers (centroid positions) removed by applying median filter
Obtain minBoundCircle and minBoundEllipse considering centroids as data points to be enclosed

The algorithm searches the edges in finer scales and strengthen them with the edges recovered from higher scale. The homogeneous regions have vectors of zero length, so the detected edge segments grow in thickness (and often strength) as we move from lower

to higher scales. Some edges do not exist in lower scale, but can still be significant. To decide on the same and reduce noise we put a boundary condition - and when the maximal edge strength (M) is greater than a heuristically predefined constant (C) -the edges are retained, or else they are discarded.

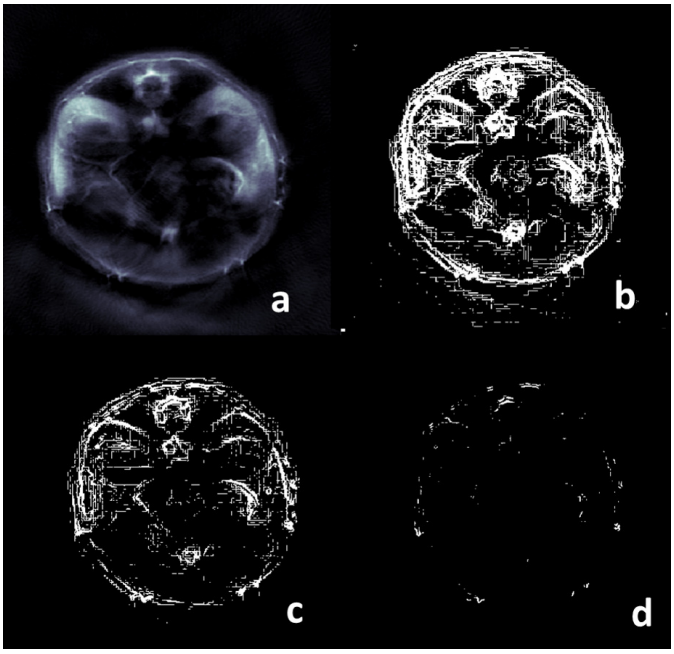

Figure 3.1: Reconstructed optoacoustic image using non-negative constrained model based inversion (a), and (b-d) edges detected at multiple scales $s = 1, 2, 3$ respectively using diffused edge-flow model.

3.2.1.2 Morphological edge enhancement

The primary objective of applying a edge detection is to delineate the boundary of the imaged object and differentiate it from the background. But often in OA, the signal originate from the impurities or inhomogenities withing coupling medium. Further, noisy background is present in reconstructed images (lower boundary in Fig. 3.1.a) due to limited view, and shortcomings of inversion methodologies. This noises are often strong enough to be detected by edge detection algorithm as true edges. Thus, a non-linear morphological processing is done on the binary edge mask obtained from the edge detection process. We take an sub-pixel sampling approach (0.5 px), rendering the operation is redundant beyond the second scale level. The morphological mask should be differentially choosen at different scales. Initially, the image is eroded with a disc structuring element to remove noisy patches, but it also thins the edges. To recover the edges a closing operation is executed, with smaller structural element for erosion and a bigger element (2px) for dilation.

3.2.1.3 Parametric shape model fitting

Delineating the tissue boundaries in OAT, provides additional challenges due to illumination conditions and limited view considerations in the detection, the reconstructed images can be affected by open edges and fuzzy boundaries. Traditional edge linking algorithms may then fail to provide satisfactory segmentations. Thereby, we suggest a novel curve fitting model that delimits the tissue-background boundaries in OAT images. We further characterize the goodness of fit (GoF) by several accepted evaluation metrics. We use the GoF and use additional image filtration techniques to iteratively improve the performance of the fit.
In section 3.2.1.1 we discussed about detection of edges, and several authors have utilized the edge-flow vector for segmentation. In OAT images we see formation of smaller edge clusters and open contours. Thus, getting an ideal segmentation using edge linker seem to perform poorly. However, given the fact that our current problem requires segmenting the image into only two classes - image and background, we follow a simple curve fitting approach. The proposed method first generates the centriods for edge clusters and then try to fit on a geometric pattern (deformable ellipse) iteratively through a set of parametric operations. A typical scenario in curve fitting is when the data is a best fitted, but some data points lies outside the curve, as we take an interpolated spline fitting criterion. In our approach, we modeled an inclusion criterion which enclosed all centroids and create forms a closed curve. Theoretically, it draws a convex hull with the centroids on a perimeter and approximate it to the nearest curve. In some datasets, we see presence of the outlier centroids which significantly biases the curve (due to presence of the inclusion criterion) leading to erroneous fitting. To avoid such complications, the values of the centroid positions are filtered for squeezing out outliers through a median filter, and then analyzed for generating the shape models which match the object boundary.

3.2.1.4 Goodness of fit

The goodness of fit is calculated using the average Dice coefficient metric (DM), which is a measure of contour overlap utilizing the area under the fitted curve (A), manually segmented region (M), and their intersection. DM always vary between 0 and 1, with DM ≥ 7 being considered a good segmentation[109]. The DM can be expressed as:

$$DM = \frac{2 \mid (A \cap M) \mid}{\mid A \mid + \mid M \mid} \tag{3.1}$$

The mean perpendicular distances (meanPD) between A and M are also shown for comparison in section 3.2.2.

3.2.2 Experimental studies and results

For testing and standardization of the introduced image processing framework, a database of 30 datasets for 3 different anatomical regions in mice (10 for each region) was created. Each individual dataset represents signals (averaged 10 times) acquired at up to 6

Table 3.1: Efficacy of Curve Fitting (Multiscale segmentation)

	Dice Coefficient Metric		
Regions	w/o medfilt	w medfilt	meanPD(mm)
Brain	0.9387	0.9440	1.4679
Liver	0.9093	0.9447	1.1819
Kidney/Spleen	0.9606	0.9571	1.5141

different positions and at 8 different wavelengths (between 690-900 nm). Since manual segmentation of each dataset was needed for computing the performance of the algorithm vis-a-vis ground truth, the number of datasets was scaled down. Thereby, 2 datasets were considered from each anatomical regions, namely brain, liver and kidney/spleen, for computing the goodness of fit parameters. The proposed algorithm demonstrated good edge recovery performance. As shown in Fig. 3.1, the algorithm weighted the edges that appear in multiple scales and reduced the spurious edges. The assumption made by [107] is that if the vector direction change matches in multiple scales, then we can infer that it corresponds to real edges. Thus, the vector directions were checked in both finer and courser scales, in a way that when there is a match, the designated edges were strengthened. The construction of the algorithm allows to detect the initial edge points from the finer scales, and reinforce then as we move to the larger scales. The finer scales are more immune to noise and the use of a non-negative constrain during the image reconstruction process prevents unnatural movement of the vector field (potentially due to absence of undesired negative values). Thus the edges detected in the finer scales are very significant to recover object boundaries, and are helpful in segmentation of OAT images. In Fig. 3.2, we show the performance of multiscale segmentation along with the edge map recovered using Sobel operator (Fig. 3.2.b). The improvement in the edge detection performance by considering multiple scale (as over single scale in Sobel) in evident in the combined multiscale edge map ($\sigma = 1 - 3$). Further, a closer observation reveals that the morphological processing have successfully eliminated the spurious edges formed beyond the tissue boundary (Fig. 3.2.d) Finally, in Fig. 3.2(e-f) we show the calculated centroid clusters obtained from the morphologically processed binary edge map, and the ellipse fitting model applied to this centroids respectively.

Thereafter, we computed the goodness of fit using quantitative measures, viz. Dice coefficient and mean probability distribution (meanPD), with ground truth (manual segmentation) as reference. In Table 1 we show the performances of the curve fitting using the DM (2). Theoretically, DM values above 0.7 are considered to represent a good segmentation result, and using the proposed methodology DM values between 0.90 and 0.96 were achieved. Medial filtering was used to improve noise performance when outlier centroids are present, and further improvement in the DM values was observed in most regions, except for the kidney/spleen zone where the DM decreased after median filtering, although DM values above 0.95 both with and without secondary filtering were achieved (Fig. 3.3).The meanPD is calculated (in mm) for a total effective imaged area of 20x20 mm, the image being produced by reconstruction of OA pressure waves.

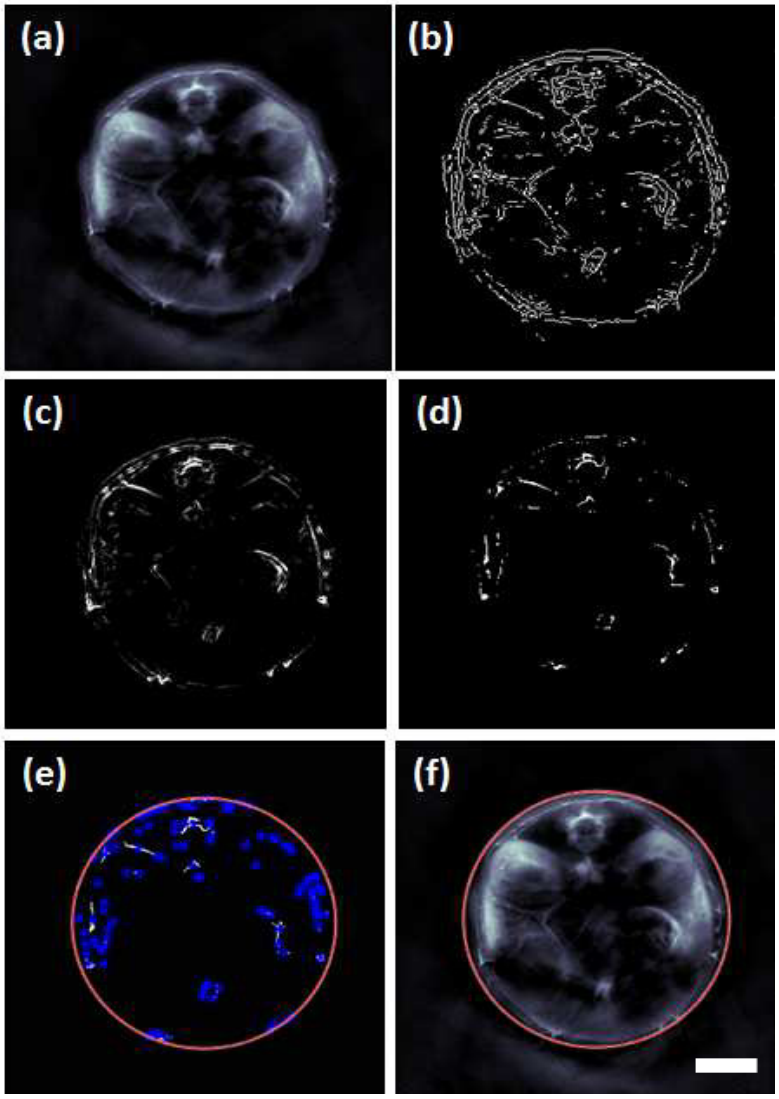

Figure 3.2: Reconstructed Optoacoustic image with non-negative constrain(a), edge-maps generated by Sobel operator (b), Multiscale (Edgeflow) map (c) and (proposed) Morphological processed multiscale edge map (d) are shown. In (e) computed centroids from edge clusters are shown in blue, and (f) illustrates the curve fitting method applied to the centroids (fitted curve marked in red). [Scale = 3mm]

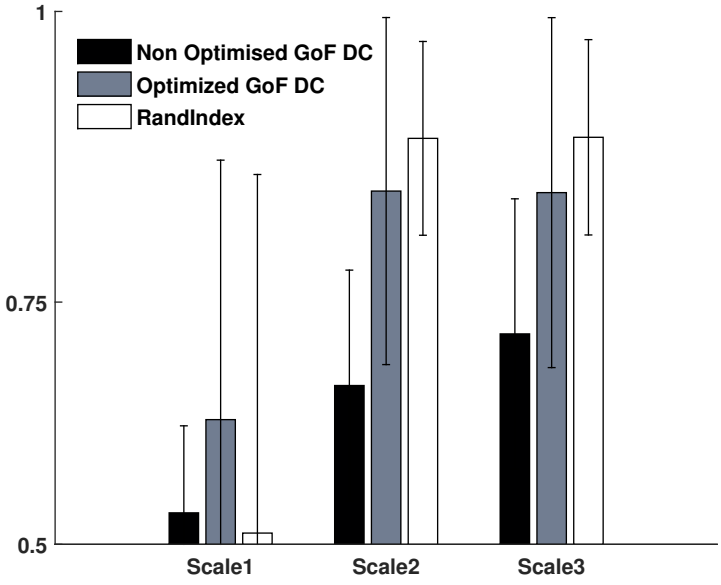

Figure 3.3: GoF trace and the standard deviation for the torso(kidney/spleen region) scans of mouse. (Total dataset size = 12 (z-slices in whole body small animal tomographic scanner), acquired from 2 different mice) *in-vivo*

Thus, the proposed method for delineating the boundary of OA small animals images using a multiscale edge detection algorithm in combination with geometrical curve fitting performs with high accuracy and low time complexity, suited for fast image segmentation.

3.3 Active contour models for segmentation

Active contour, also referred to as snakes, is a deformable model widely used in image analysis applications given its flexibility and efficiency [102, 110]. Snakes are generally interactive in nature and demand user input or an initial guess, followed by movement of a curve towards the boundary of the object of interest. The mathematical formulation behind the snakes is an energy-minimizing spline, with an associated 'snake energy' as a cost function. The spline is guided by external constrain forces and influenced by image forces which oblige it to converge towards dominant features like lines or edges.

3.3.1 Theory of active contour models

In the current study, the classical snake model is used. It involves a controlled continuity spline representing a generalization of Tikhonov stabilization, which can be visualized as a regularization problem [43, 89, 111]. The governing forces for curve evolution are: (a) image forces E_{image} that push snakes towards the edge feature and contours, (b) the internal energy E_{int} enforcing a piecewise smoothness constraint, and (c) the external

constrained forces E_c that put the snakes closer to appropriate local minima. Thus the total energy of the image can be expressed as,

$$E_{snakes}(s) = E_{image}(s) + E_{\text{int}}(s) + E_c(s) \tag{3.2}$$

where s encodes the parametric snake representation. The optimum snake is then obtained as

$$s_{opt} = \arg_s \min E_{snakes}(s) \tag{3.3}$$

It should be noted that E_{image} is purely data driven, whereas E_c is defined by user interactions. As E_{image} is influenced by the nature of the image, it needs to be carefully calibrated. In our case, calibration is achieved by using the energy functional as proposed by Kass *et al.* i.e.,

$$E_{image} = w_{line}\ E_{line} + w_{edge}\ E_{edge} + w_{term}\ E_{term} \tag{3.4}$$

where E_{image}, E_{int} and E_c are the energy functionals and w represents the corresponding weights. Further, a morphological image processing sub-unit was added to the image segmentation workflow to generate smoother boundaries [112]. The morphological processes utilized a disc shaped structuring element with 2 pixel diameter. Closing operations were carried out on the segmented (binary) image mask to plug any spurious holes or irregular edge inundations that might be present in the mask due to limited view problems.
Deformable models and active contour segmentation is in itself a highly investigated area in image analysis and several advanced methods viz. active contour without edges [113], localized region based active contours [114], geodesic methods [115] etc exist. However, we limit our current investigation to the classical model postulated by Kass *et al.* and design an efficient workflow with the existing algorithm to achieve the goal of segmenting MSOT images and using this information as prior for mapping optical and acoustic inhomogeneity, ultimately leading to better imaging performance.

3.3.1.1 Mathematical formulation of active contours

In our study we implemented the point snake model, proposed by Kass et al [21] which employs an elementary representation of discrete curves, and satisfy a n-neighbor connectivity. As mentioned in 3.3.1, the model consists in a controlled continuity spline influenced by image forces as well as external constrained forces. Given that the controlled continuity spline is a generalization of the Tikhonov stabilizer [43], Kass *et al.* suggested to treat it as a regularization problem [111]. Geometrically, snakes are contours embedded in an image plane $(x, y) \in \Re^2$. The position of a snake can be parametrically represented as $v(s) = (x(s), y(s))$, where x and y are the coordinate functions and $s \in [0, 1]$ is the domain. The energy functional of the contour is given by,

$$
\begin{aligned}
E^*_{snake} &= \int_0^1 E_{snake}(v(s))ds \\
&= \int_0^1 E_{int}(v(s)) + \int_0^1 E_{image}(v(s)) + \int_0^1 E_c(v(s))ds
\end{aligned}
\tag{3.5}
$$

where E_{int} is the internal energy (piecewise smoothness constraint), E_{image} represents the image forces, and E_c gives the external constrained forces (pushes snakes to desired local minima). Eq. 3.4 in section represents a simplified version of the same formulation. Deconstructing each component, the internal energy can be depicted as,

$$E_{int} = (\alpha(s)\,|V_s(s)|^2 + \beta(s)\,|V_{ss}(s)|^2)/2 \tag{3.6}$$

with the first and second order control terms, $\alpha(s)$ and $\beta(s)$ respectively, controlling the nature and behavior of the curve. Specifically, $\alpha(s)$ controls the tension, and $\beta(s)$ controls the rigidity in an image [103]. For discretizing the energy formulations Eq. 3.6 can be rewritten by using vector notation $V_i = (x_i, y_i) = (x(ih), y(ih))$ as,

$$E_{int} = \alpha_i\,|V_i - V_{i-1}|^2\,/2h^2 + \beta_i\,|V_{i-1} - 2V_i - V_{i+1}|^2\,/2h^4 \tag{3.7}$$

The corresponding Euler equations obtained can be represented in matrix format are,

$$\mathbf{Ax} + \mathbf{f_x(x,y)} = \mathbf{0}$$
$$\mathbf{Ay} + \mathbf{f_y(x,y)} = \mathbf{0}$$

Solving the equations in a matrix inversion, we obtain

$$\mathbf{x_t} = (\mathbf{A} + \gamma\mathbf{I})^{-1}(\gamma\mathbf{x}_{t-1} - \mathbf{f_x}(x_{t-1}, y_{t-1}))$$
$$\mathbf{y_t} = (\mathbf{A} + \gamma\mathbf{I})^{-1}(\gamma\mathbf{x}_{t-1} - \mathbf{f_x}(x_{t-1}, y_{t-1}))$$

where $\mathbf{A}$ and $\mathbf{A} + \gamma\mathbf{I}$ are pentadiagonal banded matrices, and t represents the time steps. The inverse matrix is calculated using LU (lower-upper) decomposition, being the computational complexity $O(n)$. Thus, simplifying the formulation the image energy can be expressed as a combination of weighted energy terms as in Eq. 3.2, given by

$$E_{image} = \; w_{line}\; E_{line} + w_{edge}\; E_{edge} + w_{term}\; E_{term} \tag{3.8}$$

The line functional is represented by image intensity $E_{line} = I(x, y)$, and the weight w_{line} is determined by the pixel intensity towards which it is attracted. The edge functional is given by the filtered image intensity gradient $E_{edge} = -(Filt * \nabla^2 I)^2$, where $Filt = G_\sigma$. We introduce the filtering term to avoid the spline from getting struck in a local minimum. Mandal *et. al.* [87] has shown the applicability of scale-space processing for OA images, and an anisotropic diffusion (Modified Perona-Malik diffusion) with Gaussian kernel can also be employed [69], it is expressed as

$$\frac{\partial I}{\partial t} = div(c(|DG_\sigma * I|)\nabla I) \tag{3.9}$$

where D is the diffusion tensor and c is the diffusion coefficient [116].
The terminal functional plays of role in finding terminations of line segments and corners and operates on a smoothened image $I' = (Filt * I)$. Assuming the gradient angle $\theta = \tan^{-1}(I'_y/I'_x)$, we can write the curvature of level contours in as

$$\begin{aligned} E_{term} &= \frac{\partial \theta}{\partial \mathbf{n}_\perp} \\ &= \frac{\partial^2 I' / \partial \mathbf{n}^2{}_\perp}{\partial I' / \partial \mathbf{n}} \\ &= \frac{I'_{yy} I'^2_x - 2 I'_{xy} I'_x I'_y + I'_{xx} I'^2_y}{\left(I'^2_x - I'^2_y\right)^{3/2}} \end{aligned} \tag{3.10}$$

where $\mathbf{n} = (\cos\theta, \sin\theta)$ and $\mathbf{n}_\perp = (-\sin\theta, \cos\theta)$ are the unit vectors along and perpendicular to the gradient direction [98, 117].
The basic snake model entails calibration of several parameters, has higher computational complexity, and cannot detect multiple objects in the same topology. However, it offers a better understanding of its interaction with MSOT images and perfectly suits the two compartment model of segmentation we are currently pursuing.

3.3.2 Experimental protocol

3.3.2.1 Tissue mimicking phantoms

Two types of tissue mimicking phantoms were developed for testing purposes. The first phantom was built to render a light fluence attenuation representative of average soft tissues. For this, black India ink and Intralipid were added to the agar solution in order to attain an optical absorption coefficient $\mu_a = 0.2\ \mathrm{cm}^{-1}$ and a reduced scattering coefficient $\mu\prime_s = 10\ \mathrm{cm}^{-1}$. Two tubular insertions of a more concentrated India ink having an optical absorption coefficient of $\mu_a = 1\mathrm{cm}^{-1}$ were embedded in the phantom at different depths, one tubing being located close to the periphery and the other approximately at the center of the phantom.
The second phantom was designed to mimic a small increment in the SoS. This was achieved with a mixture of agar solution (approximately 2/3 by volume) and glycerine (approximately 1/3 by volume), as described in [55, 110]. As glycerine is hydrophilic, it readily dissolves in the water-based agar solution. Given the fact that the SoS in glycerine is 1920 m/s and the SoS in agar gel is approximately 1500 m/s, the expected SoS in the mixture is around 1640 m/s, i.e., $\approx 10\%$ increase. Black polyethylene microparticles with a diameter of approximately $200\mu m$ (Cospheric LLC, Santa Barbara, CA) were then embedded in the imaging plane to assess the spatial resolution rendered. The phantoms were made in irregular shapes so that the efficiency of segmentation algorithm can be properly assessed. All phantoms were finally embedded in cylindrical blocks of agar with a diameter of 24 mm for easier handling.

3.3.2.2 Small animals imaging

The segmentation performance was evaluated with *in-vivo* mouse images. For this, the animal handling protocols were scrupulously followed under supervision of trained personnel and the imaging experiments were performed in full conformity with institutional guidelines and with approval from the Government of Upper Bavaria. The mice were sedated with Isoflurane and immersed in water bath kept at 34°C using a specialized mouse holder (iThera Medical GmbH, Munich, Germany). Altogether, 30 datasets were acquired from 12 different mice for three different representative anatomical regions, namely (a) brain, (b) liver and (c) kidney/spleen. In addition, two polyethylene tubings containing Indocyanine green (ICG) $\mu_a = 1.9$ cm^{-1} at $\lambda = 800$nm were inserted at different depths (peripheral T1 and deeply embedded T2) in a CD1 mouse post mortem in order to quantitatively validate the suggested SoS and light fluence correction methods in real tissues [92]. The mouse was then imaged at different positions along the torso using 10 different wavelengths ranging between 680 and 900 nm. From the multispectral data, the ICG distribution was spectrally unmixed from background tissue components using a semi-automated blind unmixing algorithm termed vertex component analysis [69].

3.3.3 Performance of segmentation methods

We imaged irregular shaped phantoms and small animals (*in vivo* and *post mortem*) as mentioned in 3.3.2 to establish the efficacy of the the active contour segmentation methods for OA imaging. The segmentation results for the irregular phantoms (star and heart) are shown in Fig. 3.4. For the phantom experiments the segmentation accuracy achieved was very high (DM ≈ 9.4), and additional morphological processing for getting a smoother boundary was not required. However, we observed slight aberration at the surfaces of phantoms prepared with material having two significantly different SoS - such issues can be addressed by application of multiple SoS mapping algorithms as outlined in section 3.4.2. The DM values are computed using the a-priori shape and size information of the imaged object, and comparing the same with the segmentation mask.

The applicability of active contour segmentation for *in-vivo* small animal datasets reconstructed with the model-based reconstruction method is showcased in Fig. 3.5. The optimum values of the terms in Eq.3.4 for *in-vivo* mouse imaging were heuristically determined by computing the segmentation with different values and assessing the segmentation performances over multiple datasets acquired from the brain, liver and kidney/spleen regions. These regions have image properties and morphologies that are very distinct from each other, thus the properties of the snakes were recalibrated for each region individually. We used 10 datasets for each of the regions and used their averaged values to determine the mean parameters, as listed in Table. 3.2. Filter Coef. denotes the values used for Gaussian kernel before initiation of the snakes. Iter denotes the number of iterations applied for each region. W represents the values for energy functions as employed for the line, edge and term measures respectively. DM gives the value for Dice coefficients, which is a measure of segmentation accuracy.

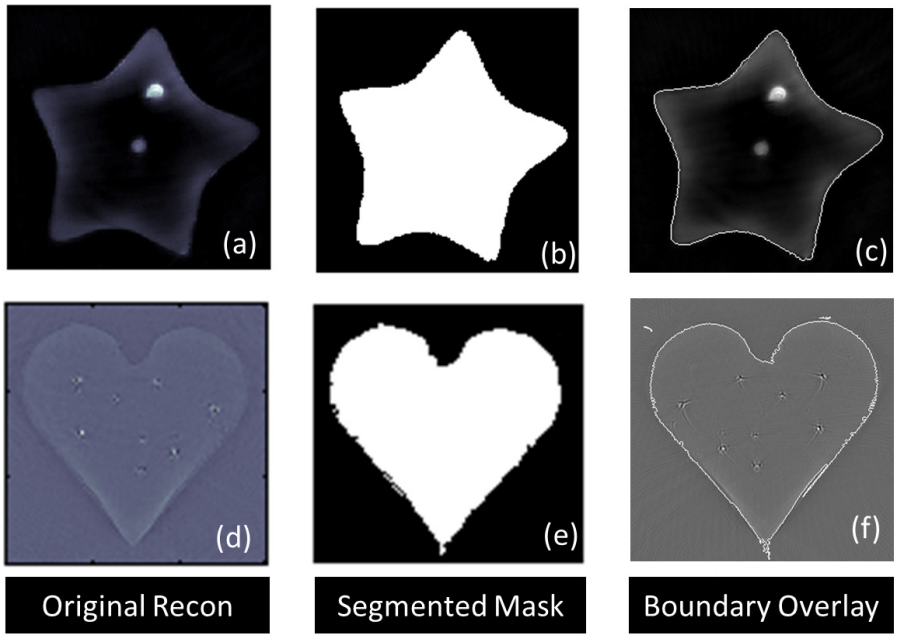

Figure 3.4: Active contour segmentation performance using irregular phantoms: Tissue mimicking Star (agar) phantom (a) and heart (agar + glycerin) phantoms (b), the corresponding segmented masks (b and e), and the corresponding boundary overlaid images (c and f).

Table 3.2: Active contour segmentation parameters for *in vivo* imaging

Regions	Filter Coef	# Iter	W_{LINE}	W_{EDGE}	W_{TERM}	DM
Brain	0.5	550	0.5 ± 0.1	0.6 ± 0.2	0.7	0.944
Liver	1.0	250	0.3 ± 0.1	0.5 ± 0.05	0.7	0.957
Kidney/Spleen	0.7	280	0.3 ± 0.1	0.5 ± 0.1	0.7	0.953

Further, the segmentation performance was tested using both heuristically chosen initial starting contour points as well as by using geometrical shape priors for initiating the contour evolution automatically. The experimental results also revealed that the minimum number of contour points that need to be defined for curve initiation is 9, so that this configuration has been used through the rest of the test samples. For better segmentation performance, a Gaussian filtering was further applied to the original images before initiation of the curve evolution. The filter coefficients used for different *in-vivo* datasets are shown in Table 3.2. The results show high variability of the parameter sets in the brain region, which demand more iteration steps (slower convergence) and yields lower segmentation accuracy. The Dice metric was then used for characterizing the segmentation accuracy vis-à-vis with user feedback. DM provides us with a statistical measure for comparing similarity of two samples, and its cut-off limits for good segmen-

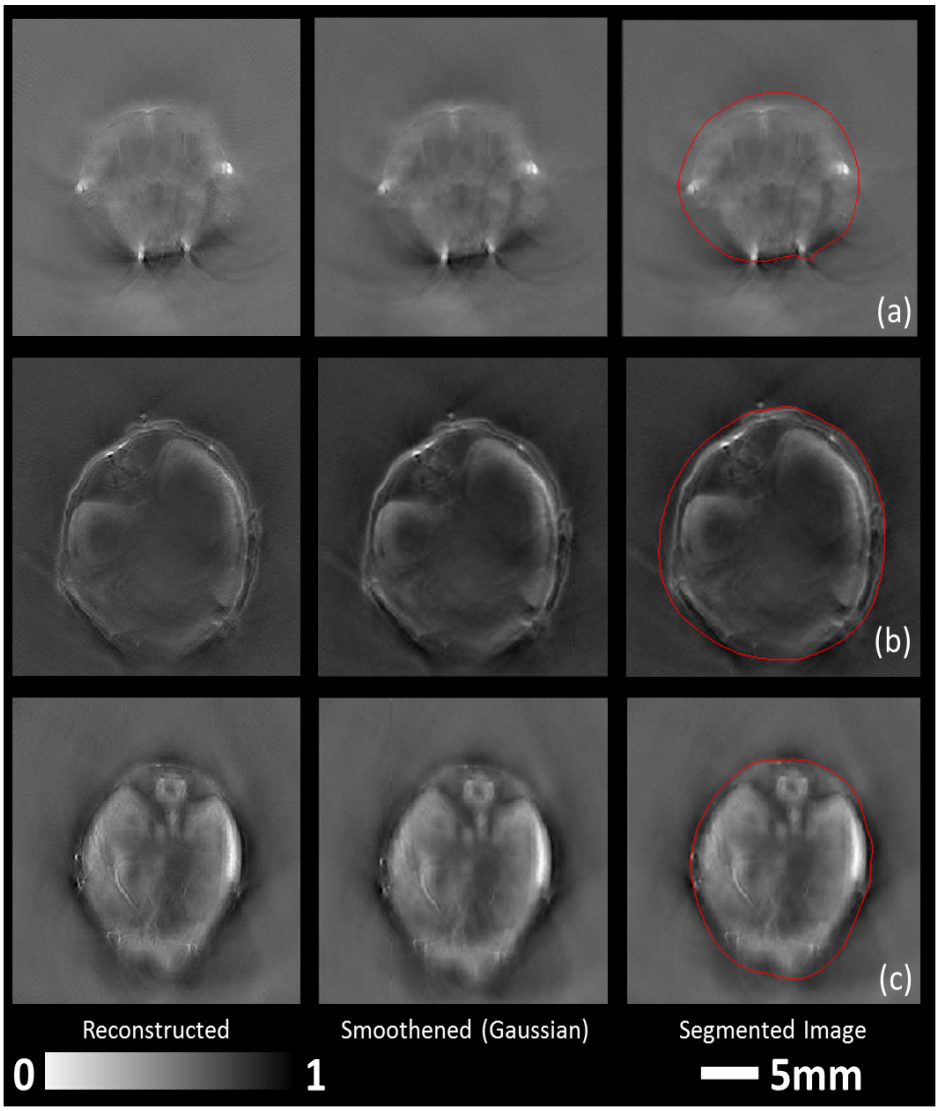

Figure 3.5: Tomographic OA reconstructions of the brain (a), liver (b) and kidney/spleen (c) regions of mice *in-vivo*. The original reconstructed images obtained with model-based inversion are shown in the first column. The second column displays the smoothened images after gaussian filtering. The segmented images using active contour(snakes) with the optimum parameters are showcased in the third column

tation are empirically decided by studying the ecologic association between species in nature [118] . For this, four independent volunteers performed manual segmentation of the reconstructed images. The current results yielded a DM$\geq$ 0.9, whereas DM$>$ 0.7 is generally considered as good segmentation. In this way, a satisfactory performance of active contour models for MSOT image segmentation was confirmed.

3.4 Visual quality enhancement using segmented priors

3.4.1 Fluence correction

In MSOT, the reconstructed images for each wavelength represent a map of the spatially varying optical energy being absorbed by the tissue. Assuming a uniform Grueneisen parameter in soft biological tissues, the absorbed energy is proportional to the product of the absorption coefficient $\mu_a(\overrightarrow{r})$ and the light intensity $U(\overrightarrow{r})$ at a given voxel. Obtaining accurate maps of concentration of individual chromophores implies on the one hand spectrally or temporally unmixing the distribution of the chromophore of interest from other substances contributing to $\mu_a(\overrightarrow{r})$, and on the other hand normalizing the OA images with the excitation light fluence distribution. Several mathematical procedures have been suggested for light fluence normalization [18], including optical propagation models [119], iterative algorithms based on fixed-point methods [120, 121], frequency decomposition of OA images, logarithmic unmixing of multispectral datasets [122], or estimation of decay rates of photoswitchable probes [123]. Light fluence can be directly estimated from the OA images [100], but the image need to be properly segmented to accurately assign the optical properties to different tissues. Here, we propose a diffusion-theory-based light propagation model that uses the segmented boundaries of the object as a method to extract quantified information from OA images. The photon diffusion equation [124, 90] is assumed to model the light intensity in scattering tissues,

$$S_0 = -\nabla.[D(\overrightarrow{r}).\nabla U(\overrightarrow{r})] + \mu_a(\overrightarrow{r})U(\overrightarrow{r}) \tag{3.11}$$

where $D = {}^1\!/_3(\mu\prime_s + \mu_a)$ is the spatially dependent diffusion coefficient of the medium and $\mu\prime_s$ is the reduced scattering coefficient, S_0 being the source term. neglects transient effects, which applies for typical pulse durations of 10 ns (or equivalently 3 m length) used for OA excitation. We assumed a constant intensity illumination (S_0) on the boundary enclosing the object volume, and the problem was treated as a two-dimensional problem for simplicity. The interface between the scattering and non scattering medium can be modeled using the Robin boundary condition [125],

$$U(\overrightarrow{r}) + 2D(\overrightarrow{r})\hat{n}.\overrightarrow{\nabla}U(\overrightarrow{r}) = 0, \overrightarrow{r} \in \partial\Omega \tag{3.12}$$

where $\partial\Omega$ the boundary of the object and is the unit vector normal to the boundary pointing outwards. The solution to Eq.3.12 is obtained numerically using a finite volume method (FVM) solution approach based on the Deal II Framework [100, 126]. In the given framework the elements of the mesh have a cubical base shape which is deformed and stretched to match the shape of the imaged object. The value of the fluence is

thereafter calculated for the nodes and interpolated over the elements using a pre-defined interpolation function to reduce the computational complexity. As opposed to the earlier approaches that employed a geometrical approximation of the thresholded image to generate the FVM mesh and mapping the nodes [126], we herein used the precisely segmented boundary to provide a more accurate basis for generating the mesh.

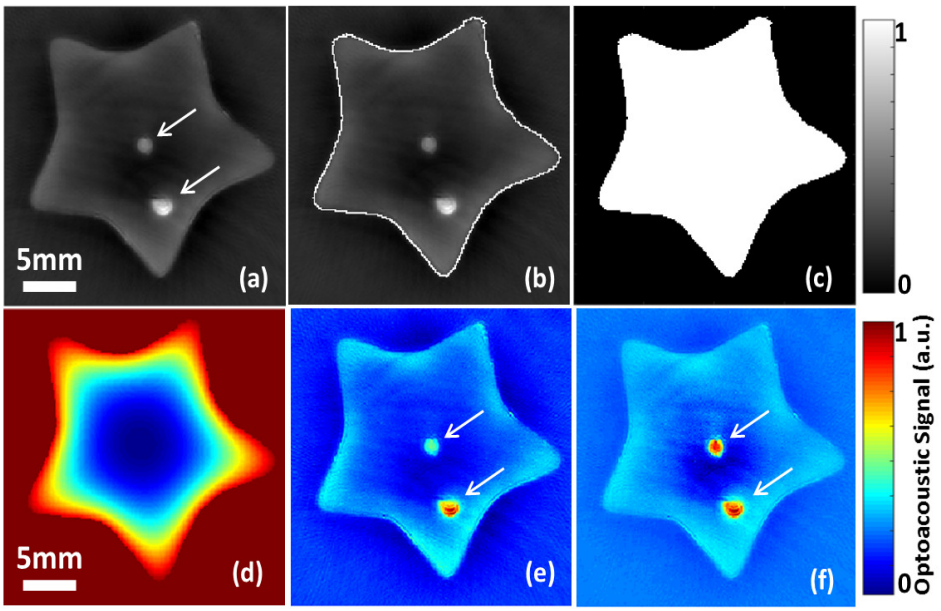

Figure 3.6: Model-based reconstruction without optical fluence correction shows an erroneous fluence distribution (a). The reconstructed image is segmented using active contour method (b) and the binary segmentation mask is extracted (c). The fluence model (d) is generated using the mask (b) as prior by application of the FVM method. Two tubular insertions of India ink having equal OD but placed at different distances from the light sources in a turbid medium are imaged (marked by white arrows), the fluence corrected image (f) using the proposed method shows better visual saliency compared to uncorrected image (e).

The results of the segmentation-assisted optical fluence normalization are illustrated in Fig.3.6. First, the OA image of the tissue mimicking phantoms with two identical tubular insertions was obtained using the model-based method, as shown in Fig.3.6(a). It can be readily seen that the two insertions (marked with white arrows) appear with substantially different intensities in the image. Indeed, optical attenuation - contributed by absorption and scattering – in the tissue mimicking phantom leads to a lower signal intensity generated for deeper-seated objects. Active contours were then used to segment the boundary of the sample, as shown in Fig.3.6(b). Based on the segmented mask in Fig.3.6(c), the light fluence distribution was obtained with a FVM based simulation assuming uniform light distribution on the boundary of the object and uniform optical properties (Fig. 3.6(d)). Normalization of the OA image with the estimated light fluence field yields the image displayed in Fig.3.6(f) (Fig.3.6(e) is the reference image without normalization), in which the two embedded tubings show similar signal intensity

as would be expected from absorbers comprising the same concentration of the chromophores. The results of the post-mortem imaging studies are displayed in Fig.3.7. The figure shows an example of a cross-sectional image being corrected for the light fluence attenuation effects. The ICG tubings and the average tissues were spectrally unmixed into two components and superimposed with different colormaps after applying the fluence correction for better visualization. It clearly shows that the relative signal intensity increases for the deep-seated tubing (T2) after light fluence normalization (Fig.3.7(b)) as compared to the non-normalized image (Fig.3.7(a)). To quantitatively evaluate the performance of the method, two-dimensional regions of interest surrounding the tubing locations were considered and the relative intensity values were compared before and after light fluence normalization for the different cross-sections (Fig.3.7(d)). Uniform optical properties were assumed within the sample according to reported average values for biological tissues [91]. The absorption coefficient was taken as $\mu_a = 0.29$ cm^{-1}, while the light fluence distribution was estimated for two different values of the reduced scattering coefficient, namely $\mu\prime_s = 15cm_{-1}$ and $\mu\prime_s = 20$ cm^{-1} [17, 127]. In both cases, the calculated intensity ratios were close to 1 for the normalized cross-sections, which demonstrates that the proposed method can offer good performance with segmented image priors. Thus, inspite of considering a simplified model for representing heterogeneous tissues, an improvement in the quantitative performance of MSOT is achieved.

3.4.2 Mapping multiple speeds of sound

In a typical MSOT imaging domain, the coupling medium and the imaged object often have different SoS, which may impair the image reconstruction quality [87, 55]. Different approaches have been so far developed to alleviate this problem, e.g. by means of the SoS mapping or generalized Radon transform models assuming geometrical acoustics approximations. Accordingly, here we use the segmented image mask to fit multiple SoS values to the different regions in the image, thus providing an alternative method to address the issue of acoustic heterogeneities without increasing the mathematical or hardware complexity of the imaging problem. To evaluate the performance of the proposed methodology, a two compartment model is considered consisting of the coupling medium outside the imaged object (the background) assigned with a given SoS (C_b) and the region inside the imaged sample assigned with a different SoS (C_o). In this formulation, the method is applicable to any reconstruction algorithm capable of accounting for a known distribution of the SoS, e.g. the filtered back-projection (FBP) algorithm [34], the interpolated matrix inversion method [15] or the time-reversal approach [116]. Herein, the FBP algorithm was used to automate the workflow in conjunction with automated SoS calibration. The automated SoS calibration for the image fitted with two values of the SoS was carried out with a normalized variance of the image gradient magnitude using Sobel operator (Sobel+Var) and anisotropic diffusion using consistent gradient operator (Ad-CG), as recently reported by Mandal *et. al.* [87, 69]. The FBP method is based on a delay-and-sum approach and for a finite number of measuring locations, where the optical energy deposition at a given pixel of the region of interest (ROI) is calculated as,

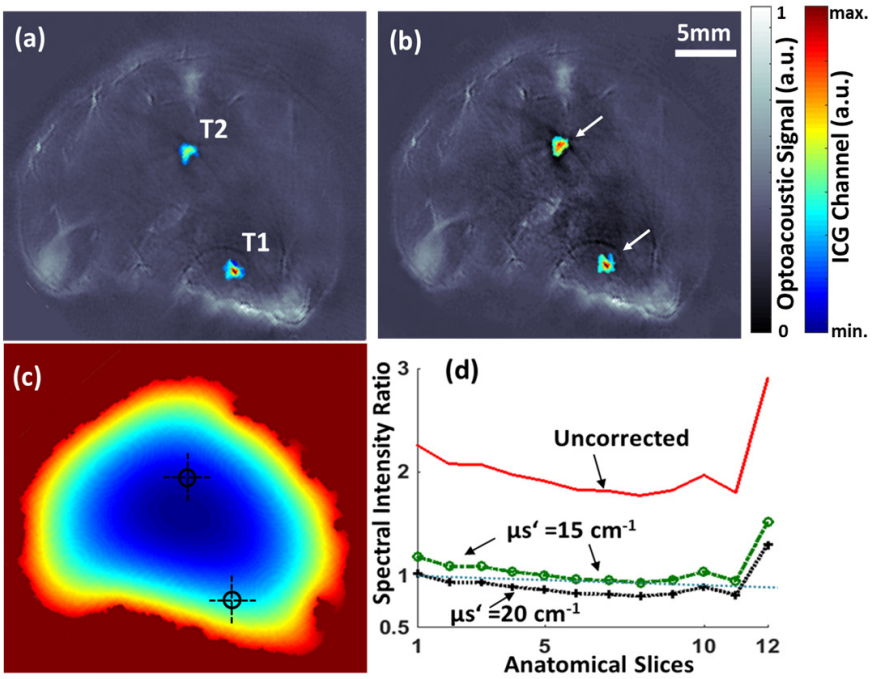

Figure 3.7: Post-mortem imaging of mice with ICG insertions $\mu_a = 1.9cm^{-1}$ at $\lambda = 800$nm at two different depths (T1 and T2): The optoacoustic anatomical reference image and the unmixed images corresponding to the ICG distributions for the uncorrected image (a) and fluence corrected image (b) are displayed. Both images were obtained post unmixing using 10 different wavelengths. The fluence map generated using the FVM method using the segmented prior is shown in (c), crosshairs indicates positions of insertions. The relative contrast ratios for fluence uncorrected and corrected images (12 anatomical slices) for two different tissue absorption properties are plotted in (d), clearly demonstrating a significant improvement (1.1691) after application of fluence correction using the proposed segmented prior based FVM method.

$$f(x'_j, y'_j) = \sum\nolimits_i s(x_i, y_i, t_{ij}) \tag{3.13}$$

where (x_i, y_i) is the i^{th} measuring location and $t_{ij} = \mid (x'_j, y'_j) - (x_i, y_i) \mid /c$, being c the SoS when a uniform SoS is considered. $s(x_i, y_i, t_{ij})$ represents the function to be back-projected, i.e. filtered pressure. Eq. 3.13 is expressed in arbitrary units, where the constant terms accounting for unit conversion factors are omitted for simplicity. As mentioned earlier, we fit two SoS values (c_o, c_b) for the background and object respectively. In this case,in Eq. 3.13 is estimated as the time of flight (ToF) from the center of the transducer to a given voxel is calculated as

$$ToF = \frac{d_c}{c_0} + (d - d_c)/c_b \tag{3.14}$$

where d is the distance from the detector to the voxel considered and d_c is the fraction of d located within the tissue. We can employ the model-based algorithm for multiple

SoS mapping, however the method is computationally expensive for SoS calibration purposes. Thus, we choose FBP methods for automated SoS calibration and multiple SoS fitting. The details of the SoS calibration methods and the rational for favoring the faster (but often less accurate) FBP method has been illustrated by [87].The phantom results are presented in Fig. 3.5. Fig.3.5(a) shows the tomographic reconstruction obtained when a uniform value of the SoS is assumed for both the phantom and the surrounding coupling medium. A single value of the SoS ($c = 1535m/s$) was fitted based on focusing metrics, which visually yields a reasonable reconstruction. However, a closer observation reveals that the difference of SoS between background and phantom has inevitably led to degradation of image quality. Specifically, a zoom in on a selected microsphere reveals that some microspheres in the imaged plane have not been accurately reconstructed due to acoustic mismatch and wrong assignment of the SoS distribution. Additional artifacts appear at the edge of the phantom, as indicated by the white arrow. Active contour segmentation (and morphological processing as explained in) was subsequently applied to the tomographic reconstruction in Fig. 3.5(a), yielding the mask displayed in Fig. 3.5(b). The mask allows differentiating between the imaged object and the background region, so that different values of the SoS can be assigned. In particular, the values of the SoS for the sample ($c_o = 1565m/s$) and the background ($c_b = 1515m/s$) were estimated based on autofocusing metrics. The corrected tomographic reconstruction obtained by considering the mask in Fig. 3.5(b) and the fitted values of the SoS is showcased in Fig. 3.5(c). The magnification of the same area as in Fig. 3.5(c) shows a sharper reconstruction of the microsphere when compared to Fig. 3.5(a). Furthermore, the model using multiple SoS renders a sharper appearance of the edges (marked with a white arrow).

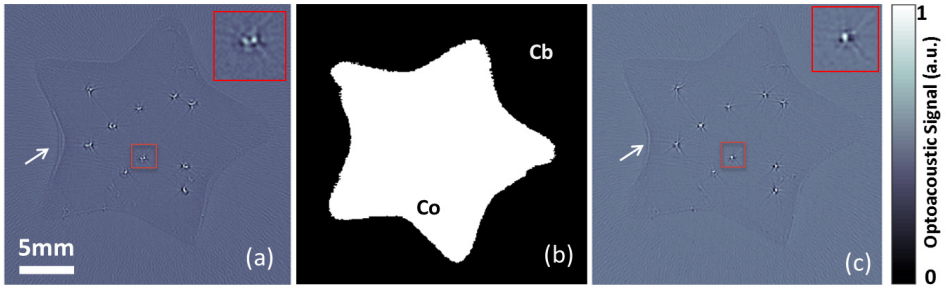

Figure 3.8: Single speed of sound (SoS = 1535) is applied homogenously to obtain (a), the segmentation mask (b) is extracted using active contour method and morphological processing. Two different SoS -1525 (Cb) for background region and 1565 for inside object boundary (Co) were fitted to obtained an improved reconstruction (c). Zoom in (region marked with red boxes) of reconstructed microsphere(s) is included in insert and reconstructed edges are marked with arrow (s).

The post-mortem acquisitions were used for evaluating the algorithm performance in the case of low contrast ex-vivo images that may yield less accurate segmentation using active contours (Fig. 3.9). Here we first reconstructed an image using the backprojection

algorithm, whereas focusing matrices with temperature priors were used to determine the most suitable SoS. An initial segmented mask was then obtained by segmenting the reconstructed image, which was morphologically processed to provide a smoother mask. Finally, the obtained mask was employed to build the two-compartment model of SoS. The SoS of the background coupling medium (water bath) was determined using its measured temperature (c_o=1515m/s at 34°C). For computing the SoS of the object, we reconstructed a stack of 100 images with SoS spaced 5 m/s and a fixed background SoS. Selected autofocusing metrics were executed to determine the calibrated SoS ($c_o = 1555$ m/s). The reconstructed image obtained with the two compartment model is shown in Fig 3.9(b). The autofocusing metrics showed good convergence in the presence of strong absorbers in Fig. 3.9(d), and the line profiles displayed in Fig 3.9(c) indicate significant improvements with respect to images reconstructed with a uniform SoS. Indeed, not only are the tubings better characterized but also the internal structures are observed to be marginally more defined, e.g. spinal region, when using the two compartment SoS approach. Similar to the light fluence normalization measurements, segmentation of internal areas having different values of the SoS may further improve the resolution and contrast of the reconstructed images obtained by accounting for heterogeneous acoustic properties of tissues.

3.5 Discussion and conclusion

In this chapter, we have outlined two independent methods for segmenting OA images and demonstrated the applicability of the segmented priors to improve visual image quality in quantitative OA imaging. The first method (as outlined in section 3.2) that has been demonstrated for delineating the boundary of OA small animals images uses a multiscale edge detection algorithm in combination with geometrical curve fitting. The method is self-deterministic and requires minimal human intervention. The second method (section 3.3.1), employs active contour (snakes) models for segmentation in cross-sectional (two-dimensional) tomographic OA imaging. Further, the we have shown that using the active contour segmentation results as prior information during the image reconstruction procedure can significantly improve the imaging performance.The performance of active contour models has been outlined for whole-body segmentation of mice using three representative anatomical regions.The optimum values of the parameters used in the segmentation procedure such as the weighting factors to estimate the image forces or the number and location of the initial contour points were determined heuristically. Specifically, these values were computed over multiple datasets and the segmentation performance was subsequently evaluated. Thereby, these parameters may need to be recalibrated for other tomographic configurations or other biological samples. Further, it is possible to develop strategies to automate the seed point detection through the use of parametric curve fitting models, given a computational overhead [127]. The fitting models can further reduce dependency on human feedback, but do not influence the final segmentation performance.
Acoustic inversion in OA tomography is commonly conditioned by the differences be-

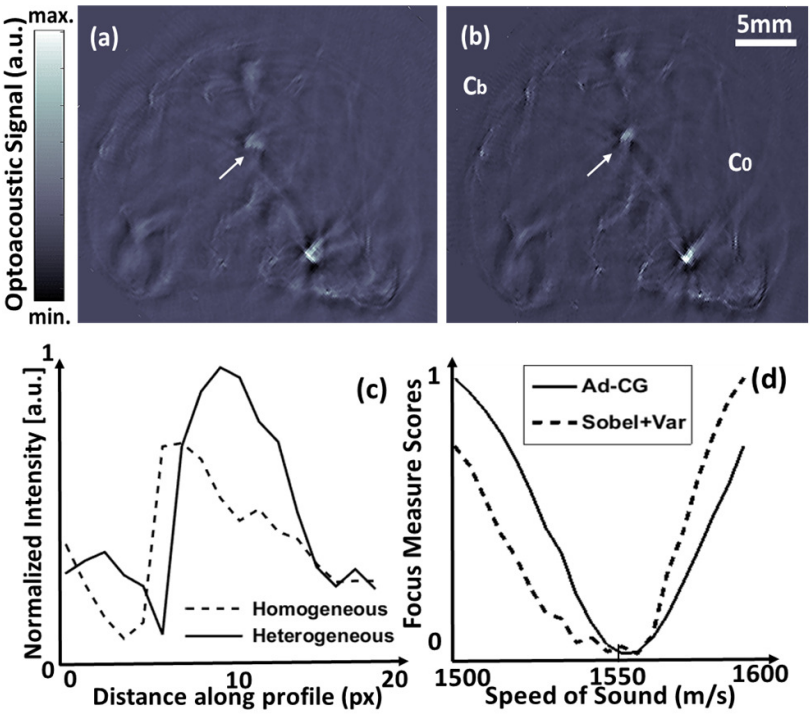

Figure 3.9: Post-mortem images of mice with ICG insertions (200 nmol) at two different depths reconstructed with (a) single speed of sound (1520) and (b) multiple (differential) speeds of sound (Background SoS Cb = 1515 and Object SoS Co = 1555 m/s). The line profiles of the marked insertion along the direction of the arrow when reconstructed with homogenous and heterogenneous SoS are shown in figure (c). The automated speed of sound calibration curves (Sobel +Var and Ad-CG methods) for heterogenous SoS fitting are shown in (d).

tween the acoustic propagation properties of the imaged tissue versus the surrounding coupling medium. Typically, a uniform non-attenuating medium comprising both the sample and water is assumed for reconstructions, which may lead to an inadequate imaging performance since the average acoustic properties in soft biological tissues are generally different from water. Thereby, identifying regions with different SoS or acoustic attenuation or areas with strong acoustic scattering or reflections is essential for optimizing the reconstruction performance. A two compartment model assuming an acoustically homogeneous tissue can then be used as a second order approximation to improve accuracy of the tomographic reconstructions. We have shown that by considering a different SoS in the sample, one can improve the spatial resolution performance when imaging through real heterogeneous tissues. Clearly, a similar procedure can be used to segment the imaged medium into three or more compartments in order to further enhance the imaging performance. In a similar manner, optical propagation is very different in a transparent coupling medium as compared to real biological tissues, where photons undergo strong absorption and scattering. Thereby, a two compartment model can also be used as a first order approximation to account for the significant effect of

light fluence attenuation, and segmentation of the OA images is then again essential for this purpose. Normalization with the light fluence distribution is needed for quantifying the concentration of specific optical biomarkers. We have shown that a numerical model assuming homogenous optical properties within properly segmented boundary can already be sufficiently accurate for normalization purposes both in phantom experiments with controlled absorption and scattering, as well as in real biological samples. A more accurate estimation of the light fluence within the sample implies detailed knowledge of the spatial distribution of its optical properties, which is very challenging to obtain in living organisms. It was previously shown that iterative light normalization methods may render good performance in numerical simulations [18, 128] but can turn unstable in experimental studies if the scattering coefficient or object boundaries are not accurately estimated. Proper segmentation of the outer boundary of the sample or internal regions having strong changes in optical properties then becomes essential for accurate light fluence normalization in OA tomography [93].
The OA signal/image datasets can be very large given the 5D nature of this modality, automating the image formation and analysis workflow is a very challenging and important problem. Thus, the algorithms and the workflows demonstrated herein are expected to be helpful in automating OA image segmentation, with important significance towards enabling quantitative imaging applications. In conclusion, OA image segmentation and analysis is a nascent and emergent area of investigation that holds potential for advanced applications including, but not limited to organ segmentation, diagnostic imaging [129] and pharmacokinetic studies [130]. The demonstrated good performance of active contour models for OA segmentation of real tissues, and the feasibility to account for optical and acoustic discontinuities in the imaged region, anticipate the general applicability of the suggested approach for enhancing the resolution and image quality of tomographic OA reconstructions. Considering that the recently developed hand-held probes for OA clinical translation employ the same acquisition geometry, the methods presented in this work can further be applied in the development of diagnostic tools for translational imaging in human subjects [131].

4 Enhancing image resolution using pixel super-resolution

The spatial resolution of optoacoustic (OA) imaging is limited by the properties of the ultrasound transducer(s) used to collect the signals as well as by acoustic propagation parameters [86]. The final resolution recovered from an OA acquisition is determined by the system configuration and the reconstruction algorithm employed [132, 133]. The ideal reconstruction procedure is usually based on several assumptions: (1) wide-band detection, (2) point detector measurement, (3) impulse excitation, (4) homogeneous speed of sound, (5) full-angle detection view and (6) continuous sampling. However, most of these assumptions are not realistic in practical implementations. For example, actual ultrasound sensors have a finite sensing aperture and detection bandwidth [10], which limit the frequency content of the detected signals and hence the spatial resolution achieved [134]. Phase aberrations caused by speed of sound (SoS) variations and signal broadening associated to acoustic attenuation [135, 136] also degrade the spatial resolution of the images rendered by assuming a uniform acoustic medium [87, 55]. Finally, the detection surfaces are generally finite and partially closed, so that the OA signals cannot be collected from all directions [137, 138]. Under these circumstances, the achievable spatial resolution is usually lower than that predicted theoretically.

Traditionally the researchers have attained improvements in spatial resolution and overall image fidelity through hardware improvements by means of increasing the detector density [139]. Reconstruction methods that account for the detection properties of the measurement system and signal distortions (in the coupling medium) has further enhanced the imaging performance [86, 135, 52, 45, 140]. Accurate modeling in actual biological tissues can solve the mentioned issues, however, it is a non-trivial challenge and advanced algorithms are computationally expensive [138, 56].

An alternative approach to improve the contrast and spatial resolution of an image is by integrating information from several low resolution (LR) images obtained at different imaging positions to generate a high resolution (HR) image [141, 142]. Termed super-resolution [143, 144], this imaging method relates to a class of 'pixel super resolution' algorithms that are employed in digital imaging and lens-less microscopy, to overcome resolution limitations due to pixel size. This approach does not relate to super-resolution methods aiming at breaking the diffraction limit of light and/or ultrasound [145, 146]. To differentiate these two classes of "super resolution" methods we refer to the method

This chapter has been adapted with modifications from:
H. He, **S. Mandal**, A. Buehler, X. L. Deán-Ben, D. Razansky and V. Ntziachristos, "Improving Optoacoustic Image Quality via Geometric Pixel Super-Resolution Approach," in IEEE Transactions on Medical Imaging, vol. 35, no. 3, pp. 812-818, March 2016.

employed in digital imaging as pixel super resolution (PSR) herein. PSR methods were first introduced in digital image processing [143] and have been adapted to biomedical imaging modalities such as x-ray CT, MRI and PET [144, 147, 148, 149, 150, 151, 152]. PSR methods have been successfully applied to MRI for resolution and image quality enhancement without increasing the acquisition time or changing the imaging system [149]. For example, Kennedy et al. [144] demonstrated the application of iterative PSR algorithms in improving resolution of clinical PET imaging by multiple datasets with spatial shifts between consecutive acquisitions. The PSR method suggested herein is specifically implemented the scanning protocols of a small animal MSOT scanner, and is termed OA-PSR [2].

In this chapter, we outline the basic theory behind PSR algorithm, demonstrate the PSR implementation in OA imaging and illustrate the improvements gained in image resolution and contrast. The study includes simulations and experimental measurements on phantoms and ex-vivo murine organs.

4.1 Theory of pixel super-resolution

The PSR method is a promising signal processing methodology, and has been an active area of research in computer vision and image enhancement. The recent award of the Nobel Prize in Chemistry (2014) [153], has sparked additional interest in the domain area of SR imaging, however our method does not address the limitations of (optical) diffraction limit, nor uses any photo-switchable agents to attain higher resolution. The PSR method focuses on image enhancement and overcomes the inherent resolution limits of LR imaging systems [147, 154]. The operating principle of PSR techniques relies on composing a high resolution image from a sequence of low resolution images acquired from different imaging perspectives or views [155]. During the image acquisition process motion is introduced by controlled phenomenon (e.g. rotation of satellites, panning camera motion) or unconditionally (e.g. object motion, breathing motion for animal imaging) [156, 157]. If we have a-priori information or are able to identify the motion(s) with subpixel accuracy, we can combine several LR images with slightly varied information to reconstruct a SR image, the method is illustrated in Fig. 4.1. The PSR methodologies comes with their own share of limitations and problems, the primary ones being the blurring of images (low egde information) and sub-sampled images. However, for OA implementations such problems are already dealt with using the algorithms for SoS autofocusing (2.2.1) or multi-bandwidth deconvolution [158], and improved image reconstruction (2.3). Interpolation is another problem in SR reconstruction, and inspite of improvements in interpolation techniques the single image interpolation functions cannot recover the losses in high frequency components and degradation causes during LR acquisition. Thus, many researchers do not consider interpolation as a SR technique. On the contrary SR imaging fuse information from multiple acquisitions/ datasets to achieve a HR image, and out implementation of OA- PSR is based on the same assumptions.

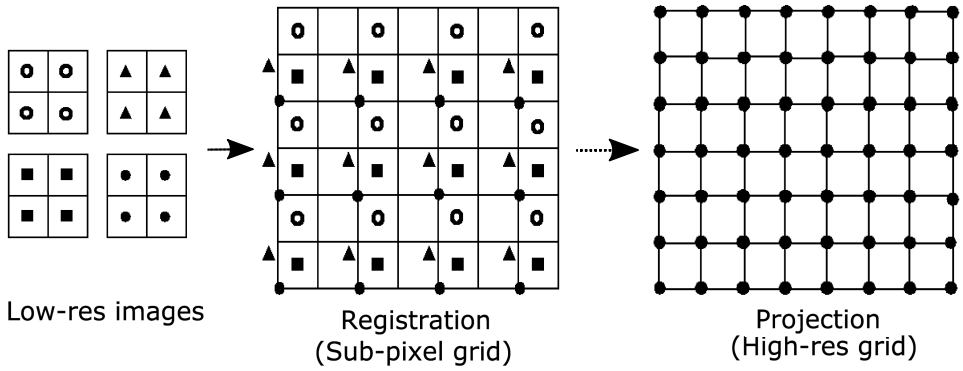

Figure 4.1: The basic premise for pixel super-resolution using a basic registration- regularization- projection based reconstruction. The method maps several LR images onto a HR grid.

4.1.0.1 Observational model

Formulation is a observational model that relates original HR image with the acquired LR image is vital to implement and analyze the PSR process. The image acquisition process is ideally modeled by the following stages: (*i*) geometric transformation, (*ii*) blurring (*iii*) down sampling and (*iv*) noise model. The models are well developed for camera imaging (a scenario where PSR is amply used), however, this being the first attempt to introduce PSR in OA we had to carefully design each component of the observational model. Further, the model for OA is one which takes consideration both the reconstruction and post-reconstruction image parameters, making it more complex than only the post-acquisition image parameters as in the case of camera (natural) images.
In the designed model the transformations included rotation and translations(in plane translations in multiple directions), blurring was introduced by convolving with the impulse response of the transducer arrays. The assumed noise model was additive Gaussian in nature. Given the considerations the observational model can be mathematically expressed as,

$$Y_k = D_k H_k F_k X + V_k \tag{4.1}$$

where Y_k represent the kth LR image with a native resolution of $N_1 \times N_2$, X is the HR image estimated from Y_k with a resolution of $qN_1 \times qN_2$, q being the scaling factor. D_k is the decimation operation, H_k is the blurring factor represents by the transducer impulse response, F_k is the affine motion operator between X and corresponding LR frame Y, and V_k is the additive Gaussian noise.

4.1.0.2 PSR image reconstruction algorithm

The PSR method is generally defined as an inverse process of imaging degradation, and we find several methods in literature to achieve it [158]. There are several ways through

which researchers have accomplished PSR reconstruction, the most commonly used methods used includes non-uniform interpolation approach, iterative back-projection, adaptive filtering approach, frequency domain approach, regularized reconstruction (deterministic and stochastic) approach, projection onto convex sets (POCS), and hybrid (maximum-likelihood minimization together with POCS) approaches [159, 160, 161]. For the current work, we employed the PSR regularized reconstruction approach, where the inversion is regularized due to the ill-posed nature of the problem [152, 162]. Accordingly, the HR image is calculated by imposing an additional regularization factor $\lambda\gamma(X)$ on the observational model (Eq. 4.1). Thus, the problem is reduced to a generalized minimization cost function derived from the observation model and can be expressed as,

$$\overline{X} = \arg\underset{X}{Min}\left\{\sum_{k=1}^{N} \|Y_k, D_k H_k F_k X\| + \lambda\gamma(X)\right\} \tag{4.2}$$

where $\gamma(X)$ is a regularization term, λ being a regularization weighting parameter determined according to the trade-off between edge information and noise. The initial guess for the HR image is taken by interpolating a specific LR image.

Though the spatial transformation for different acquisitions can generally be accurately characterized, the image transformation among reconstructed LR images may not exactly correspond to the defined spatial transformation due to inevitable movement of the imaging setup and target. Thereby, in order to improve the image quality in the PSR process, the image transformation between the estimated HR frame X and the kth LR frame Y (motion matrix F_k) is accurately estimated with a method based on optical flow registration [163]. Then, the solution of Eq. 4.2 corresponding to the HR image X is calculated iteratively until the solution converges or a pre-defined cut-off value (maximum) of iterations is reached.

The PSR inversion process defined in (Eq.4.2) is an ill-posed process, so that a regularization term is generally required for rendering a stable solution [162]. The regularization term compensates for ill-posedness by a priori imposing additional information on the desirable HR image [147, 162], consequently suppressing artifacts and noise, and improving the rate of convergence. Herein, we employ a bilateral total variation (BTV) regularization term defined as:

$$\gamma(X) = \sum_{l=-P}^{P}\sum_{m=0}^{P} \alpha^{|m|+|l|} \left\|X - S_x^l S_y^m X\right\| \tag{4.3}$$

where $l + m \geq 0$, S_x^l and S_y^m are shift matrices to present l and m pixels shift in horizontal and vertical directions, respectively. $P(1 \leq P \leq 3)$ is the shifting range in both directions and $\alpha(0 < \alpha < 1)$ is the weighting coefficient. The scalar weight α gives a spatially-decaying effect to the regularization terms summation. The BTV regularization is based on the combination of the total variation restoration model and the bilateral filter [147, 162], where total variation anisotropic diffusion [69] is used for image restoration and edge enhancement, and the bilateral filter focuses on noise reduction and edge sharpening [164]. Subsequent application of the bilateral filter several

times leads to smoothing of the signal until reaching a steady rate. Based on this, a large value of α is chosen for images affected by noise, which suppresses noise and smooth flat regions in the estimated HR image at the expense of losing edge information. More detailed information about the BTV regularization function can be found in [162, 164]. Combining eqns.4.2 and 4.3, the iterative PSR process is calculated with steepest descent method and the final minimization function described as:

$$\overline{X}_{n+1} = \overline{X}_n + \left\{ \sum_{k=1}^{N} F_k^T H_k^T D_k^Y \bullet sign(Y_k - D_k H_k F_k \overline{X}_n) + \lambda \left(\sum_{l=-P}^{P} \sum_{m=0}^{P} \alpha^{|m|+|l|} \left(I - S_x^{-l} S_y^{-m} \right) \bullet sign\left(\overline{X}_n - S_x^l S_y^m \overline{X}_n \right) \right) \right\} \tag{3.4}$$

where S_x^{-l} and S_y^{-m} represent the transposes of matrices S_x^l and S_y^m respectively and they have a shifting effect in the opposite directions as S_x^l and S_y^m.

4.2 Simulations studies for OA-PSR

4.2.1 Simulation design

Numerical simulations were performed to test the performance of the suggested PSR method on synthetic OA data. For this, a resolution target phantom was used to define the theoretical initial OA pressure distribution (Fig. 4.2(a)). The simulations were executed using MATLAB (MathWorks, Inc.) k-Wave Toolbox [17, 45]. The signals at 200 points located at a distance of 25 mm from the center of the phantom and equally-spaced along an arc of 180° were considered. A simulated Gaussian shape impulse response with a full-width at half maximum (FWHM) of 100 ns was convolved with the simulated OA signals to mimic the effects of the frequency response of the transducer, which degraded the spatial resolution to $150 \times 150 \mu m$. The phantom was shifted linearly with a step-size of 300 μm assuming that four LR images are to be acquired in four translation scanning positions, i.e. $(x + \Delta x, y)$, $(x, y + \Delta y)$, $(x - \Delta x, y)$, $(x, y - \Delta y)$, being $\Delta x = \Delta y = 0.3mm$, for a given (fixed) z-plane.λ was taken as 0.02 and α was taken as 0.01 for the simulated LR images.

4.2.2 Simulation results

The results of the numerical simulation are depicted in Fig. 4.2. Fig. 4.2(a) shows the optical absorption distribution used for the forward simulation, which represents a resolution target phantom (USAF) typically used as a characterization tool in optical imaging. Fig. 4.2(b) shows the LR OA image reconstructed by using the FBP algorithm by considering a pixel size of 100 μm whereas Fig. 4.2(c) presents the HR image obtained by interpolation from the reference image in Fig. 4.2(b). Fig. 4.2(d) displays the HR

image obtained by interleaving the LR reconstructions obtained with 4 scanned slices translated in the same plane. The HR image obtained with the PSR method from the same 4 slices is shown in Fig. 4.2(e). From the zoomed in areas shown in Fig. 4.2(f) – (i) and from the line profiles shown in Fig. 4.2(j), (k), we see that the proposed PSR method significantly improves the image resolution.

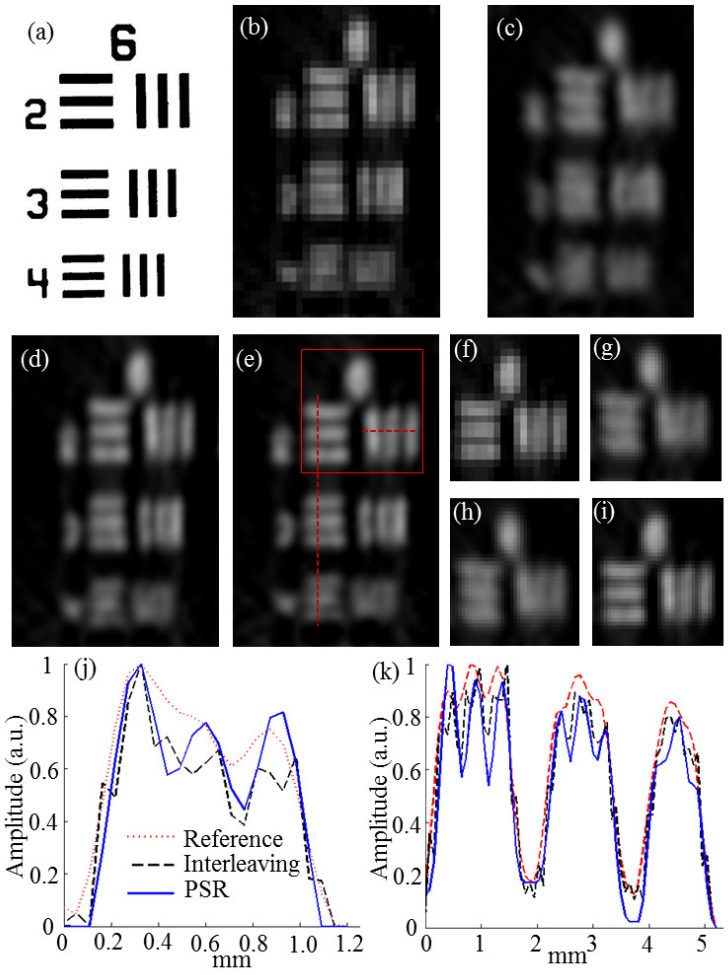

Figure 4.2: Simulation of PSR algorithm. (a) Reference USAF phantom. (b) Low resolution (LR) reconstructed image. 4 LR images with 3pixels shifts were used to obtain a higher resolution image using (c) Interpolation, (d) interleaving and (e) PSR. The figures (f-i) are the zoom-in of the region marked in red in for panels (b-e) respectively. The line profiles in the horizontal and vertical directions marked in panel (e) are represented in (j) and (k) respectively for the interpolation (red), interleaving and PSR (blue) methods.

4.3 Implementation of PSR in optoacoustic tomography

In order to test the experimental performance of the PSR method in OA tomography, experiments were conducted using a small animal MSOT256-TF scanner (iThera Medical GmbH, Munich, Germany). The resolution of the system depended on the frequency response and the geometrical properties of the detector array, and was estimated as $\approx 150\mu$m in the cross-sectional plane and $\approx 800\mu m$ in the normal direction. The MSOT system integrate high-precision stages able to translate the scanning sample in steps of 0.1 mm. The PSR algorithm was first implemented in the translation mode by combining sets of four LR images acquired in four translation scanning positions (Fig. 4.2). Specifically, the sample was scanned to the positions $(x+\Delta x, y)$, $(x, y+\Delta y)$, $(x-\Delta x, y)$, $(x, y-\Delta y)$, being $\Delta x = \Delta y = 0.3mm$, for a given (fixed) z-plane. In addition, the PSR algorithm was also implemented in a "transaxial mode", which combined translation and rotation. The transaxial mode acquired three LR images for each translational position using virtual rotations $\phi \pm \Delta\phi$, where $\Delta\phi$ corresponded to the angular separation of 5 consecutive elements of the array in the transverse plane between successive acquisitions. In the translation mode, the geometric transformation at different imaging views was applied precisely and all transducer elements (256 elements) were considered for all reconstructions. Only 200 transducer elements were used for the reconstructions in the transaxial mode, and the virtual rotation was simulated by selecting the transducer elements considered. The schematic of the MSOT256 system and the modes of operation for achieving OA-PSR are illustrated in the Fig. 4.3. Because the MSOT transducer array is toroidally focused, the best quality image is generally obtained with the sample located on the focus area of the detector. For a fair comparison, the quality of cross-sectional reconstruction was determined by visual inspection and the best image was chosen as the reference image for the PSR process. Signals of 200 channels in the central area of the detector were considered for reconstruction of the reference image in the transaxial mode.

The OA images for all scanning positions were reconstructed with a standard filtered back-projection (FBP) algorithm [34]. Prior to reconstruction, the OA signals were band-pass filtered with cut-off frequencies between 0.2 and 7 MHz in order to remove low frequency off-sets and high frequency noise. A uniform speed of sound (SoS) of 1510 m/s was used for each reconstruction. Indeed, even if the SoS variations from one medium to another can cause of distortions in the OA images, using a constant SoS value generally allows obtaining a representative image [55]. Thereby, the values of SoS were optimally chosen for each image by using iterative autofocusing metrics. A model-based reconstruction method employing similar regularization as the PSR method was used as a reference (shown in Fig. 4.6) for comparison of the proposed method vis-à-vis advanced reconstruction methodologies [15]. All LR images are mathematically registered to the reference image for calculation of the image transformation. For comparison, the transformation information between the reference image and each LR images were interpolated into the reference image to obtain the so-called interleaving image. The interleaving image corresponds to a two times up-sampled LR image with the same size as the PSR image. For the translation or transaxial mode, the image obtained at the

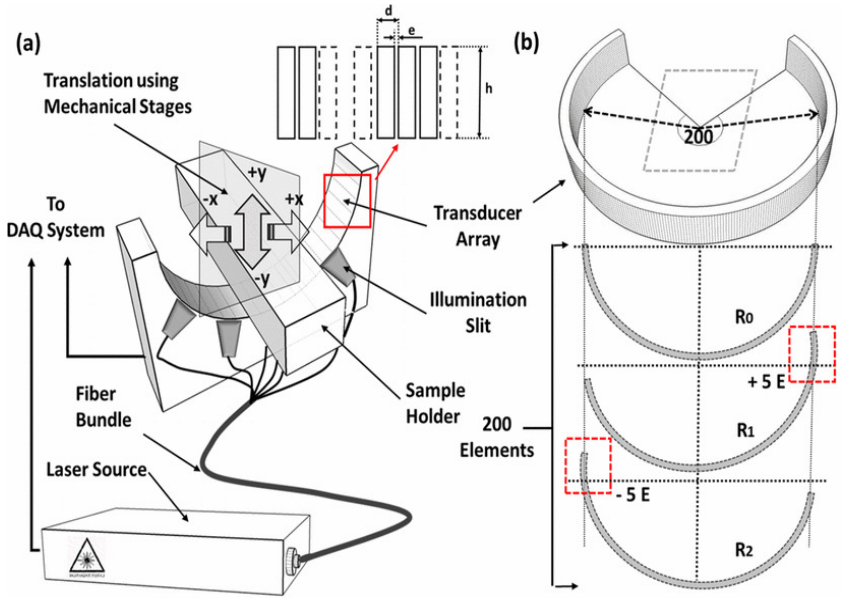

Figure 4.3: Schematic of the MSOT256 system with the detector and laser arrangement, the sample holder is connected to mechanical stages for translation of the sample. The configuration of the detector arrays is shown in the zoom-in, the system comprises of 256 cylindrically focused individual detector elements. (a) Translational (X and Y directions in a single Z plane) and (b) transaxial scanning modes. The sample is translated four positons (in X and y) in the translational mode and detectors are virtually rotated for three configurations (r0–r2) in the transaxial mode to acquire the data stack for super-resolution image formation.

focus area was taken as the initial guess for the HR image. The transformation matrix was calculated between the guessed HR image and LR images obtained in other positions. In each iteration of the PSR inversion problem, the reference image was updated with the interleaving image, and the motion between the LR images and the updated reference image was then calculated. The PSR procedure was iteratively updated until the difference error was less than 0.02 or after 12 interactions. λ was taken as 0.02 for all data, while α was taken as 0.01 for the simulated LR images and, was increased to 0.05 for smoothing noise of the reconstructed PSR images in the USAF and mouse tissue experiments. The reference images shown in section 4.3 were reconstructed with the FBP algorithm considering the same pixel number and width as the PSR image.

In order to compare the image contrast of the resolution target phantom, the average intensity (S) of the resolution lines were calculated, as well as the standard deviation of background (B) signals in the spaces between the lines. The region of interest for calculating for resolution line was established by digitally masking the image with the known location of the target lines. The ratio of the average signal to the standard deviation of background noise provided a contrast-to-noise ratio $CNR = 20 * log(S/B)$.

Table 4.1: Contrast ration CNR for optoacoustic images in translation mode

Image type	Contrast Ratio			
	Line 1	Line 2	Line 3	Line 4
Native Resolution	2.1*	1.2*	1.9*	1.1*
Interleaving	1.8	0.5	1.7	0.6
PSR (Proposed)	3.2	3.8	2.8	1.9

* *distortions present*

4.3.1 Measurements of resolution (USAF) phantoms

Experiments were performed to validate the simulation results and characterize the resolution improvement achieved with the PSR method in practical cases. We used a printed paper (USAF resolution target, standard inkjet printer with black ink) phantom embedded in a 1.9 cm diameter diffuse agar cylinder (6% by volume Intralipid in the agar solution) for the measurements. The structure of the phantom is shown in Fig. 4.4(a). The image object includes several groups of elements of different size, which can be used for resolution characterization at different levels. Four OA images of the resolution target phantom were obtained in the translation mode and twelve OA images were acquired in the transaxial mode.

The experimental results corresponding to the two-dimensional USAF target paper phantom imaged in the translational mode described in Section II-C are given in Fig. 4.3. Fig. 4.4(a) displays a photograph of the printed structure. The LR OA images are reconstructed with the FBP algorithm by considering a pixel size of 62.5 μm and the reference image (reconstructed with same pixel number and width as the PSR image) is shown in Fig. 34.4(b). The image obtained by interleaving 4 translational scans is shown in Fig. 4.4(c). The PSR image reconstructed from the same 4 positions is shown in Fig. 4.4(d). Much like in the simulations, the PSR image has higher resolution and quality as observed in the zoomed areas in Fig. 4.4(e) – (g) and in the line profiles in Fig. 4.4(h), (i) comparing to other approaches. Specifically, line features in Fig. 4.4(e) are seriously distorted (e.g. labels 3, 4 and 8) and discontinuities (e.g. labels 1, 6 and 7) can be observed. The line features in the interleaving image [Fig. 4.4(c)] are also distorted and noisy. On the other hand, the lateral (e.g. labels 3 and 4) and axial (e.g. labels 7 and 8) resolution characterization lines are more distinguishable in the PSR image. The lateral and axial line profiles marked by the red arrows in Fig. 4.4(d) also suggest a better resolution in the PSR image. The comparison of contrast-to-noise ratio (CNR) achieved with the different methods is showcased in Table I. The PSR image provides a CNR more than 50% higher than the reference image and 50% higher than the interleaving image (Table 4.1).

Fig. 4.5 shows the results of the USAF phantom experiment imaged in the transaxial mode by considering different numbers of LR images. The images obtained with the interleaving and PSR methods considering 1 transaxial scanning positions (3 images) are shown in Fig. 4.5(a) and (c). The corresponding results obtained using 3 transaxial

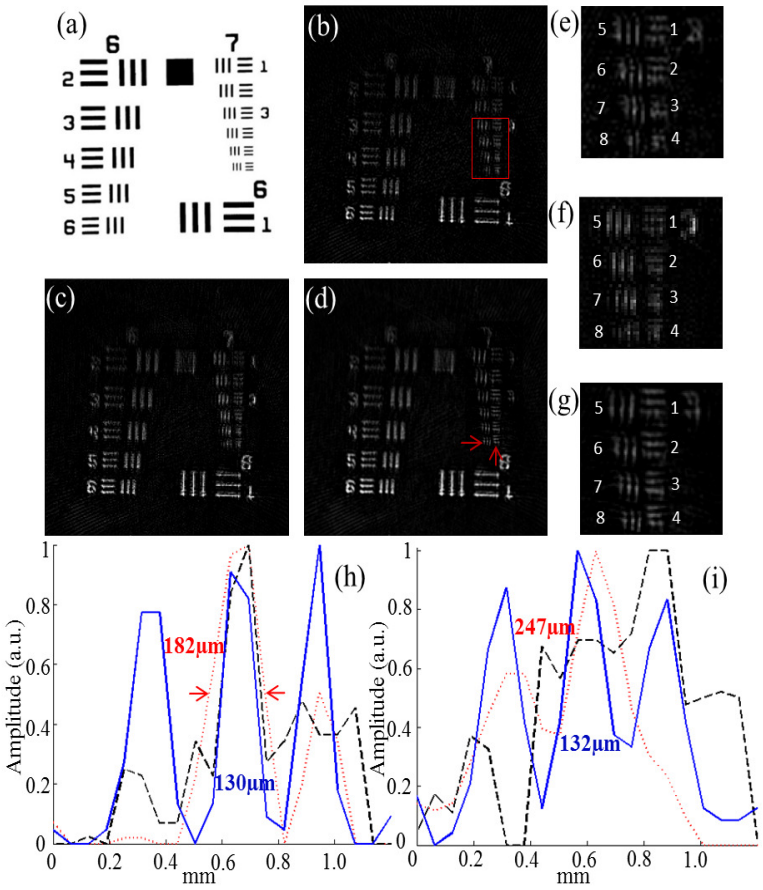

Figure 4.4: (a) Reference USAF phantom printed on white paper with black ink, which was embedded in scattering agar. (b) Reconstructed high resolution reference image. Low resolution (LR) images were reconstructed using back projection, 4 LR images with 0.3mm shifts in linear direction were used to obtain a higher resolution image using (c) interleaving and (d) PSR. The figures (e-g) are the zoom-in of region marked in red in panel b for the panels (b-d) respectively. The line profiles in the horizontal and vertical directions marked in panel (d) are represented in (h) and (i) respectively for the high-resolution reference image (red), the interleaving image (black) and the super-resolution image (blue).

positions (9 images) are displayed in Fig. 4.5(b) and (d). The image in Fig. 4.4(b) is also considered as a reference. Targets in the PSR results are better resolved comparing to the reference and interleaving images. Comparing the horizontal (labeled 1, 2, 3, and 4) and vertical (labeled 5, 6, 7 and 8) resolution characterization lines in Fig. 4(c) and 4(d), it is observed that increasing the number of LR images also leads to a better resolution of the PSR images. Fig. 4.5(e) and (f) shows the relationship between the CNR (labels 4 and 6) and the number of LR slices used in PSR method. It is shown that increasing the number of LR images for PSR reconstruction generally leads to an increase in the CNR. However, the CNR may decrease because more noise is accumulated with the number of

LR slices increasing in the PSR process; the same is clearly demonstrated in Fig. 4.5(e), (f) where the CNR value is decreased when more than 9 LR images were used.

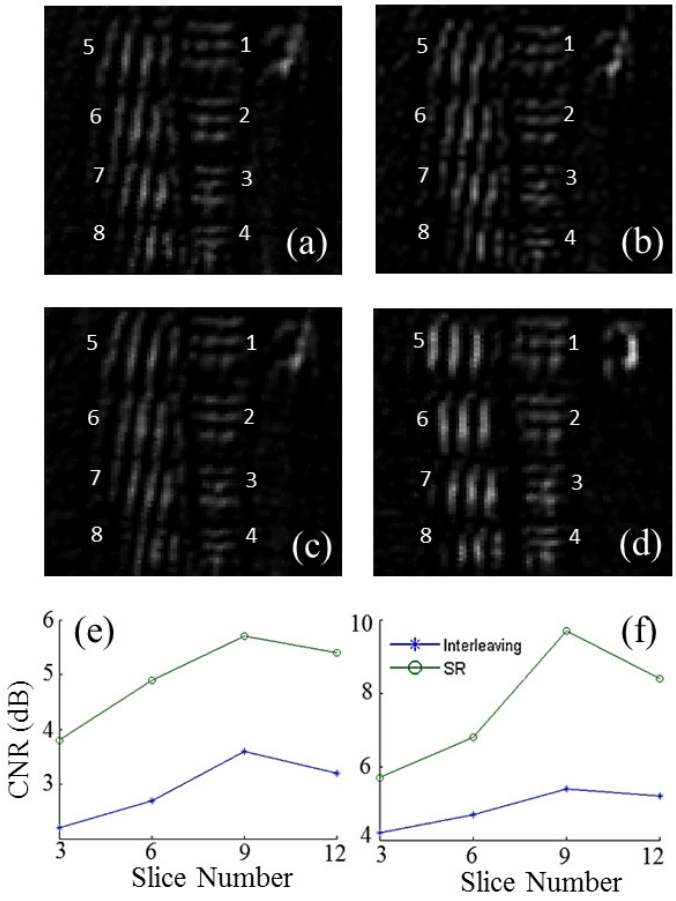

Figure 4.5: Low resolution (LR) images were reconstructed using back projection with 0.3mm shifts in the linear direction (translational) and 5 element shifts (rotational). Higher resolution image reconstructed using (a) interleaving 3 images (1 transaxial position), (b) Interleaving with 9 images (3 transaxial positions), (c) PSR with 3 images (rotation) and (d) PSR with 9 images (rotation + translation). The plots in (e) and (f) show the relationship between the number of slices and CNR for areas 4 and 6 respectively.

4.3.2 Ex-vivo tissue imaging

To demonstrate the applicability of the method in biological imaging, we conducted trials using ex-vivo murine kidney samples. The samples were extracted post-mortem (non-perfused) according to institutional regulations (with permissions from the authorities of Upper-Bavaria region) regarding animal handling protocols and subsequently embedded in a diffuse agar block (6% by volume Intralipid in the agar solution) for ensuring uniform

illumination of the sample. After completion of OA imaging experiments, the sample was isolated and frozen at $-51°C$ for 24 hours. It was thereafter embedded in a water soluble optimal cutting temperature compound and cryosectioned with sample thickness of $20\mu m$ at a temperature of $-20°C$. The RGB images of the cryosections were used as a reference to validate the reconstruction and PSR results by correlating the location, orientation and morphology of the blood vessels within the kidney mass.

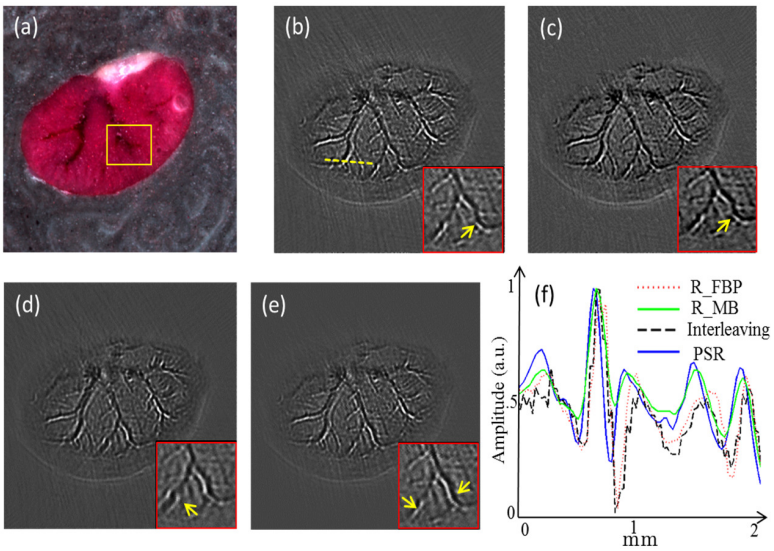

Figure 4.6: Reconstruction results for the ex-vivo murine kidney. (a) Reference cryoslice image. (b) Reconstructed high-resolution reference image with the FBP method. (c) Reconstructed high-resolution reference image with the model-based method. (d) Interleaving result with 6 images obtained in the transaxial mode. (e) PSR image. The line profile marked on (b) is shown in (f). Zoom in of the region marked in panel (a) is provided for better visualization of the microvasculature and image enhancement achieved by different methods.

The results for the ex-vivo kidney experiment are presented in Fig.4.6. A photograph of a cryoslice obtained through the imaging position is shown in Fig. 4.6(a). Fig. 4.6(b) and (c) show reference images obtained with the FBP and model-based algorithms by considering 400×400 pixels with pixel width $50\mu m$. The interleaving result [Fig. 4.6(d)] obtained by directly registering information from different scanning views reconstructed with FBP shows similar image fidelity to the reference image. In contrast, the PSR image considering 6 slices reconstructed with FBP in the transaxial mode displayed in Fig. 4.6(e) demonstrates improvements on image quality. Specifically, blood vessel structures marked with the box indicated on Fig. 4.6(a) are better resolved in the PSR image than in the images obtained with other methods, as shown by inserts in Figs. 4.6(b)–(e). The vascular structures [as indicated by arrows in the inserts in Figs. 4.6(b)–(e)] in the PSR image show better structural integrity and conformity when compared to the reference images and the interleaving image. The visual evaluation is further corroborated by the line profile drawn over a given image segment [indicated by the dashed-line in Fig. 4.6(b)], which indicates that blood vessels are better resolved in the PSR image. In

addition, the PSR image has significantly less streak-type artefacts as compared to the other images, so that the background noise is reduced.

4.4 Discussion and conclusions

We developed a novel geometrical pixel super-resolution method achieved using joint reconstruction -image processing techniques, and implemented for state of the art OA (tomographic) imaging system. The proposed PSR method utilizes multiple LR post-reconstruction OA images with geometrical proximity to efficiently integrate the information into a HR image. In this chapter, we illustrated the OA-PSR method and its' performance in enhancing the image resolution and contrast for cross-sectional OA imaging. The OA-PSR method can easily be extended to a wide range of imaging systems by properly defining and customizing the scanning protocol for individual systems. Thus, using our method researchers can overcome limitations of the system hardware and reconstruction methods by simple geometrical manipulations of scan protocol and sequences.

Using OA-PSR the we were able to improve image resolution in both the lateral and axial directions, and the findings were validated through simulations and experiments conducted with a USAF resolution target phantoms. The resolution characterized as FWHM along the lateral direction of the line target was improved from $180\mu m$ in the reference image to $130\mu m$ in the PSR image, and the FWHM value along the axial direction was improved from $247\mu m$ to $132\mu m$ respectively. The small target resolution lines (obtained for a single imaging position) were distorted and blurred in the native resolution (reference) image, and blurred in the interleaving image retrieved by considering several positions. However, OA-PSR image (considering several positions) was free of the distortions and blurry effect, additionally showing better CNR performance. The image quality of larger line targets were also enhanced with the OA-PSR method, and an improvement of CNR can be observed. Thereby, the PSR method reduced distortion of line features and enhanced image contrast at different resolution scales.

Furthermore, we have shown that increasing the number of LR images obtained along different imaging views improved the image quality of the OA-PSR result. Notably, increasing the number of LR images in the super-resolution process may result in integration of reconstruction errors and noise in the resulting OA-PSR image, especially when the image quality of the LR images is low. For the noisy images, the regularization parameters can be further optimized to smooth the noise. However, high regularization will lead to blurring in the resulting PSR image. Also, the number of scanning positions for a specific OA system may be controlled. Therefore, the optimum number of low-resolution images to consider for the OA-PSR must be determined according to the achievable image quality enhancement and the practicability in different imaging setups. On the other hand, the experiments on an ex-vivo mouse kidney illustrate the potential of the OA-PSR method for improving the image quality of in real biological samples, specially for imaging of vascular structures.

Although the improvements in image quality using OA-PSR come at an incremental computation overhead, the method can potentially improve imaging accuracy by acquiring multiple LR images and combining them algorithmically on a software platform, instead of having a slower HR acquisition achieved through averaging the signal data over multiple cycles (typically 10 frames). The processing time grows with the number of LR images used in the OA-PSR process, both in terms of signal acquisition time as well as in image reconstruction and processing. Thereby, a trade-off between OA image quality and image formation speed generally exists. This is particularly significant during *in vivo* measurements, where the system dynamics can vary within a very short time window. Numerically, the total time for reconstructing 4 LR images and subsequent processing with the OA-PSR method for $400 \times 400 pixel^2$ is about 1.33 times of the reconstructing time of the HR reference image, which has half pixel width (total pixel resolution is doubled) of the LR image. Also, total execution time of OA-PSR processing was five times faster than the computation time of the model-based reconstruction in Fig. 4.6(c). The image reconstructions and super-resolution processing can be further accelerated by paralleled computing with graphics processing units (GPU), which can potentially improve the applicability of the OA-PSR method further.

There exists limitations in the OA-PSR implementation that should be addressed for performance optimization. We acknowledge that the OA-PSR method is sensitive to the noise level of the LR image. However, suitable regularization or denoising methods can be applied for noise suppression. The noise level affects the registration accuracy in the PSR process, which diminishes the resolution. Thereby, improvements in the OA reconstruction and pre-processing methods can potentially lead to removing noise and artifacts, and prevent noise signals being registered in the final HR images. Furthermore, the accuracy of registration methods significantly affects the image quality of PSR-MSOT imaging. For ex vivo experiments, fast linear motion estimation method can be performed simultaneously with the OA-PSR process. However, the method can be significantly challenging in applications *in vivo* due to cardiac or respiratory motions. In this case, advanced registration methods, such as nonlinear subpixel registration method [165], may be employed for estimating the motion between different images. We are experimenting with the possibility of using the temporal (space-time superresolution) [166] and multispectral information [167] to build new PSR algorithms as well.

Overall, the successful application of pixel super-resolution techniques in OA imaging implies the general applicability of this methodology to increase image resolution and quality. The demonstrated enhancement of resolution and contrast in experiments with tissue-mimicking phantoms and actual biological tissues showcase that OA-PSR has the potential to become an useful tool for clinical practice and biomedical research. The method will allow delivering higher imaging resolution without significant hardware upgrades can be achieved. As a potential follow-up work, future research should aim to investigate the different motion correction methods for *in vivo* PSR-MSOT imaging, and integrate the developed methodology with the experimental clinical OA scanners.

5 Biomedical imaging applications

MSOT is a potent technology for biomedical imaging applications, given its capability of high resolution three dimensional (3D), real-time, spectrally resolved visualization of molecular probes located deep in scattering living tissues. In the earlier chapters we have focused primarily on technical developments of MSOT, in the current chapter we illustrate two application studies of MSOT. In the first application (section 5.1), we describe a novel use of MSOT imaging in artificial reproduction, with Brilliant cresyl blue (BCB) as a supravital contrast agent. Inspite of the recent developments in medical imaging, a non-destructive method that reliably predicts the developmental competence of an oocyte inside an ovarian follicle is conspicuously lacking. Thus, we utilized the multi-wavelength acquisition and spectrally resolved imaging capabilities of MSOT to obtain biologically relevant information without damaging the oocytes or diminishing their viability. The method allows us to visualize both the anatomy and contrast agents, and gain precise folliculometric information, including volume, anatomical position and oocyte size. The non-invasive nature of this approach enables *in vitro* culture of the isolated oocytes. Best to our knowledge, our study is the first to employ contrast enhancement in ovarian imaging, and to demonstrate the capability of MSOT for non-destructive ovarian follicular imaging which will be of great benefit to *in vitro* fertilization (IVF) studies.
More recently our group has developed a portable spherical array probe for volumetric real-time multispectral optoacoustic imaging (vMSOT) at centimeter scale depths, which has successfully provided superior imaging speed and suitability for the 3D visualization of tissues, and also yielded detailed *in vivo* volumetric images on a mesoscopic level [168]. The second application study (section 5.2), utilizes the vMSOT system to conduct intravital imaging of tumor masses and internal organs of small animal, and study perfusion profile in real time. The investigations illustrate hypoxia and nutrition gradients as well as cell viability, proliferation and drug response potentials in solid breast cancer tumor masses. The findings are vital in understanding the dynamics of living tissues and disease prognosis and progression [9, 6].

Parts of this chapter has been adapted with modifications from:

[1] Dutta R*, **Mandal S***, Lin HC, Kind A, Schnieke A, Razansky D., "Multispectral optoacoustic tomography enables non-destructive imaging of mammalian ovarian follicles for artificial reproduction," *In review (Nov '16)*

[2] V. Ermolayev, X. Dean-Ben, **S. Mandal**, V. Ntziachristos, and D. Razansky, "Simultaneous visualization of tumour oxygenation, neovascularization and contrast agent perfusion by real-time three-dimensional optoacoustic tomography," Eur. Radiol., pp. 1–9, 2015.

5.1 Non-destructive imaging of mammalian ovarian follicles for artificial reproduction

Medical imaging technologies are a cornerstone of artificial reproductive technology (ART) for the treatment of infertility in human medicine, and improvement of animal productivity in agriculture [169]. Existing diagnostic imaging technologies, such as pelvic magnetic resonance imaging (MRI) and ultrasound, have provided valuable insights into the mammalian reproductive system. However, the imaging contrast and spatial resolution of these methods are far inferior to those routinely obtained with optical microscopy. Ultrasonographic follicular imaging, the primary tool for oocyte retrieval in IVF and embryo culture, reveals the growing follicle only as a black bubble [170]. Folliculometric information, such as follicular wall thickness, is determined by manual or semi-automated segmentation and provides only crude information with questionable predictive value [171]. Determination of oocyte quality is vital in assisted reproduction, but there has yet been no assessment method that does not disrupt the follicle. Researchers and clinical practitioners need an innovative imaging method that reliably predicts oocyte viability and developmental competence. A non-destructive method that reliably predicts the developmental competence of an oocyte inside an ovarian follicle would be of great benefit to in IVF studies. Our investigations illustrated a novel method for non-destructive evaluation of oocyte quality using MSOT [4] in conjunction with BCB [172], a relatively new red-region contrast agent. Multi-wavelength acquisition and spectrally resolved reconstructions provided unprecedented image contrast without damaging oocyte viability. MSOT allows one to visualize both the anatomy and contrast agents [173] and gain precise folliculometric information, including volume, anatomical position, and oocyte size. The non-invasive nature of this approach enables further in vitro culture of the isolated oocytes. We attempted for the first time contrast enhancement in ovarian imaging and demonstrated the capability of MSOT for non-destructive ovarian follicular imaging. BCB has previously been used effectively to identify developmentally competent oocytes without reducing oocyte viability [172, 174, 175, 176]. BCB is reduced by the intracellular activity of glucose-6-phosphate dehydrogenase (G6PDH), a pentose phosphate pathway enzyme, the activity of which gradually decreases as oocytes reach growth phase [177]. Oocytes in mature growth phase do not reduce BCB and exhibit a blue colored cytoplasm (BCB+ve). Growing oocytes have a high level of G6PDH activity, resulting in a colorless oocyte cytoplasm (BCB−ve) [178]. But contrast enhancement using BCB has not so far been attempted in ovarian follicle imaging.
MSOT is capable of selectively quantifying the distribution of specific biomarkers using multiple excitation wavelengths and delivers optical contrast at unprecedented resolution and penetration depths [6]. It has previously been applied to specific imaging of fluorescent proteins in model organisms [4], and for tracking perfusion profiles of contrast agents and blood oxygenation *in vivo*. MSOT utilizes non-ionizing radiation (near-infrared range) [28] with safe levels of optical flux (< 15mJ/pulse on the surface of the imaged tissue), making it attractive for non-destructive cellular imaging. Our imaging trials were conducted *in vitro* by injecting BCB into porcine ovarian follicles

and imaging the intact ovarian structure ex vivo. Spectral unmixing [84] and image analysis techniques were used on acquired MSOT images to quantify image contrast and identify suitable follicles with competent oocytes. To investigate whether the procedure harmed the oocytes in any way, oocyte follicles were isolated and cultured *in vitro* then analyzed by real-time and reverse transcriptase PCR and DNA fragmentation analysis. The obtained results support the usefulness of BCB contrast enhanced MSOT as a simple, gentle and efficient imaging method for monitoring oocyte viability.

5.1.1 Optoacoustic imaging protocol

5.1.1.1 Characterizing the BCB as an OA contrast agent

BCB contains a primary amine on the benzenoid structure (Φ-NH2), a tertiary amine (R3N) and a quaternary ammonium salt (R4N+), the chemical structure [172] is included in Fig. 5.1). The optical and OA response of BCB was characterized using spectroscopic measurements (Ocean optics USB4000-FL, Bandwidth: 351-1043nm) and direct OA measurements with different concentrations of BCB diluted in Dulbecco's phosphate-buffered saline (DPBS). Spectroscopic measurements show the absorption peak BCB to be at 620 nm. However, this wavelength cannot be used for direct OA measurement because the laser is optimized in the range 680-900 nm for maximum tissue penetration. We measured the OA spectrum by placing a fine bore polyethylene tubing (0.86mm ID and 1.27mm OD) embedded within a diffusing agar block (for uniform illumination) and perfusing BCB solutions at six different concentrations. The stock solutions (1 M) were diluted to achieve the desired concentration of 13mM. The signals were acquired by an array of 256 detectors (averaged signal over 4 acquisitions) using 20 wavelengths, and reconstructed using model-based method (see section 1.2 for explanation). The signals were normalized for laser power over all 20 wavelengths and the lumen of the tubing was segmented. Thereafter the spectral signal amplitude was obtained as an average of the integral intensity value across the segmented lumen, and plotted for different concentrations of solution (Fig. 5.1).

5.1.1.2 MSOT imaging protocol

Porcine ovaries were brought from a slaughterhouse to the laboratory, within one hour of collection, in a temperature-controlled box maintained at a temperature of $39°C$. Ovaries were thoroughly washed with pre-warmed ($39°C$) DPBS solution containing 0.1% polyvinyl alcohol, penicillin, and streptomycin solution. Then, 50 μl samples of 13 mM BCB were carefully injected into 4-6 mm follicles using a fine 29 G needle (Fig. 5.2.1). The ovary was then fixed using a polythene film inside the MSOT scanner. Imaging of explanted ovaries was performed by cross-sectional OA acquisition geometry using a commercial small animal MSOT256-TF scanner (Fig. 5.2.2). The signal averaged 10 times in order to improve SNR performance in acquiring cross sections of the entire ovary. The acquired signals were initially band-pass filtered with cut-off frequencies between 0.1 and 7 MHz to remove low frequency offsets and high frequency noise, and subsequently input to a reconstruction algorithm rendering a cross-sectional distribution

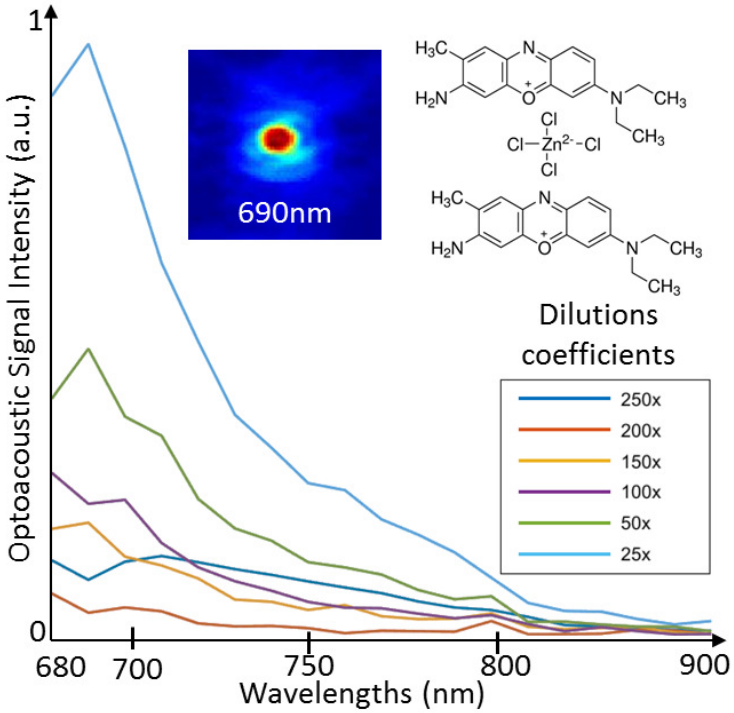

Figure 5.1: Wavelength dependent optoacoustic signal extinction curve for BCB: The optoacoustic signal responses are measured at several pre-injection dilution coefficients (x =13mM stock solution of BCB/DPBS) using the MSOT (cross-sectional) imaging at varying wavelengths. The BCB solution was perfused through a transparent fine bore polyurethane tubing (0.86mm ID and 1.27mm OD) embedded inside a scattering agar block (7% intralipid by volume). The signal values were determined by fitting an ROI and computing the mean image intensity across the ROI, each for corresponding wavelengths (20WLs were recorded) and dilution coefficients. A representative reconstructed an image (WL 690) is shown in an insert.

of the optical absorption.

The acquired images were reconstructed with the exact numerical model-based reconstruction algorithm [137]. The model-based reconstruction method provide more quantitative reconstructions by taking into account the various experimental imperfection, retaining frequency information and mitigating artifacts; thus it emerged as our choice of reconstruction algorithm. We employed a grid of 200x200 pixels corresponding to a field of view of 25 mm x 25 mm (125 μm pixel size), which is adapted to the actual resolution of the system. We used a vertex component analysis (VCA) based fast blind unmixing method [179] to map the distribution of BCB within ovarian tissue [180]. Since the internal molecular composition of fluid inside the follicles was not spectrally evaluated, the problem was treated mathematically as a two object problem – the tissue and the BCB contrast. Thus, in our approach we unmixed specifically for the presence of BCB within the ovarian follicle, given that the presence of BCB+ structure helped identify the

competent follicles. The VCA based unmixing method was able to arbitrarily identify two channels and display the corresponding spectrum. The spectra were then matched with the OA spectrum of BCB experimentally measured and mapped to the corresponding tissue components and the BCB channel. Detailed mathematical formulation of the method used and its efficacy is given by [179, 180].

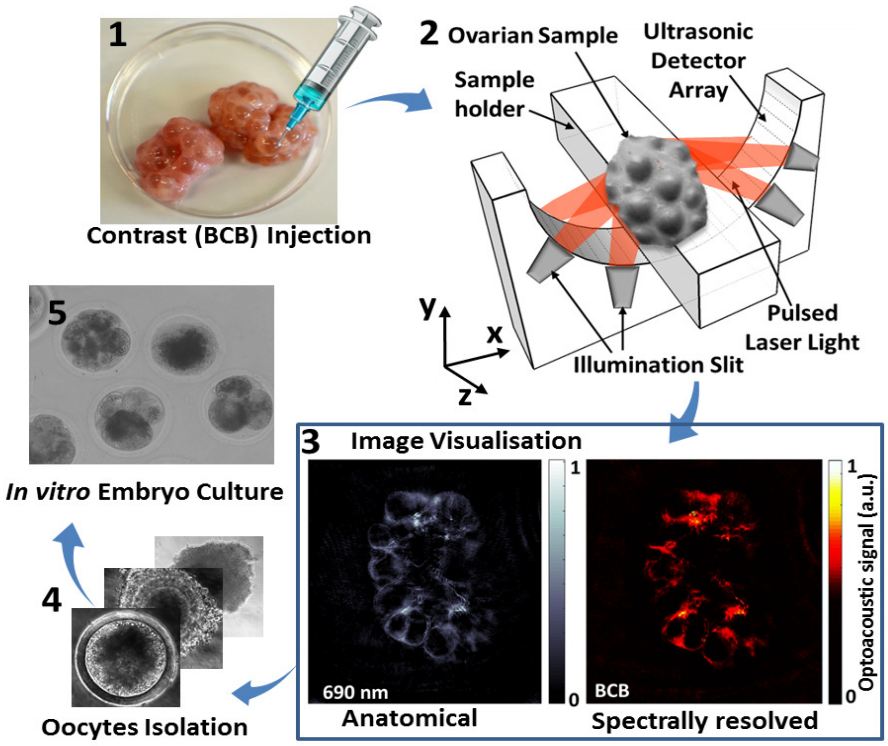

Figure 5.2: Protocol for ovarian imaging: (1) BCB was injected into the ovarian follicles using a ultrafine needle. (2) After BCB injection ovaries were imaged using MSOT. (3) Single wavelength (690 nm) image of BCB contrast enhanced ovarian follicles are shown in anatomical reference image, and the contrast from BCB molecules is spectrally resolved through a blind unmixing process using 5 wavelengths (4) Following MSOT imaging oocytes were isolated by aspiration and kept for further in vitro culture and analysis. (5) The final stage shows successful formation of the embryo from the isolated oocytes extracted from the BCB+ MSOT scanned ovarian follicles.

5.1.2 Results of MSOT imaging trials

We probed a narrow window of BCB contrast in the near-infrared range (wavelengths 680-750nm) using a commercial MSOT system (inVision 256TF, iThera Medical GmbH). Stock solutions of 1M BCB were diluted in DPBS to a 13mM working concentration. OA spectral evaluation (as illustrated in Fig. 5.1), revealed that 13mM BCB provided satisfactory signal recovery without quenching. This concentration was used throughout the experimentation and imaging trials. Fig. 5.2 illustrates the phases in the entire

ovarian imaging protocol (5 phases) standardized for the study. Ovarian follicles were first injected with BCB solution using a fine bore needle. Follicles contain fluid that further dilutes BCB, so injection concentrations were conservatively overestimated by 10% volume (Fig. 5.2.1). The ovaries were then placed on a polyethylene sheet supplied with DPBS solution, and placed in the imaging domain submerged in deionized water at 34°C for MSOT imaging (Fig. 5.2.2). In Fig. 5.2.3 the single wavelength image at 690 nm (high signal intensity at this wavelength) shows the internal anatomy of the ovary (*ex vivo*). To clearly identify the locations where BCB is deposited relative to tissue morphology, we spectrally unmixed the MSOT signals into two channels (BCB and tissue). The BCB channel showed deposition along the walls of the follicles (Fig. 5.2.3). A VCA based blind unmixing algorithm was used to identify the distribution of the chromophores (BCB). The individual follicles were isolated and the cumulus-oocyte complexes (COCs) manually extracted and visually evaluated by optical microscopy. Fig. 5.2.4 shows the microscopic images of COCs graded for validation of the results. Further, we developed automated grading algorithms based on machine learning, but a detailed descriptions of the developed method is beyond the scope of the current dissertation topic [181]. In the final stage of the workflow, we attempted *in vitro* embryo culture of irradiated oocytes (Fig. 5.2.5) to ascertain viability of the oocytes post-experimentation. Ovaries were scanned before (pre-injection) and after (post-injection) BCB was injected. We observed a clear increase of signal along the walls of the follicles post-injection, as illustrated by Fig. 5.3a. The test was repeated over 12 ovarian samples ($\approx$ 100 follicles). For quantitative evaluation we selected two ovaries and calculated the relative (normalized) signal intensity pre- and post-injection. Fig. 5.3b shows box plots of normalized intensities of 15 regions-of-interest (ROI) chosen in each ovary along the follicle walls for two independent ovarian samples. In both cases, mean intensity post injection was higher than pre-injection. The pre-injection sample (Fig. 5.3) shows slight imaging contrast due to the presence of residual blood. Thus, choosing suitable ROI (around the follicles) is essential instead taking the mean intensity value of the images, to avoid erroneous quantification from the presence of residual blood. The spread of contrast values post-injection was higher compared to pre-injection, due to the different levels of hormones and follicular volumes. Close observation revealed that some ovarian follicles show no significant changes in contrast even after injection, these are developing follicles that decolorize the BCB contrast. These BCB$-$ve follicles can thus be rejected, and oocytes are not extracted from them for further development. Finally, we generated a 3D rendering of the full ovarian mass by stacking multiple scan slices along the Z-direction scanned at a distance of 0.1mm. The 3D scan provides suitable anatomical landmarks and allows computation of follicular volume, an important marker of maturity.

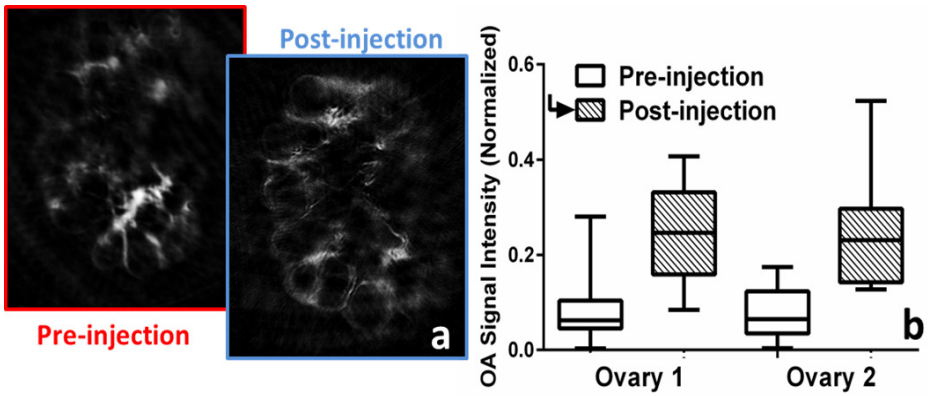

Figure 5.3: Scan of (intact) ovaries ex-vivo before (red insert) and after (blue insert) injection of BCB (diluted 100x stock solution) is shown (a). The post-injection images (normalized) of the ovaries show an increase in relative contrast values. The box-plots of contrast values for two ovaries, before and after the injection are shown (b). Fifteen (15) data-points in each ovary was chosen for evaluation.

5.1.3 MSOT as an non-destructive imaging tool

5.1.3.1 Validation of MSOT imaging using histology and SPIM studies

The MSOT system used was limited to 150μm in-plane resolution, extendable to $\approx$ 120μm using pixel super-resolution methods [182]. This resolution was optimal for visualizing BCB contrast within follicular masses, but fell short of visualizing the COCs. To validate our observations at higher resolution, a randomly chosen set of MSOT-analyzed ovarian follicles (Fig. 5.4.a) were examined by histological imaging (control) and selective plane illumination microscopy (SPIM) (insert Fig. 5.4.a, Fig. 5.4.d). A state-of-the-art SPIM system was fabricated in-house to enable ovarian follicular imaging (Fig. 5.5). A wide range of individual follicles were extracted from two different sets of ovaries and all selected samples were imaged in their entirety, as their sizes matched the camera field of view (FOV). The high contrast (signal-to-noise ratio) and image resolution achieved by SPIM readily distinguished the different anatomical features (Fig. 5.4.d). We analyzed the most relevant morphological features using the SPIM images [183], i.e. size of the developing cumulative COC and follicle wall thickness. The COC can be clearly seen attached to the inner follicle wall. COCs were detectable in approximately 70% follicles, and COC size varied between 40 μm and 110 μm (Fig. 5.4.b). Detection of COC as small as 40 μm is comparable to the resolution of histological analysis [184], and surpasses that of ultrasound biomicroscopy [185]. Histological sections obtained through cryoslicing (figure 4a) and H&E stained microscopic images served as controls (Fig. 5.4.c).

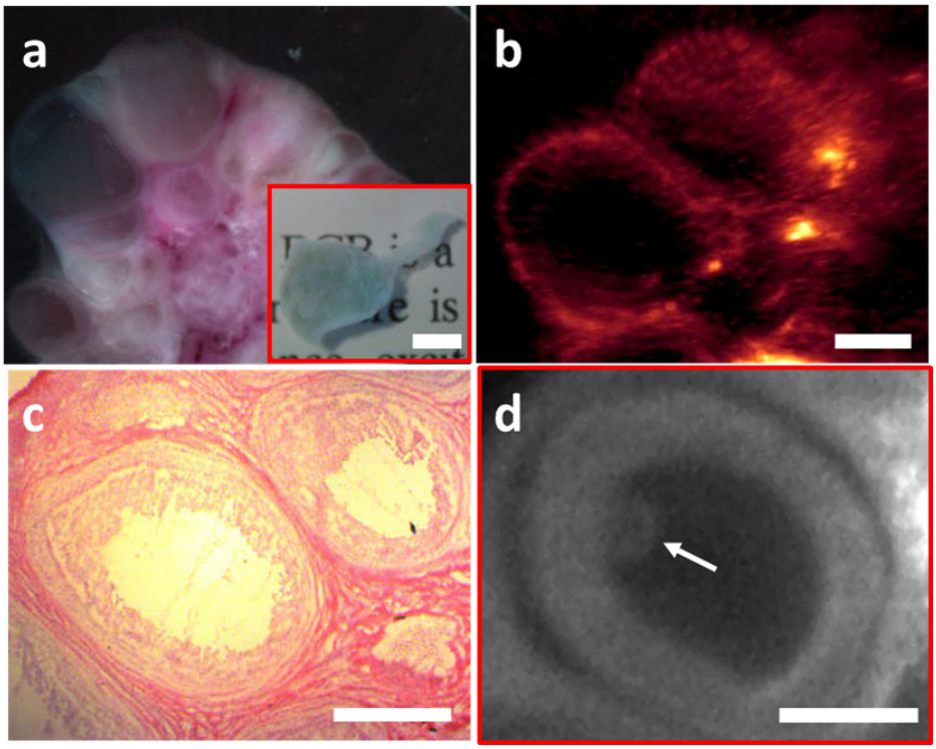

Figure 5.4: The cryosliced image of BCB+ porcine ovary (a), and the optoacoustic image of the selected ovarian section is shown (b). The histological evaluation was done using H&E stains (c), and validated using the SPIM imaging (d). Insert in (a) shows an isolated follicle which was cleared and imaged using SPIM to obtain the corresponding anatomy for validation (d), the arrow points to the attached COC. [Scalebars ≈ 1 mm]

5.1.3.2 In vitro embryo culture

We examined whether oocyte viability was harmed by laser irradiation from MSOT scanning or not. Nuclear maturation of each oocyte was scored by attainment of metaphase II, as judged by the presence of condensed chromosomes in an equatorial position and extrusion of the first polar body (Fig. 5.6). Nuclear maturation data (table 5.1) showed no significant difference in nuclear maturation rate between MSOT-scanned and non-scanned control oocytes. The MSOT scanner used (operating in NIR regime) provides a narrow, but sufficient band of wavelengths to identify signals from competent BCB (+) follicles and distinguish them from the developing follicles. This enabled suitable oocytes to be selected for *in vitro* embryo culture without disrupting follicle structure. To validate the findings, we assessed the competence of oocytes to develop further by culture *in vitro*. Oocytes aspirated from MSOT-scanned ovaries were parthenogenetically activated to indicate developmental potential. Development was scored as the number of embryos consisting of two to eight equally-sized blastomeres 48 h after activation. No statistically significant difference was observed between MSOT-scanned BCB +ve oocytes and control BCB+ve oocytes (table 5.1), indicating that MSOT scanning has

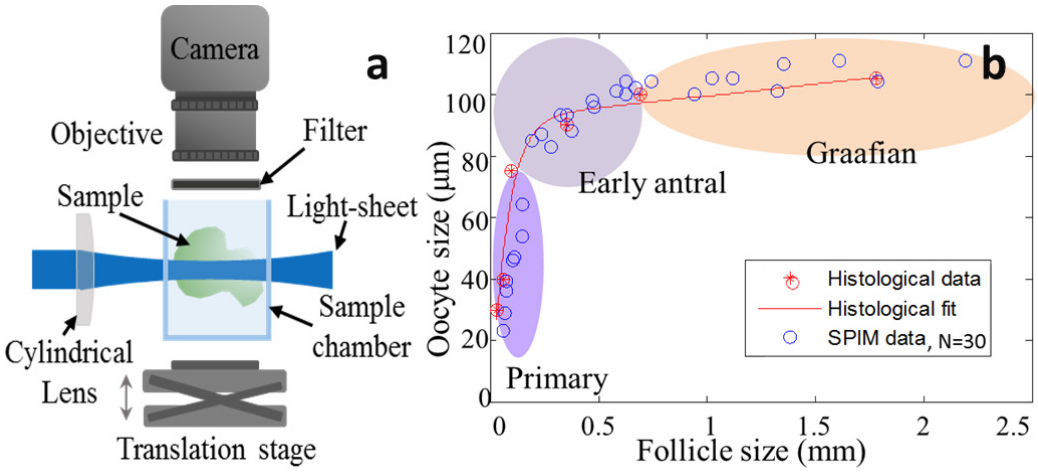

Figure 5.5: Validation of imaging studies with SPIM: (a) The construction and components of the customized SPIM system for ovarian imaging; (b) quantitative analysis of the oocyte size versus the follicle size. Blue circles are data points taken from the SPIM images. 30 data points were taken from SPIM results of two different samples. Histological data of porcine ovarian follicles previously reported in literature are shown in red. R2 (adjusted coefficient of determination) = 0.76, indicating good agreement. Follicles can be categorized according to physical dimensions as: primary (violet) with COC $\approx 60\mu$m, early antral (yellow), with COC $\approx 80\mu$m, or Graafian follicles (green) with COC $\approx 120\mu$m.

no detectable detrimental effect. As expected, nuclear maturation and parthenogenetic activation rates were significantly higher in BCB+ve than BCB–ve oocytes, as reported in goats [186] and heifers [187]. The low nuclear maturation rate of BCB–ve oocytes could be due to incomplete or abnormal cytoplasmic maturation.

Table 5.1: Nuclear maturation and parthenogenetic activation

	MSOT scanned		**Control group**	
	BCB-ve	BCB+ve	BCB+ve	BCB-ve
Nuclear maturation (%)	$85.52\% \pm 2.92$	$78.41\% \pm 3.91$	$86.48\% \pm 3.07$	$79.9\% \pm 3.82$
Parthenogenetic activation(%)	$88.91\% \pm 3.65$	$70.57\% \pm 3.28$	$87.98\% \pm 4.91$	$69.03\% \pm 5.26$

5.1.3.3 Expression of stress and apoptosis-related genes in MSOT scanned porcine COCs

Gene expression analysis of four genes chosen for their roles in cell stress and apoptosis were conducted to determine whether irradiation from MSOT scanning is stressful to oocytes. Differential expression of the stress-associated gene TP53 and three genes related to apoptosis, BCL, BAK (BCL2-antagonist/killer), and CASP3 (caspase 3),

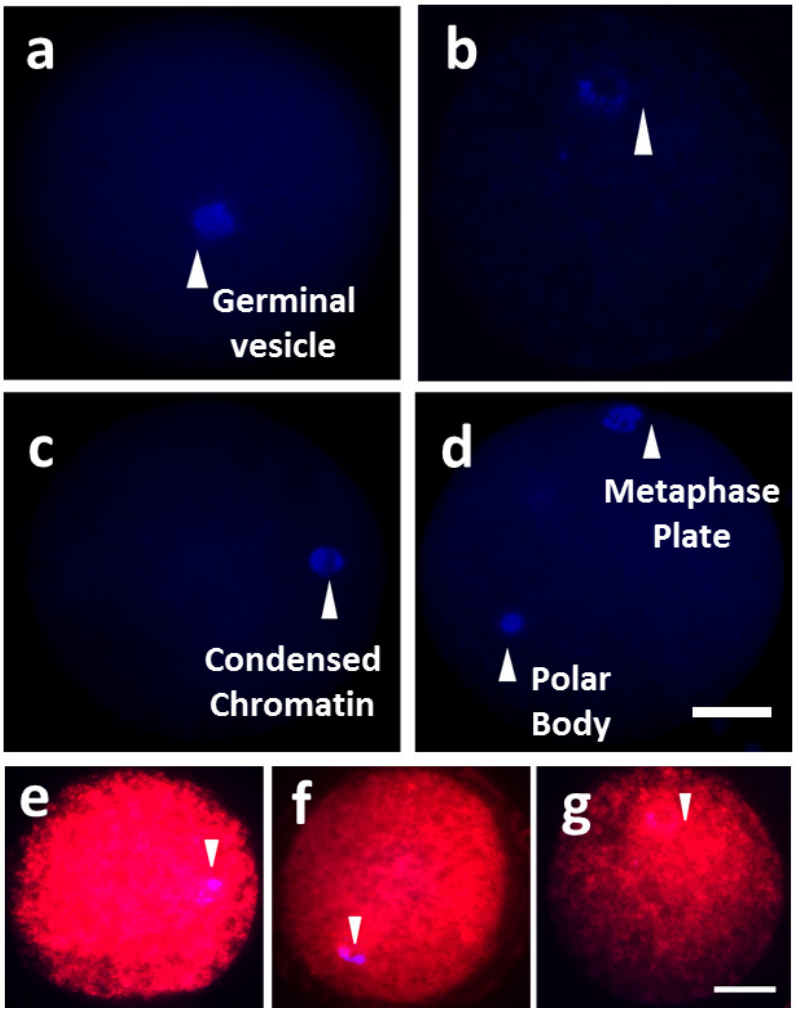

Figure 5.6: Progression of BCB stained oocytes through different stages of maturation: (a) Immature oocyte (b) Germinal Vesicle breakdown stage (c) appearance of first polar body and (d) Mature oocyte with visible polar body and metaphase plate. Mitochondrial distribution of (e) BCB+ ve oocytes showing uniform distribution with polar body and metaphase plate, (f) a control oocyte showing uniform distribution with polar body and metaphase plate and (g) BCB –ve oocyte arrested at germinal vesicle breakdown stage with non uniform mitochondrial distribution. All scale bars indicate 100μm.

was analyzed by quantitative real-time RT-PCR in two pools of 50 to 60 randomly-selected COCs from scanned and control ovaries without considering their developmental competence (Fig. 5.7). Three replicates were conducted for each experiment. Fig. 5.7b shows that no significant difference was detected in relative mRNA expression of TP53, BCL, BAK and CASP 3 ($p < 0.05$), between oocytes isolated from MSOT-scanned and control ovaries. Studies in humans and mice have revealed a clear relationship between *in vitro* culture related stress and TP53 expression in embryos [188]. BCL XL, BAK and CASP3 are members of two important regulatory families involved in apoptosis. BCL XL and BAK are a pro-apoptotic members of the Bcl-2 family that induce oocyte apoptosis when cytoplasmic levels are elevated [189].

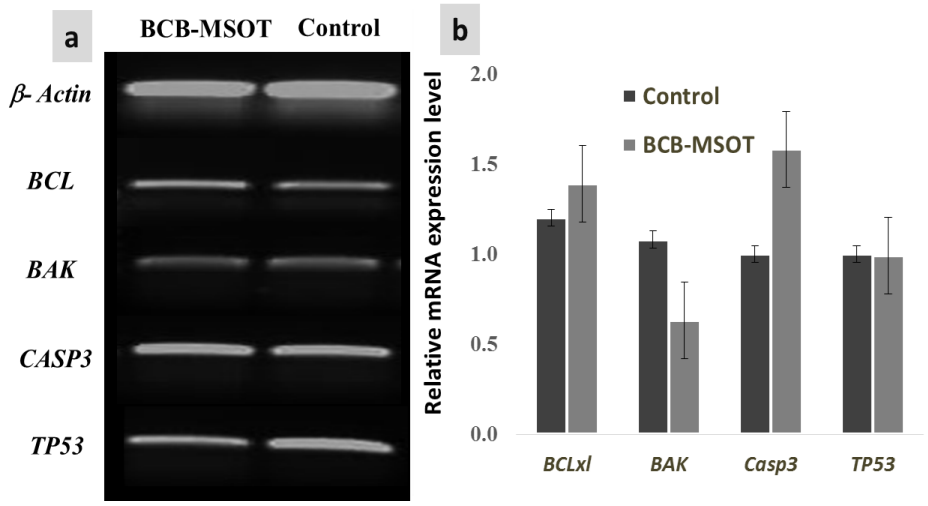

Figure 5.7: The Reverse transcription PCR of (a) apoptosis associated and stress associated genes in MSOT scanned oocytes (exposure 5-20 mins). The panel (b) shows the statistical significances for tests conducted with ß-Actin, BCL BAK and TP53 – no significant DNA damage due to BCB and/or MSOT scanning is observed.

5.1.3.4 DNA fragmentation assay

TUNEL analysis to detect DNA fragmentation was carried out as a further indicator of cell stress and apoptosis, following the protocol described previously [30](Fig. 5.8a-c). A TUNEL score was determined as the percentage of COCs showing signs of DNA fragmentation, as indicated by a fluorescent signal. There was no significant difference in TUNEL score between oocytes isolated from MSOT-scanned ovaries ($31.26\% \pm 4.23$) and from control ovaries ($30.11\% \pm 2.97$). Though it is not clear whether the BCB test could serve as an indirect marker of oocyte apoptosis, our investigation of the probable effect of MSOT scanning on oocyte quality revealed that it imposed no apparent stress on the oocyte. The average exposure time for each ovary was ≈ 25 min, with maximal flux ≈ 20 mJ cm^{-2} (per pulse) and average intensity of 200 mW cm^{-2} at the surface (at 750 nm), fulfilling the laser maximum permissible exposure (MPE) recommendations

(**ANSI** Standards). DNA fragmentation observed in immature oocytes (particularly GV and MI stages) could be a consequence of stress during maturation of the ovarian follicle, or hypoxia resulting from compromised microcirculation and correlate with aneuploidy or other chromosomal abnormalities [190, 191]. We found no evidence of DNA fragmentation in the cumulus layer in immature porcine COCs. This is consistent with a similar finding in cattle where no TUNEL signal was obtained in cumulus cells of immature oocytes [192]. Thus, the DNA fragmentation assay and relative mRNA expression of important apoptosis-related genes indicate that MSOT scanning does not cause stress to the oocytes.

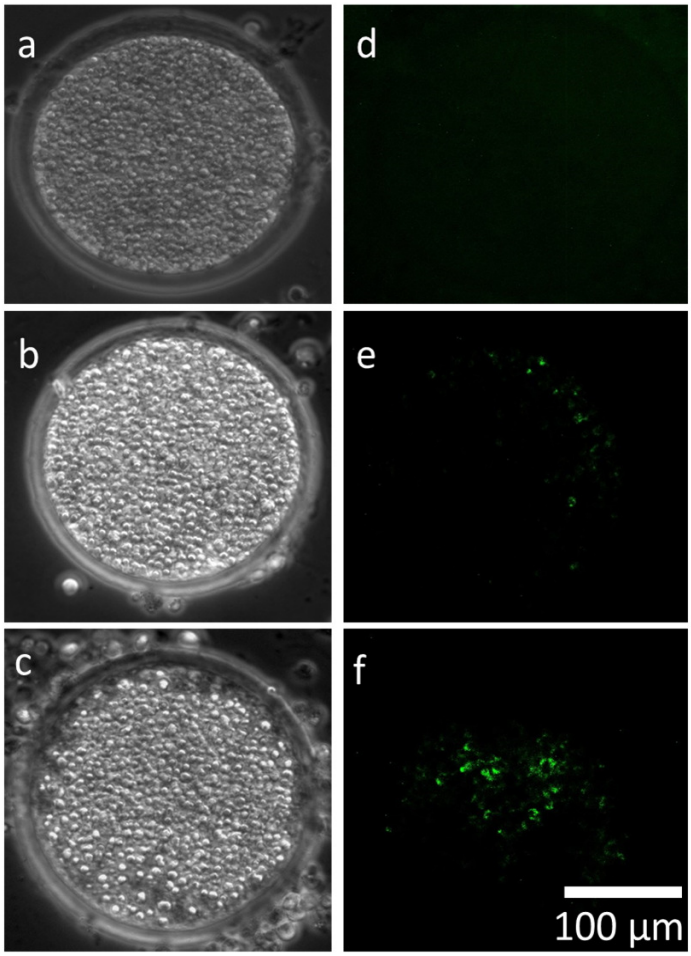

Figure 5.8: DNA fragmentation detection (bright-field images) by TUNEL assay (a) Porcine oocyte with no detectable DNA fragmentation, (b) BCB +ve porcine oocyte with DNA fragmentation, and (c) control oocyte with DNA fragmentation. The corresponding fluorescent channel images of (a-c) are shown (d-f) on the same scale.

5.1.4 Discussion and conclusion

We demonstrated a novel combination of ovarian follicle imaging with BCB as intra-vital contrasting medium using MSOT technology. The volumetric OA scanning (planar imaging plus Z-translation) provided suitable anatomical landmarks, and multi-wavelength acquisition allowed spectral resolution of the contrast agent (BCB). The anatomic scans using single wavelength OA images distinctly show the follicular antrum and theca interna layers, allowing individual follicles to be easily identified. The segmentation and volumetric evaluation of the follicles from anatomic data (as carried out in ultrasonic evaluation of ovaries) can also be achieved using the MSOT data [2, 171]. Ovarian follicles were validated by a state-of-the-art SPIM system specifically designed for ovarian follicle imaging (as in Fig. 5.5). Clearly distinguishable COCs protruding into the follicular antrum of several antral and Graafian follicles were measured at 40-110 μm, and their correlation with the developmental stage of the follicles was as described by others [184]. SPIM imaging coupled with the cryosection and histological (H&E stained) images provided a suitable measure to determine the efficacy of the BCB contrast enhanced MSOT imaging protocol. The MSOT system has lower imaging resolution but has the advantage of being non-destructive, unlike SPIM and histological analyses [183]. The high spatial resolution and high contrast offered by BCB contrast-enhanced MSOT imaging provides quantitative anatomical information similar to that obtained by ultrasonic measurements commonly used in animal studies [184] and clinical practice [171]. Furthermore, the functional capability of MSOT as an imaging modality allows (presence or absence of) BCB contrast visualization without disrupting the follicle, opening up exciting new possibilities in molecular imaging for ART. Maintaining oocyte viability was one of the most important criteria for our study and defined the choice of BCB as a contrast medium and MSOT as a non-ionizing imaging modality. Parthenogenetic activation and embryo development indicated that the imaging was harmless and analysis of DNA fragmentation and expression of important apoptosis-related genes indicated no apparent damage to the oocytes. Our investigation provides further support for the use of BCB as a safe labelling agent for oocyte selection, and demonstrates the applicability of MSOT in *in vitro* embryo production. There is immense scope for improving ovarian imaging techniques, as existing methods provide only crude information with questionable predictive value. Oocyte quality is certainly an important factor determining the outcome of ART procedures, but so far it has not been possible to test oocyte quality within a follicle. We therefore anticipate that a non-destructive method that reliably predicts the quality of the developing oocyte inside a follicle will be of great benefit. As illustrated in the current article, an approach for functional oocyte and embryo assessment by ovarian imaging with the use of an exogenous contrast agent, can indeed be a key new technology for artificial reproduction.
Future development of the approach will open new dimensions in follicular imaging delivering useful anatomical, functional and molecular information without hampering the integrity of the follicle. Possible applications include diagnosis of follicular cysts, empty follicle syndrome, and developmental studies. The poor quality of retrieved oocytes due to improper timing of oocyte retrieval is an important factor in the relatively low success

rate of human IVF. *in vivo* visualization of oocytes in situ could help practitioners to make informed decisions about timing oocyte retrieval.

5.2 4D imaging of perfusion in preclinical breast tumor model

Breast cancer is one of the leading causes of death in the female population worldwide. Despite significant improvements in survival rates over the past 25 years, approximately 522,000 deaths from breast cancer was recorded worldwide in 2012 (15% of female deaths and 6% of the total) [193]. The distressing statistics motivated us to explore the capabilities of MSOT towards breast cancer detection and management.
Breast tumors are highly heterogeneous, a detailed understanding of tumor molecular profile is thus essential for cancer management and personalized tailoring of clinical decisions. Early diagnosis, structural and functional assessment of tumors are critical for effective disease treatment and prognosis [194]. In the current study we investigate solid tumors, which are heterogeneous organ-like structures nourished by a vascular network. Neovasculature is often characterized by convoluted structure, enhanced branching patterns, excessive loops and shunts [195]. Disrupted vascular network causes limited oxygen and nutrient supply leading to metabolic and cell proliferation gradients influencing drug sensitivity [196]. Optical molecular imaging technologies play a vital role in oncology [197], and combined with highly sensitive *in-vivo* probes contribute to the understanding of functional and histological properties of tumors and anticancer therapies [198, 199, 200]. Contrary to other pure optical imaging techniques, OA provided high resolution molecular imaging at the whole-organ or whole-body scale and enables better visualization of vascular networks, blood perfusion and microenvironment gradients in cancer [201]. To further exploit the advantages, such as easy *in-vivo* handling and real-time imaging performance, small animal MSOT systems were designed based on cross-sectional two-dimensional (2D) imaging geometries [2, 37, 202], and three-dimensional (3D) rendering is then achieved by stacking multiple 2D images. However, the technique restricts real time acquisition to a cross-sectional plane within the tumor or organ, and the volumetric reconstructions obtained thereby are prone to motion problems and out-of-plane artifacts leading to quantification errors and anisotropic resolution in the volume of interest [51]. The limitations renders most of the commercial 2D scanners unsuitable for real-time *in-vivo* measurements [158, 138], and it encouraged researchers to explore spherical arrays with distributed elements have for 4D OA imaging (3D imaging in real time) [20]. More recently, our group developed a vMSOT imaging system based on a densely-packed spherical array of sensors [168]. The system integrates real-time reconstruction using a graphics processing unit and allows visualization of the 3D optical absorption distribution in real time [30]. In this work, we illustrate the capabilities of vMSOT for cancer imaging in preclinical models. Specifically, 3D intravital imaging of whole breast cancer allografts in mice was performed and compared versus the volumetric imaging performance with a standard cross-sectional MSOT system. Intrinsic tissue properties, such as blood oxygenation gradients, along with externally administered nanoparticle distribution were visualized in order to study vascularization,

probe penetration and extravasation kinetics in solid tumors. Volumetric imaging in real time enabled simultaneous assessment of perfusion kinetics in different regions of interest within the tumor and opened the way to clinical application of this technology in skin or breast diagnostics and therapy monitoring.

5.2.1 Experimental setup and tumor model

5.2.1.1 Experimental setup and signal acquisition

The vMSOT system employes a custom-made array of 256 piezocomposite detectors located on a spherical aperture (Imasonic SaS, Voray, France) which simultaneously collects OA signals from the imaged tumor. The individual elements have a central frequency of 4 MHz and bandwidth (full width at half maximum) of 4.0 MHz. Light excitation was provided through a fiber bundle (CeramOptics GmbH, Bonn, Germany) inserted in the central part of the ultrasonic array (Fig. 5.9). A tunable (690-900nm) optical parametric oscillator (OPO)-based laser (Phocus, Opotek Inc., Carlsbad, CA) generating pulses with duration below 10ns was used as a light source. The excited OA signals were simultaneously acquired by custom-made data acquisition system consisting of 256 analog to digital converters (Falkenstein Mikrosysteme, Taufkirchen, Germany) triggered by the Q-switch laser output. The vMSOT system was fixed underneath an animal lying in supine position with a custom made holder as shown in Figs. 5.10b and 5.10c. Agar and ultrasound gel were used to ensure efficient acoustic transmission of the OA signal. The resolution of the imaging system was evaluated as approximately 200μm in all three dimensions [168]. For comparison, the mice were also imaged using a cross-sectional 2D MSOT system designed by [2]. The system employed an array of 64 cylindrically-focused transducers (Imasonic SaS, Voray, France) to collect OA signals from a cross-section animal plane giving the in-plane resolution of 150μm and the resolution in z-axis as 800μm. A 10-arm fiber bundle provided illumination through the lateral sides of the array. For imaging, the mouse is covered with a transparent polyethylene membrane and fixed in the custom-built frame to place it into a water tank providing acoustic coupling and avoiding direct animal contact with water. The animal was anesthetized using an inhalation anesthesia (see also *in-vivo* imaging experiments), which was applied through the tubes and a mask integrated in the frame.

5.2.1.2 Signal and image processing

The acquired signals (256 channels) were first deconvolved with the transducer impulse response and filtered with cut-off frequencies between 200 kHz and 7 MHz. Image reconstruction for the vMSOT setup utilized a parallel implementation of a back-projection algorithm [34], whereas a two-dimensional model-based algorithm [15] was employed for cross-sectional 2D-MSOT. The reconstructed images represented the spatial distribution of the optical absorption at the particular excitation wavelength. In order to determine the distribution of specific tissue contrast, the images acquired at several different wavelengths were cross-correlated and spectrally unmixed by least-square fitting to the chromophore absorption spectra on a per-pixel basis [196]. For simplicity, optical

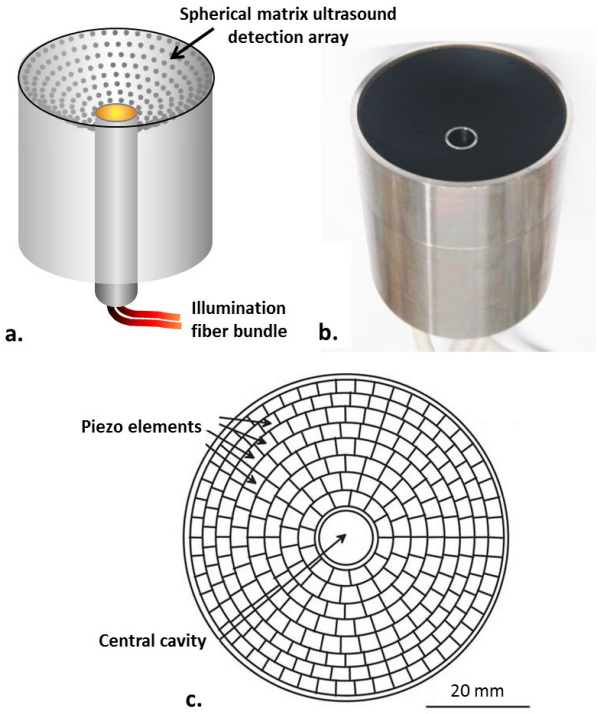

Figure 5.9: Archietecture of the vMSOT imaging sensor: The ultrasound transducer array consists of 256 elements disposed on a spherical surface covering an angle of 90°. (a) 3D scheme of the array with individual element positions schematically shown as dots. (b) Actual picture of the system. (c) Projection of the transducer with the shape of the individual piezo elements.

absorption was assumed to be caused solely by oxygenated, deoxygenated hemoglobin and externally administered agents.

5.2.1.3 Cancer model and contrast agent application

The animal handling procedures and experimentation were conducted in agreement with Helmholtz Zentrum München and Government of Upper Bavaria guidelines, and complied with German federal and international laws and regulations. 5 female 8-week old Hsd:Athymic Nude-Foxn1nu/nu mice (Harlan Winkelmann, Germany) bearing tumor allografts were imaged. The mutant nude mice represented a suitable allograft host, since defects in immune system enabled effective and reliable tumor propagation. Also, the lack of hair and melanin skin pigmentation was appropriate for OA imaging. The tumors were grown upon subcutaneous injection of 1 million (mio.) 4T1 murine breast cancer cells into the back of the mouse approximately 10 days before the imaging experiment so that the allografts reached a diameter of approximately 0.8 cm. Tumor-carrying mice were injected in the tail vein (i.v.) with 100 nmol of liposomes carrying indocyanine green (Lipo-ICG), which is characterized by long persistence (Fig. 5.11) in the vascular system (custom made). Additionally, [203] has used the 2D-MSOT to confirm Lipo-

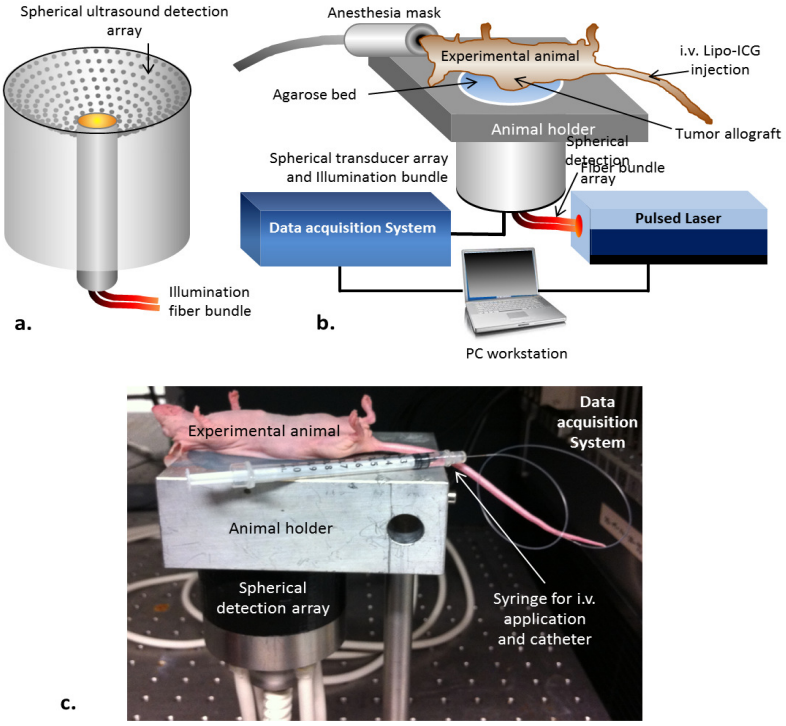

Figure 5.10: Experimental setup. (a) Sketch of the vMSOT imaging sensor comprising of a spherical matrix ultrasound detection array, (b) sketch of the experimental setup. Experimental animals bearing tumor allografts were positioned on the animal holder.(c) Photograph of the setup during the experiment. The syringe was connected with the catheter for intravenous lipo-ICG injection during the imaging experiment. (Courtesy: Eur. Rad 2016)

ICG as a potent OA agent and resolved tissue accumulation in tumor-bearing animals. The studies signify opening up new vistas in pharmacology studies and nanoparticle investigation for oncological imaging applications.

5.2.1.4 In-vivo imaging experiments

In-vivo imaging experiments were performed with nude mice tumor allografts using either inhalation anesthesia (2-3 vol. % isofluran at apx. 0.9 L/min oxygen flow) or injection anesthesia (100 mg/kg body weight (BW) Ketamine and 5 mg/kg BW Xylazine). The experimental animals were anesthetized and positioned on the custom designed animal holder (Fig. 5.10b and Fig. 5.10c). The imaging experiment was started 10 seconds before animals received 100 nmol lipo-ICG through i.v. catheter (Fig. 5.10c) in order to keep the animal position and therefore imaged area exactly the same during the whole imaging set and the entrance of the contrast agent in particular. The tumor area was imaged before and after the lipo-ICG injection using 800nm excitation wavelength (maximum absorption for lipo-ICG) for total time of 120 seconds at 10 frames per second. Afterwards, without changing the animal position, the same area was imaged at

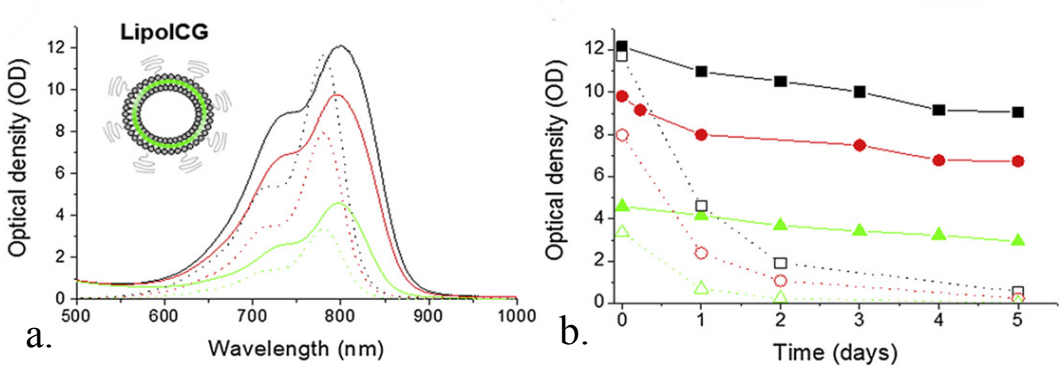

Figure 5.11: The structure of Lipo-ICG, (a) UV-Vis absorption spectra on day of preparation, and (b) maximum absorbance over 5 days of LipoICG (solid lines) and free ICG (dotted lines) at 75 μm (black lines), 50 μm (red lines) and 25 μm (green lines) ICG. Adopted with modifications from [203]

wavelengths 700, 720, 740, 760, 780, 800, 820, 840 and 860 nm. The animals were then imaged for lipo-ICG epi-fluorescent profile of the tumor and surrounding area using high resolution LucaEMR EMCCD camera (Andor Technology, Belfast, UK) and immediately afterwards brought to the 2D-MSOT equipment. Approximately 20 mm long area containing s.c. tumor with diameter of 8-10 mm was imaged with 2D-MSOT using the same excitation wavelength set as was applied at vMSOT imaging, which created an image stack of approximately 180-200 planes (dependent on the region of interest size, 0.1μm each plane). Typical 2D-MSOT imaging experiment took about 12-15 minutes time. Part of the experimental group (n=2) was imaged initially with 2D-MSOT in one optical plane through the tumor during the lipo-ICG injection with the same time setup. Subsequently, the tumor area was imaged using multispectral image stack acquisition and further with epi-fluorescence imaging and vMSOT as indicated above. All the mice were sacrificed with overdose Ketamine and Xylazine and frozen immediately after the imaging experiment for further signal validation and anatomical analysis.

5.2.1.5 Validation

The results of *in-vivo* imaging were validated using a multispectral epi-illumination cryoslicing imaging system [197]. Tumor areas were sliced and imaged with 150μm steps in either a transversal or dorsal plane. The 20μm thick cryo-slices in representative planes were taken for subsequent histological analyses and epi-fluorescence thin-section imaging (TSI). Hematoxylin-eosin staining of cryo sections was further performed (7) with the stained sections imaged using light microscope (Leica Microsystems, Wetzlar, Germany). Selected cryo-slices were also embedded with Vectashield Mounting Medium with DAPI (Vector Laboratories, Burlingame, CA USA) and imaged with a fluorescent microscope (Leica Microsystems, Wetzlar, Germany). The resulting images were combined using Microsoft Image Composite Editor (http://research.microsoft.com/en-us/um/redmond/groups/ivm/ice/) and GNU Image Manipulation Program (http://www.gimp.org/).

5.2.2 Results and validation

We successfully conducted the experiments designed, and the results were reported by [28]. We compared the vMSOT *in-vivo* performance versus the standard cross-sectional 2D-MSOT and epi-fluorescence imaging (Fig. 5.12). The animals bearing 4T1 breast tumor allografts (n=4) were imaged continuously during lipo-ICG injection at 20fps. The representative volumetric images, retrieved by the vMSOT system were characterized by nearly isotropic resolution of 200μm [168] in all three axes clearly revealing the lipo-ICG distribution in vascular network inside and around the tumor (Fig. 5.12a). In order to achieve an equivalent 3D image of the tumor area, multiple cross-sectional images (x-z plane) were acquired with the 2D-MSOT system, which took several minutes. The 2D images were combined in extra rendering step to yield a volumetric representation (Fig. 5.12b). While high-resolution 2D images were achievable with 2D-MSOT, the resulting 3D images were strongly affected by out-of-plane artifacts and rendering inaccuracies, which lead to anisotropic resolution along the z-axis [51]. Presence of artifacts and lower out-of-plane resolution hinders the visualization of vasculature in y-z and especially x-y plane, where the tumor was difficult to distinguish from surrounding tissue (Fig. 5.12b), in contrast to the corresponding image by vMSOT (Fig. 5.12a). The epi-fluorescence image of the tumor area did not provide details of the contrast distribution in the context of vascular network, but merely confirmed lipo-ICG presence in the tumor and the surrounding skin for all animals studied (Fig. 5.12c), which agreed with the expected pattern considering short time between agent application and imaging.

For further studying the perfusion kinetics with high temporal resolution, lipo-ICG entrance and perfusion in the tumor was monitored in real time using single wavelength illumination at 800 nm, i.e. lipo-ICG peak absorption and isosbestic point for hemoglobin. The imaging was started 10 seconds prior to agent injection initially detecting the background signal corresponding to intrinsic blood contrast (leftmost images in Fig. 5.13). Upon agent application one could observe temporal and spatial development of lipo-ICG signal in and around the tumor. Fig. 5.13 presents the time course of the volumetric projections in the x-y, x-z and y-z planes, which clearly demonstrated strong signal enhancement versus intrinsic blood contrast shortly after the agent application. In-vivo imaging by vMSOT revealed more details in all 3 dimensions than similar dynamic imaging with the 2D-MSOT system, which could be acquired only in one optical plane (Fig. 5.13b).

We analyzed the temporal distribution of lipo-ICG signal in different ROIs.The ROIs were selected based on 3D movies showing dynamic anatomical, vascular and perfusion properties.The study illustrates the heterogeneity of perfusion kinetics inside the tumor and contrast agent uptake after intravenous injection.In order to remove motion artefacts associated to breathing, a second order Butterworth low-pass filter was applied to the temporal profiles of the signals in each ROI, which were subsequently normalized to the maximum value. The analysis of multiple ROIs revealed three reproducible groups of temporal distribution profiles, the representative curves of which are displayed in Fig. 5.14. Group 1 demonstrated fast lipo-ICG increase shortly after injection and fast subsequent reduction to a plateau at approximately 1.5-fold enhancement from the pre-

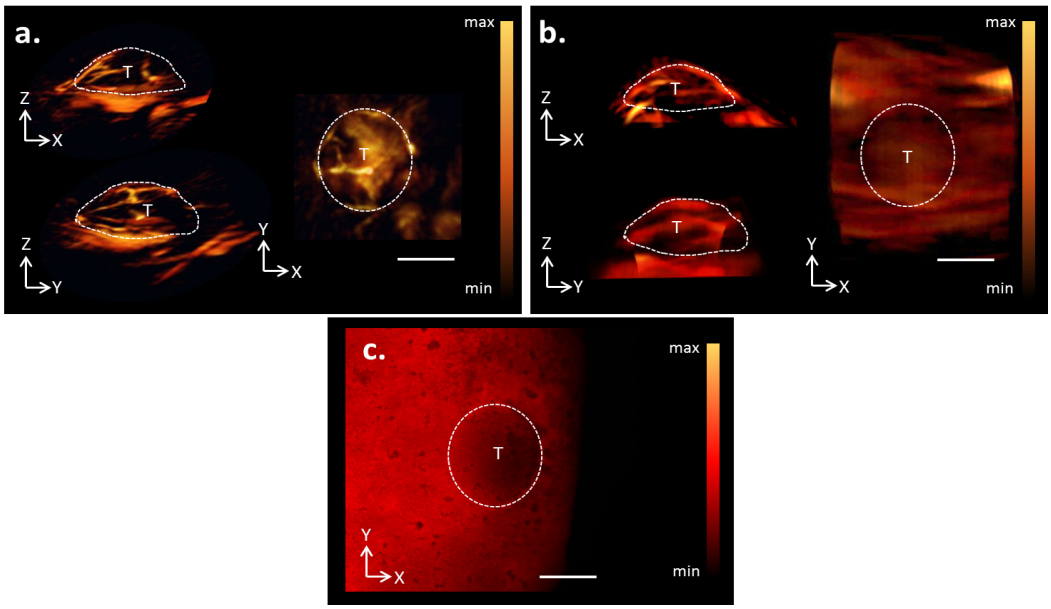

Figure 5.12: Performance of volumetric versus cross-sectional tumor imaging. (a) Maximum intensity projections of the reconstructions attained by the vMSOT system in different focal planes show high detail and isotropic resolution. (b) Corresponding images of the same area obtained by the cross-sectional 2D-MSOT imaging system suffer from rendering artifacts especially in z-direction. (we have to change the axis in the figure) Note that the x-y and y-z projections were rendered after processing the original multiple images acquired in the x-z plane. (c) Epi-fluorescence imaging of the same tumor. Dotted lines depict the tumor shapes in appropriate projections. Scale bar: 5 mm.

injection background signal level. Group 2 exhibited slower kinetics with significantly delayed peak signal enhancement at approximately 25 seconds post agent application and plateau level comparable to the peak values. Group 3 also showed delayed peak signal enhancement; however, the signal got slowly reduced to nearly the background level afterwards. The three lipo-ICG temporal profiles detected by real time vMSOT likely reflect perfusion in various vasculature types: healthy major blood vessels (Group 1), leaky vessels with slower perfusion kinetics (Group 2) and smaller blood vessels with lower throughput capacity (Group 3). The resulting 3D lipo-ICG distribution map was also summarized in 360° view.

Immediately after the real-time imaging at 800 nm, we acquired multispectral image sequences to accurately verify contrast agent location based on its unique spectral signature. Since the temporal distribution of lipo-ICG was highly dynamic, we standardized the multispectral imaging to be finished approximately 30 minutes upon the agent application. The main intrinsic contrast components contributing to the tissue absorption included oxygenated (HbO2) and deoxygenated (Hb) hemoblobin. They were visualized using the spectral unmixing procedure (Fig. 5.15) and also co-registered yielding the 3D map of in-vivo vasculature and blood oxygenation profiles in and around the tumor (Fig. 5.15a, b). Spectral unmixing also rendered the 3D map of lipo-ICG spatial distribution

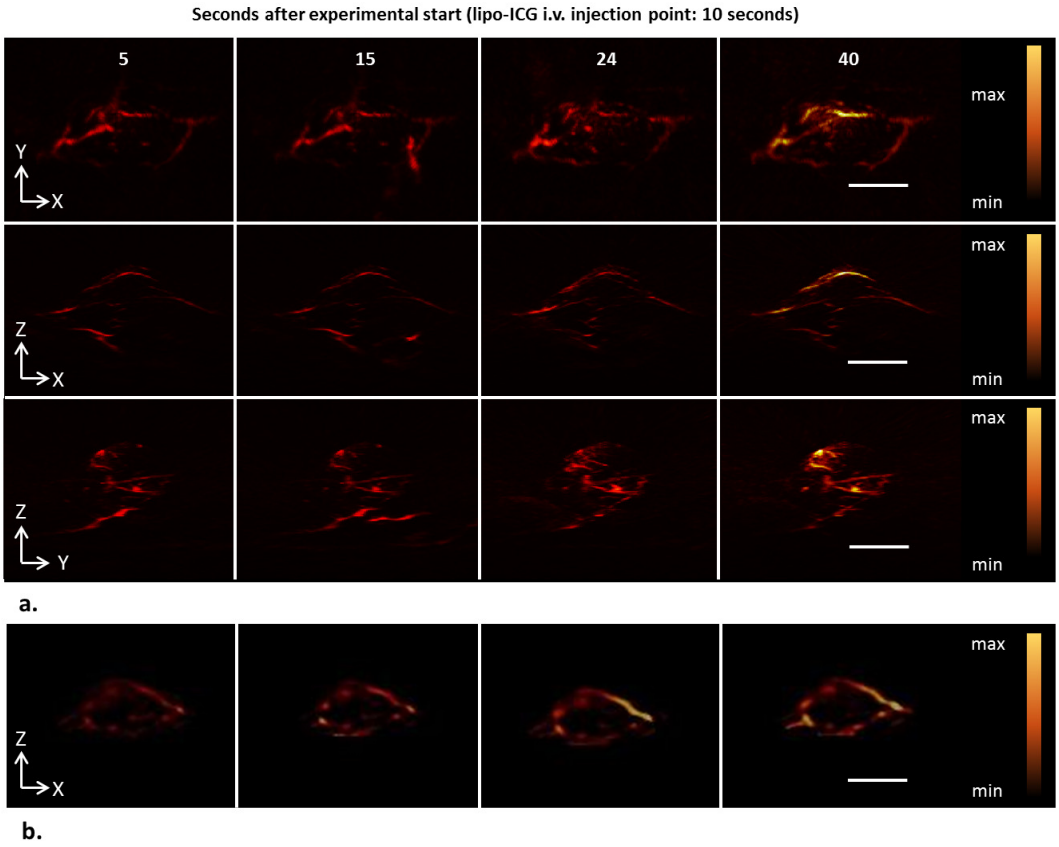

Figure 5.13: Comparison of real time imaging by vMSOT and 2D MSOT systems. (a) Maximal intensity projection (MIP) views in three dimensions showing the 800nm signal distribution at 5, 15, 24 and 40 seconds after start of the acquisition. Lipo-ICG application was done 10 seconds after imaging start. Note blood intrinsic contrast at 5 seconds vs. development of lipo-ICG signal at 15, 24 and 40 seconds (b) Imaging of tumor area at the same time points (5, 15, 24 and 40 seconds) during lipo-ICG application obtained by 2D MSOT. The tumor was manually segmented in these images. Scale bar: 5 mm. Color scales represent the corresponding chromophore concentrations in arbitrary units.

at given time point (Fig. 5.15d). Some Hb-rich areas readily recognized in the 3D map likely corresponded to the blood infiltrating the tumor mass due to leaky vessels, an observation that correlated well with the areas of diffuse lipo-ICG accumulation (Fig. 5.15c, f). In general, the specific lipo-ICG distribution profile rendered by the unmixing at 30 minutes upon application (Fig. 5.15d) correlated to both the HbO2 and Hb profiles showing that it was located in the blood vessels, but also started to extravasate into the tumor mass.

Lipo-ICG distribution and histological properties of tumors were imaged and analyzed post-mortem on the cryo-sections and validated against *in-vivo* OA maps (Fig. 5.15e). Both *in-vivo* and *ex-vivo* profiles in the sample tumor contained majority of the lipo-ICG fluorescence in the tumor periphery, which can be explained by the short time between

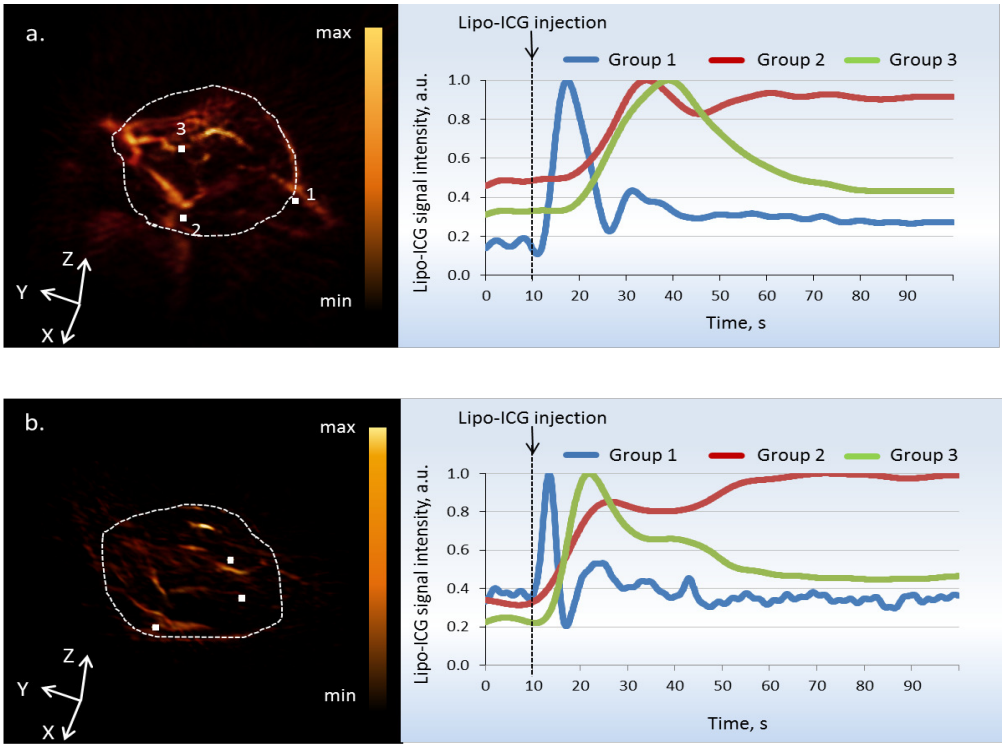

Figure 5.14: 3D view and analysis of lipo-ICG signal temporal distribution reveal 3 major groups of perfusion profiles in different tumors (a) and (b). Left panels: 3D images acquired 30 seconds after lipo-ICG application. The numbered squares show regions of interest (ROIs) representative for the major perfusion profile groups. Right panels: quantification graphs for the 3 groups of lipo-ICG temporal profiles. Lipo-ICG profiles likely reflect the perfusion rates in various types of vasculature: healthy major blood vessel (Group 1), leaky tumor vessel with poor perfusion kinetics (Group 2) and smaller blood vessel with increased resistance (Group 3). Color scale shows the intensity of the optoacoustic signal in arbitrary units.

lipo-ICG application and imaging. Since the animals were sacrificed and frozen immediately after the imaging experiment, frozen samples reflected the time point of imaging. vMSOT revealed most informative and detailed *in-vivo* lipo-ICG profile in the vasculature context in 3D (Fig. 5.15c,d) and in 2D (Fig. 5.15f). Hematoxylin-eosine staining confirmed the tumor shape and demonstrated histological properties of this region (Fig. 5.15e). The ex-vivo fluorescence profiles validated *in-vivo* data showing the areas of major lipo-ICG accumulation similar to the vMSOT-rendered profile (Fig 5.15d). It has to be noted that *ex-vivo* methods deliver the appropriate part of signal distribution for particular slice and time point. On the other hand, vMSOT allowed detection of lipo-ICG in the context of intrinsic blood contrast delivering more detailed information and longitudinal signal tracking along tumor vessel population in 3D. Overall, fluorescent (Fig. 5.15g) and histological validation with DAPI (Fig. 5.15h) of vMSOT data revealed good correlation between *in-vivo* and *ex-vivo* lipo-ICG profiles.

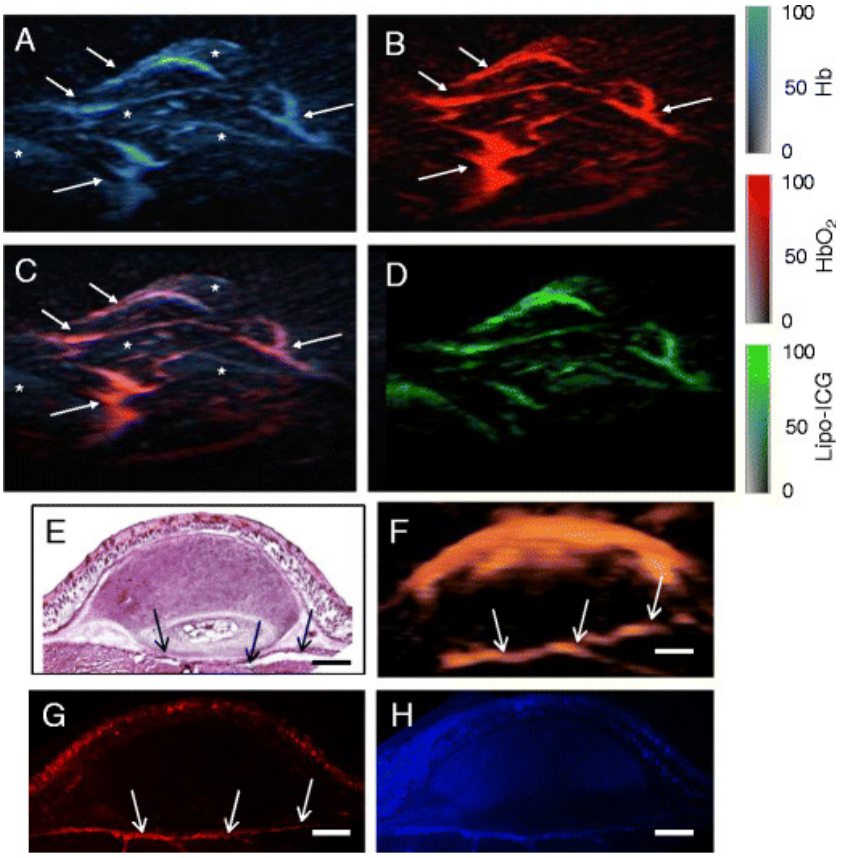

Figure 5.15: Imaging of in-vivo distribution of the intrinsic tissue chromophores and extrinsically administered contrast agent in the tumor 10 minutes post lipo-ICG injection. Spectrally-unmixed distribution of oxygenated (HbO2) and deoxygenated hemoglobin (Hb) are shown in (a) and (b), respectively. (c) The blood oxygenation profiles are represented by superimposition of the HbO2 and Hb maps. (d) Distribution of the lipo-ICG agent unmixed from the multispectral data. (a-d) Arrows point to major blood vessels. Asterisks define predominantly Hb-rich areas formed in part due to blood infiltration into the tumor mass through leaky vessels. Color scales represent the corresponding chromophore concentrations in arbitrary units. (e) Hematoxylin-eosin staining for tumor cryo-section. (f) A single 2D cross-section from the volumetric data acquired *in-vivo* by the vMSOT system from a tumor allograft after performing unmixing for the presence of lipo-ICG. (g) Fluorescence microscopy of lipo-ICG fluorescence. (h) Fluorescence microscopy of the same section stained with DAPI (cell nucleus marker used as a tissue control). Arrows (e, f, g): major blood vessels. Scale bar: 1 mm.

5.2.3 Discussion and conclusion

The study of tumor perfusion dynamics and hypoxia profiles is highly relevant for efficient therapy monitoring and development of new theranostic approaches, in both preclinical research and clinical practice. Indeed, hypoxic profiles influence metastatic potential and response to conventional irradiation and chemotherapy. We have further observed that inadequate perfusion withing tumor masses amplify pressure differences between

arterioles and venules, and increase the drug resistance [195]. Poor perfusion is one of the major factors leading to heterogeneous distribution of hypoxia regions within tumors [91]. In the present work, a new vMSOT method was applied for real-time 3D imaging and analysis of perfusion and blood oxygenation in a breast tumor mouse model *in-vivo*. The design configuration of vMSOT system (Fig. 5.9 and 5.10) offers key advantages over previously developed small-animal OA imaging systems [202, 204, 205]. As opposed to the approach of stacking the 2D images, vMSOT achieves a real-time deep-tissue imaging performance in three dimensions (10 volumes per second) using a tomographic configuration. The isotropic resolution of vMSOT (approximately 200μm in all three dimensions) enables imaging with superior accuracy and ability to analyze data in 3D. The anisotropic resolution of 2D-MSOT (800μm along the z direction vs. 150μm along the cross-section in the center of the image) strongly deteriorates the three-dimensional image quality. Thus, the study successfully demonstrate the vMSOT possesses novel qualities for studying tumor kinetics in 3D not achievable with other OA systems.
We imaged subcutaneous breast tumors with the use of lipo-ICG, a nanoparticle agent carrying a clinically-approved fluorescent and absorbing probe. Lipo-ICG was selected due to its favorable blood kinetics - it appears in the blood stream within seconds and retains for several hours. The enhanced retention enables efficient comparison between different imaging methods at various time scales upon single application of the probe [4]. vMSOT imaging during lipo-ICG injection yielded a time-lapse series of 3D images with great detail in all three (+ time) dimensions, which was not previously reported (Fig. 5.13). Rapid development of the lipo-ICG absorption signal within the first 30 seconds upon probe intravenous application was detected, initially in the major blood vessels and then in the rest of the tumor (Fig. 5.13). We quantitatively evaluated of multiple ROIs (in all tumors studied revealed the differential temporal development of the lipo-ICG signal as a perfusion marker (Fig. 5.14). It was noticed that the signal kinetics could be divided into three major classes based on their throughput. The first group (Fig. 5.14, Group 1) possibly represents major blood vessels outside the tumor, and has a fast appearance and disappearance of a sharp signal peak. The second group (Fig. 5.14, Group 2) shows a slower signal development and lipo-ICG arrest in the investigated area, it can be attributed as an example of perfusion dynamics expected in leaky tumor neovasculature. The third group (Fig. 5.14, Group 3) demonstrated slow signal enhancement and relaxation as compared to the first group, but no lipo-ICG retention, which possibly attributes it to smaller blood vessels. The vMSOT performance is enhanced by its capability for *in-vivo* assessment of high quality 3D maps of blood oxygenation in and around the tumors. Major vascular tracts constituting relatively large arteries and veins were efficiently resolved based on their oxygenation profiles. The areas outside larger blood vessels, predominantly containing deoxygenated hemoglobin components, have indicated presence of hypoxic regions mostly inside the tumor (Fig. 5.15a and 5.15b). The specific lipo-ICG map showed localization of the probe coinciding (Fig. 5.15c) with both the HbO2 and Hb profiles, so that at a given time point the great majority of the contrast agent was mainly in the blood vessels, but also started to extravasate into the tumor mass.
In conclusion, the newly developed vMSOT system enables use to study the pathophysi-

ological processes within microenvironment gradients of solid tumors by providing superior volumetric imaging performance with sustained competitive resolution and imaging depth suitable for investigations in preclinical cancer models. The approach is real-time (upto 100 fps) and suitable for 3D visualization of tumors, further it yields detailed high-resolution volumetric images in a living animal. The existing *in-vivo* imaging methods, such as dynamic contrast-enhanced CT [204], MRI [206] or ultrasound [207], lack the versatile contrast detection of vMSOT, have lower resolution and or do not possess the real-time 3D image rendering capacity. On the other hand, the limitations of vMSOT include the intrinsically restricted imaging penetration depth, which narrows the potential application portfolio. However, the possibility of using the vMSOT system in an handheld mode opens up the space for human vascular imaging [9]. Thus, we are optimistic that the technical advances and the clinical applications are readily translatable into a clinical setting.

6 Summary and future directions

6.1 Summary and contributions

The thesis consistes of two major components- development of algorithms and biomedical imaging applications. The Chapters 2-3 systemically illustrates and evaluates novel algorithms for visual quality enhancement of optoacoustic imaging ranging from image reconstruction and parameter optimization (Chapter 2), image analysis based quality enhancement methods (Chapter 3), to resolution improvement (Chapter 4). Chapter 5 demonstrates the applicability of the developed imaging protocols to pre-clinical and biomedical imaging.
The contributions of the thesis, as outlined earlier, can herein be summarized as follows:

- Development of algorithms for self-calibration of optoacoustic reconstruction parameters *including* but not limited to speed of sound estimation, and non-negative image reconstructions.
- Development of segmentation algorithms for optoacoustic imaging, and the application of segmented image prior(s) to improve visual image quality, viz. multiple speeds-of-sound mapping and optical fluence correction.
- Improving the resolution of OA images using 'pixel super-resolution' approach.
- Establishing multispectral optoacoustic tomography as an non-destruction imaging modality, with potential usage as an assisted reproductive technology.
- Investigation of the capabilities of dynamic (real-time), three-dimensional multispectral optoacoustics using v-MSOT, towards imaging of solid tumors in small animal models *in vivo*.

We have conducted in-depth experimentation for automated SoS fitting and segmentation of cross-sectional 2D images. Both phantom studies and animal imaging were conducted to develop and validate the algorithms developed. We conducted a separate study on segmentation of whole body small animal images with applications towards SoS mapping and optical fluence correction. In another independent study, we were able to use the intrinsic geometrical information and scanning capabilities of cross-sectional MSOT system(s) to achieve 'pixel super resolution,' and thus increase the resolution of the existing scanner, without hardware updates. The employed method uses information from different scanning location to overcome the limitations in resolutions caused due to size of pixels, and should not be confused with recent literature on super resolution with aim to break the diffraction limit of light or of acoustic waves.

We demonstrated MSOT as an effective tool for non-destructive evaluation of porcine ovarian follicle and explored the applicability of OA imaging pertaining to *in vitro* fertilization. We corroborated the findings and supplemented the studies with microscopic data (histopathology and SPIM imaging) and DNA defragmentation studies. Further, we have performed intravital imaging of whole breast cancer allografts in mice and compared the volumetric imaging performance with a standard cross-sectional MSOT system. The use of vMSOT enabled visualization of intrinsic contrast properties including blood oxygenation gradients along with spatial distribution of modified blood pool contrast agents to study vascularization, contrast agent penetration and extravasation in solid tumors. This study has been conducted in collaboration with biologists.
To the best of our knowledge, this is the first dissertation work which successfully brings together imaging physics, image reconstruction and image analysis methods for improving the quality and quantitativeness of OA imaging. The congregation of the diverse yet linked domains open up the door for achieving superior image quality and remarkable resolution, and push the boundaries of the present algorithms with minimal upgradation of hardware components. Additionally, the presented results on non-destructive nature of MSOT imaging establishes the claim of the method to be safe and opens new vistas in explorations in developmental and reproductive biology. Finally, we were able to demonstrate the unique capability of the vMSOT for imaging tumor microvasculature in five dimensions for the first time- obtaining there (spatial) dimensional temporal and spectral resolved visualization of solid tumors.

6.2 Future directions

The last couple of decades have seen rapid development of biomedical OA imaging with the evolution of state-of-the-art small animal imaging scanners and experimental clinical hand-held platforms. The technology has graduated from the from engineering laboratories to commercial products for pre-clinical imaging, and further into biomedical/translationalimaging platforms. So far the focus of development in OA imaging was largely focused on hardware improvement and solving the inverse problems. However, this dissertation introduces the applicability of image analysis to the current state-of-the-earth OA imaging instrumentation. The imaging physics - image analysis corroboration as illustrated in this thesis has lead to the development of new methods for quantitative inversion and parameter self-calibration, resolution enhancement, and accurate mapping of fluence and acoustic heterogeneities. This opens up the possibility of plethora of new developments, some of the suggestions are enlisted as following.

- Development of machine learning (ML) based algorithms for parameter estimation and image enhancement. ML based algorithms can be vastly be useful for improved reconstruction, identification and segmentation of organs and vascular structures.
- Use of multimodal priors (Ultrasound, MR, Xray CT) to improve the reconstruction performance and artifact reduction. More recently, there has been develop-

ment of hybrid optoacoustic- ultrasound (OPUS) systems, which has already made significant inroad in this direction [208, 209].

- Advanced methods in image segmentation including graph-cut and level-set based methods can be used to obtain more accurate boundary delineation even in images with limited view artifacts. Further, the present two compartment model can be extended to multi-compartment to improve quantitative imaging performance.

- We have used a FVM based model for fluence correction, there exist several other accurate models for correcting optical attenuations, viz. δ-Eddington approximation [210] and Monte-Carlo based methods which can be further investigated.

The applications of the OA imaging technology for *in vitro* fertilization techniques, and in oncological imaging further sheds light on the possibility of the following studies:

- Imaging of animals (and possibly of humans) *in vivo* using endoscopic or intra-urethal probes to study the ovaries, and conduct selection and intervention salvage of mature oocyctes. This can potentially revolutionize the field of artificial reproduction.

- Automated detection of tumor malignancy using ML algorithms from the perfusion dynamics, and vascular changes.

- Study treatment response on tumor masses by tracking deposition of targeted agent and hypoxia profiles.

Technologically, we have already been able to demonstrate the rendering of spectrally-resolved volumetric data in real time. State-of-the-art MSOT systems are able to accurately recover optical contrast at never-seen-before depths and speeds, and hence offer promise in a range of biomedical applications both in the research and clinics. Given the advancement of hardware capabilities we are now able to exploit the data processing limits using high-speed GPUs and to import the realm of advanced inversion models, post-processing and machine learning to the modality. Parallel to the technical developments, innovations have taken place in areas of biomarker design and detection – leading to newer applications. The five-dimensional imaging capability thus enables researchers to visualize diverse endogenous chromophores and administered contrast agents. Currently, MSOT is being widely used in areas of research including in-vivo cell tracking, molecular imaging studies, targeted molecular imaging, as well as functional imaging of the brain and heart. In spite of the vast progress, future work needs to be directed towards imaging at greater depths with enhanced accuracy and contrast, and development of image analysis and machine learning methods to suitably annotate the acquired data and enable clinical decision making using OA images.

Bibliography

[1] A. G. Bell, "Upon the production and reproduction of sound by light," *Journal of the Society of Telegraph Engineers*, vol. 9, pp. 404–426, 1880.

[2] D. Razansky, A. Buehler, and V. Ntziachristos, "Volumetric real-time multispectral optoacoustic tomography of biomarkers," *Nature protocols*, vol. 6, no. 8, pp. 1121–1129, 2011.

[3] X. Wang, Y. Pang, G. Ku, X. Xie, G. Stoica, and L. V. Wang, "Noninvasive laser-induced photoacoustic tomography for structural and functional in vivo imaging of the brain," *Nature biotechnology*, vol. 21, no. 7, pp. 803–806, 2003.

[4] D. Razansky, M. Distel, C. Vinegoni, R. Ma, N. Perrimon, R. W. Köster, and V. Ntziachristos, "Multispectral opto-acoustic tomography of deep-seated fluorescent proteins in vivo," *Nature Photonics*, vol. 3, no. 7, pp. 412–417, 2009.

[5] V. Ntziachristos, J. Ripoll, L. V. Wang, and R. Weissleder, "Looking and listening to light: the evolution of whole-body photonic imaging," *Nature biotechnology*, vol. 23, no. 3, pp. 313–320, 2005.

[6] S. Mandal, X. L. Dean-Ben, N. C. Burton, and D. Razansky, "Extending biological imaging to the fifth dimension: Evolution of volumetric small animal multispectral optoacoustic tomography.," *IEEE pulse*, vol. 6, no. 3, pp. 47–53, 2015.

[7] P. Beard, "Biomedical photoacoustic imaging," *Interface focus*, p. rsfs20110028, 2011.

[8] J. Xia and L. V. Wang, "Small-animal whole-body photoacoustic tomography: a review," *IEEE Transactions on Biomedical Engineering*, vol. 61, no. 5, pp. 1380–1389, 2014.

[9] X. Deán-Ben and D. Razansky, "Adding fifth dimension to optoacoustic imaging: volumetric time-resolved spectrally enriched tomography," *Light: Science & Applications*, vol. 3, no. 1, p. e137, 2014.

[10] L. V. Wang, *Photoacoustic imaging and spectroscopy*. CRC press, 2009.

[11] C. Hoelen and F. De Mul, "A new theoretical approach to photoacoustic signal generation," *The Journal of the Acoustical Society of America*, vol. 106, no. 2, pp. 695–706, 1999.

[12] Y. Fan, A. Mandelis, G. Spirou, and I. Alex Vitkin, "Development of a laser photothermoacoustic frequency-swept system for subsurface imaging: theory and experiment," *The Journal of the Acoustical Society of America*, vol. 116, no. 6, pp. 3523–3533, 2004.

[13] A. Miklos, Z. Bozoki, Y. Jiang, and M. Feher, "Experimental and theoretical investigation of photoacoustic-signal generation by wavelength-modulated diode lasers," *Applied Physics B: Lasers and Optics*, vol. 58, no. 6, pp. 483–492, 1994.

[14] D. Razansky, "Multispectral optoacoustic tomography volumetric color hearing in real time," *Selected Topics in Quantum Electronics, IEEE Journal of*, vol. 18, no. 3, pp. 1234–1243, 2012.

[15] A. Rosenthal, D. Razansky, and V. Ntziachristos, "Fast semi-analytical model-based acoustic inversion for quantitative optoacoustic tomography," *IEEE transactions on medical imaging*, vol. 29, no. 6, pp. 1275–1285, 2010.

[16] R. A. Kruger, P. Liu, Y. Fang, C. R. Appledorn, *et al.*, "Photoacoustic ultrasound (paus)—reconstruction tomography," *Medical physics*, vol. 22, no. 10, pp. 1605–1609, 1995.

[17] B. T. Cox, S. Kara, S. R. Arridge, and P. C. Beard, "k-space propagation models for acoustically heterogeneous media: Application to biomedical photoacoustics," *The Journal of the Acoustical Society of America*, vol. 121, no. 6, pp. 3453–3464, 2007.

[18] L. V. Wang and S. Hu, "Photoacoustic tomography: in vivo imaging from organelles to organs," *Science*, vol. 335, no. 6075, pp. 1458–1462, 2012.

[19] J. Laufer, P. Johnson, E. Zhang, B. Treeby, B. Cox, B. Pedley, and P. Beard, "In vivo preclinical photoacoustic imaging of tumor vasculature development and therapy," *Journal of biomedical optics*, vol. 17, no. 5, pp. 0560161–0560168, 2012.

[20] H.-P. Brecht, R. Su, M. Fronheiser, S. A. Ermilov, A. Conjusteau, and A. A. Oraevsky, "Whole-body three-dimensional optoacoustic tomography system for small animals," *Journal of biomedical optics*, vol. 14, no. 6, pp. 064007–064007, 2009.

[21] A. Buehler, X. L. Deán-Ben, J. Claussen, V. Ntziachristos, and D. Razansky, "Three-dimensional optoacoustic tomography at video rate," *Opt. Express*, vol. 20, pp. 22712–22719, Sep 2012.

[22] A. Buehler, E. Herzog, D. Razansky, and V. Ntziachristos, "Video rate optoacoustic tomography of mouse kidney perfusion," *Opt. Lett.*, vol. 35, pp. 2475–2477, Jul 2010.

[23] E. Herzog, A. Taruttis, N. Beziere, A. A. Lutich, D. Razansky, and V. Ntziachristos, "Optical imaging of cancer heterogeneity with multispectral optoacoustic tomography," *Radiology*, vol. 263, no. 2, pp. 461–468, 2012.

[24] X. L. Dean-Ben, A. Ozbek, and D. Razansky, "Volumetric real-time tracking of peripheral human vasculature with gpu-accelerated three-dimensional optoacoustic tomography," *IEEE transactions on medical imaging*, vol. 32, no. 11, pp. 2050–2055, 2013.

[25] A. Taruttis and V. Ntziachristos, "Advances in real-time multispectral optoacoustic imaging and its applications," *Nature Photonics*, vol. 9, no. 4, pp. 219–227, 2015.

[26] V. Ntziachristos and D. Razansky, "Molecular imaging by means of multispectral optoacoustic tomography (msot)," *Chemical reviews*, vol. 110, no. 5, pp. 2783–2794, 2010.

[27] J. Weber, P. C. Beard, and S. E. Bohndiek, "Contrast agents for molecular photoacoustic imaging," *Nature Methods*, vol. 13, no. 8, pp. 639–650, 2016.

[28] V. Ermolayev, X. L. Dean-Ben, S. Mandal, V. Ntziachristos, and D. Razansky, "Simultaneous visualization of tumour oxygenation, neovascularization and contrast agent perfusion by real-time three-dimensional optoacoustic tomography," *European radiology*, vol. 26, no. 6, pp. 1843–1851, 2016.

[29] D. A. Boas, C. Pitris, and N. Ramanujam, *Handbook of biomedical optics*. CRC press, 2011.

[30] X. L. Deán-Ben, E. Bay, and D. Razansky, "Functional optoacoustic imaging of moving objects using microsecond-delay acquisition of multispectral three-dimensional tomographic data," *Scientific reports*, vol. 4, p. 5878, 2014.

[31] X. L. Deán-Ben, S. J. Ford, and D. Razansky, "High-frame rate four dimensional optoacoustic tomography enables visualization of cardiovascular dynamics and mouse heart perfusion," *Scientific reports*, vol. 5, p. 10133, 2015.

[32] M.-L. Li, H. F. Zhang, K. Maslov, G. Stoica, and L. V. Wang, "Improved in vivo photoacoustic microscopy based on a virtual-detector concept," *Optics letters*, vol. 31, no. 4, pp. 474–476, 2006.

[33] R. Ma, M. Distel, X. L. Deán-Ben, V. Ntziachristos, and D. Razansky, "Non-invasive whole-body imaging of adult zebrafish with optoacoustic tomography," *Physics in Medicine and Biology*, vol. 57, no. 22, p. 7227, 2012.

[34] M. Xu and L. V. Wang, "Universal back-projection algorithm for photoacoustic computed tomography," *Physical Review E*, vol. 71, no. 1, p. 016706, 2005.

[35] K. P. Köstli, M. Frenz, H. Bebie, and H. P. Weber, "Temporal backward projection of optoacoustic pressure transients using fourier transform methods," *Physics in medicine and biology*, vol. 46, no. 7, p. 1863, 2001.

[36] X. Wang, Y. Xu, M. Xu, S. Yokoo, E. S. Fry, and L. V. Wang, "Photoacoustic tomography of biological tissues with high cross-section resolution: Reconstruction and experiment," *Medical physics*, vol. 29, no. 12, pp. 2799–2805, 2002.

[37] D. Razansky, N. J. Harlaar, J. L. Hillebrands, A. Taruttis, E. Herzog, C. J. Zeebregts, G. M. van Dam, and V. Ntziachristos, "Multispectral optoacoustic tomography of matrix metalloproteinase activity in vulnerable human carotid plaques," *Molecular imaging and biology*, vol. 14, no. 3, pp. 277–285, 2012.

[38] G. Paltauf, J. Viator, S. Prahl, and S. Jacques, "Iterative reconstruction algorithm for optoacoustic imaging," *The Journal of the Acoustical Society of America*, vol. 112, no. 4, pp. 1536–1544, 2002.

[39] G. T. Herman and A. Lent, "Iterative reconstruction algorithms," *Computers in biology and medicine*, vol. 6, no. 4, pp. 273–294, 1976.

[40] G. H. Golub and C. F. Van Loan, *Matrix computations*, vol. 3. JHU Press, 2012.

[41] C. C. Paige and M. A. Saunders, "Lsqr: An algorithm for sparse linear equations and sparse least squares," *ACM transactions on Mathematical Software*, vol. 8, no. 1, pp. 43–71, 1982.

[42] J. Zhang, M. A. Anastasio, P. J. La Rivière, and L. V. Wang, "Effects of different imaging models on least-squares image reconstruction accuracy in photoacoustic tomography," *IEEE Transactions on medical imaging*, vol. 28, no. 11, pp. 1781–1790, 2009.

[43] T. A., "Solution of incorrectly formulated problems and the regularization method," *Soviet Math. Dokl.*, vol. 5, pp. 1035–1038, 1963.

[44] P. Kuchment and L. Kunyansky, "Mathematics of photoacoustic and thermoacoustic tomography," in *Handbook of Mathematical Methods in Imaging*, pp. 817–865, Springer, 2011.

[45] B. E. Treeby, E. Z. Zhang, and B. T. Cox, "Photoacoustic tomography in absorbing acoustic media using time reversal," *Inverse Problems*, vol. 26, no. 11, p. 115003, 2010.

[46] A. Rosenthal, D. Razansky, and V. Ntziachristos, "Quantitative optoacoustic signal extraction using sparse signal representation," *IEEE transactions on medical imaging*, vol. 28, no. 12, pp. 1997–2006, 2009.

[47] C. Lutzweiler, S. Tzoumas, A. Rosenthal, V. Ntziachristos, and D. Razansky, "High-throughput sparsity-based inversion scheme for optoacoustic tomography," *IEEE transactions on medical imaging*, vol. 35, no. 2, pp. 674–684, 2016.

[48] C. Lutzweiler, X. L. Deán-Ben, and D. Razansky, "Expediting model-based optoacoustic reconstructions with tomographic symmetries," *Medical physics*, vol. 41, no. 1, 2014.

[49] H. Liu, K. Wang, D. Peng, H. Li, Y. Zhu, S. Zhang, M. Liu, and J. Tian, "Curve-driven-based acoustic inversion for photoacoustic tomography," *IEEE Transactions on Medical Imaging*, vol. 35, no. 12, pp. 2546–2557, 2016.

[50] G. Paltauf, J. A. Viator, S. A. Prahl, and S. L. Jacques, "Iterative reconstruction algorithm for optoacoustic imaging," *Journal of the Acoustical Society of America*, vol. 112, no. 4, pp. 1536–1544, 2002.

[51] J. Xia, M. R. Chatni, K. Maslov, Z. Guo, K. Wang, M. Anastasio, and L. V. Wang, "Whole-body ring-shaped confocal photoacoustic computed tomography of small animals in vivo," *Journal of biomedical optics*, vol. 17, no. 5, pp. 0505061–0505063, 2012.

[52] X. L. Deán-Ben, R. Ma, D. Razansky, and V. Ntziachristos, "Statistical approach for optoacoustic image reconstruction in the presence of strong acoustic heterogeneities," *IEEE Transactions on Medical Imaging*, vol. 30, no. 2, pp. 401–408, 2011.

[53] J. Jose, R. G. H. Willemink, S. Resink, D. Piras, J. C. G. van Hespen, C. H. Slump, W. Steenbergen, T. G. van Leeuwen, and S. Manohar, "Passive element enrichted photoacoustic computed tomography (PER PACT) for simultaneous imaging of acoustic propagation properties and light absorption," *Optics Express*, vol. 19, no. 3, pp. 2093–2104, 2011.

[54] X. L. Deán-Ben, A. Buehler, V. Ntziachristos, and D. Razansky, "Accurate model-based reconstruction algorithm for three-dimensional optoacoustic tomography," *IEEE Transactions on Medical Imaging*, vol. 31, no. 10, pp. 1922–1928, 2012.

[55] X. L. Deán-Ben, V. Ntziachristos, and D. Razansky, "Effects of small variations of speed of sound in optoacoustic tomographic imaging," *Medical physics*, vol. 41, no. 7, 2014.

[56] C. Huang, K. Wang, L. Nie, L. V. Wang, and M. A. Anastasio, "Full-wave iterative image reconstruction in photoacoustic tomography with acoustically inhomogeneous media," *IEEE transactions on medical imaging*, vol. 32, no. 6, pp. 1097–1110, 2013.

[57] J. Xia, C. Huang, K. Maslov, M. A. Anastasio, and L. V. Wang, "Enhancement of photoacoustic tomography by ultrasonic computed tomography based on optical excitation of elements of a full-ring transducer array," *Optics letters*, vol. 38, no. 16, pp. 3140–3143, 2013.

[58] D. Van de Sompel, L. S. Sasportas, A. Dragulescu-Andrasi, S. Bohndiek, and S. S. Gambhir, "Improving image quality by accounting for changes in water temperature during a photoacoustic tomography scan," *PLoS ONE*, vol. 7, p. e45337, 10 2012.

[59] W. Marczak, "Water as a standard in the measurements of speed of sound in liquids," *the Journal of the Acoustical Society of America*, vol. 102, no. 5, pp. 2776–2779, 1997.

[60] F. C. Groen, I. T. Young, and G. Ligthart, "A comparison of different focus functions for use in autofocus algorithms," *Cytometry*, vol. 6, no. 2, pp. 81–91, 1985.

[61] L. Firestone, K. Cook, K. Culp, N. Talsania, and K. Preston, "Comparison of autofocus methods for automated microscopy," *Cytometry*, vol. 12, no. 3, pp. 195–206, 1991.

[62] J. L. Pech-Pacheco, G. Cristóbal, J. Chamorro-Martinez, and J. Fernández-Valdivia, "Diatom autofocusing in brightfield microscopy: a comparative study," in *Pattern Recognition, 2000. Proceedings. 15th International Conference on*, vol. 3, pp. 314–317, IEEE, 2000.

[63] S. Pertuz, D. Puig, and M. A. Garcia, "Analysis of focus measure operators for shape-from-focus," *Pattern Recognition*, vol. 46, no. 5, pp. 1415–1432, 2013.

[64] A. Santos, C. Ortiz de Solórzano, J. J. Vaquero, J. Pena, N. Malpica, and F. Del Pozo, "Evaluation of autofocus functions in molecular cytogenetic analysis," *Journal of microscopy*, vol. 188, no. 3, pp. 264–272, 1997.

[65] B. E. Treeby, T. K. Varslot, E. Z. Zhang, J. G. Laufer, and P. C. Beard, "Automatic sound speed selection in photoacoustic image reconstruction using an autofocus approach," *Journal of biomedical optics*, vol. 16, no. 9, pp. 090501–090501, 2011.

[66] S. J. Orfanidis, *Introduction to signal processing*. Prentice-Hall, Inc., 1995.

[67] W. K. Pratt, J.-F. Abramatic, and O. Faugeras, "Method and apparatus for improved digital image processing," May 18 1982. US Patent 4,330,833.

[68] T. Yeo, S. Ong, R. Sinniah, *et al.*, "Autofocusing for tissue microscopy," *Image and vision computing*, vol. 11, no. 10, pp. 629–639, 1993.

[69] P. Perona and J. Malik, "Scale-space and edge detection using anisotropic diffusion," *Pattern Analysis and Machine Intelligence, IEEE Transactions on*, vol. 12, no. 7, pp. 629–639, 1990.

[70] Y. Yu and S. T. Acton, "Speckle reducing anisotropic diffusion," *IEEE Transactions on image processing*, vol. 11, no. 11, pp. 1260–1270, 2002.

[71] H. Garud, A. Ray, S. Mandal, D. Sheet, M. Mahadevappa, and J. Chatterjee, "Volume visualization approach for depth-of-field extension in digital pathology," in *Image and Signal Processing (CISP), 2011 4th International Congress on*, vol. 1, pp. 335–339, 2011.

[72] M. Subbarao, T.-S. Choi, and A. Nikzad, "Focusing techniques," *Optical Engineering*, vol. 32, no. 11, pp. 2824–2836, 1993.

[73] S. Ando, "Consistent gradient operators," *IEEE Transactions on Pattern Analysis and Machine Intelligence*, vol. 22, no. 3, pp. 252–265, 2000.

[74] B. E. Treeby, T. K. Varslot, E. Z. Zhang, J. G. Laufer, and P. C. Beard, "Automatic sound speed selection in photoacoustic image reconstruction using an autofocus approach," *Journal of Biomedical Optics*, vol. 16, no. 9, pp. 090501–090501–3, 2011.

[75] S. Mandal, E. Nasonova, X. Deán-Ben, and D. Razansky, "Fast calibration of speed-of-sound using temperature prior in whole-body small animal optoacoustic imaging," in *SPIE BiOS*, pp. 93232Q–93232Q, International Society for Optics and Photonics, 2015.

[76] A. Taruttis, A. Rosenthal, M. Kacprowicz, N. C. Burton, and V. Ntziachristos, "Multiscale multispectral optoacoustic tomography by a stationary wavelet transform prior to unmixing," *IEEE transactions on medical imaging*, vol. 33, no. 5, pp. 1194–1202, 2014.

[77] L. Ding, X. L. Deán-Ben, C. Lutzweiler, D. Razansky, and V. Ntziachristos, "Efficient non-negative constrained model-based inversion in optoacoustic tomography," *Physics in medicine and biology*, vol. 60, no. 17, p. 6733, 2015.

[78] S. Somayajula, C. Panagiotou, A. Rangarajan, Q. Li, S. R. Arridge, and R. M. Leahy, "Pet image reconstruction using information theoretic anatomical priors," *IEEE transactions on medical imaging*, vol. 30, no. 3, pp. 537–549, 2011.

[79] J. Tang and A. Rahmim, "Anatomy assisted pet image reconstruction incorporating multi-resolution joint entropy," *Physics in medicine and biology*, vol. 60, no. 1, p. 31, 2014.

[80] J. Skilling and R. Bryan, "Maximum entropy image reconstruction: general algorithm," *Monthly notices of the royal astronomical society*, vol. 211, no. 1, pp. 111–124, 1984.

[81] T. Tarvainen, A. Pulkkinen, B. T. Cox, J. P. Kaipio, and S. R. Arridge, "Bayesian image reconstruction in quantitative photoacoustic tomography," *IEEE transactions on medical imaging*, vol. 32, no. 12, pp. 2287–2298, 2013.

[82] R. Fletcher, "Practical optimization methods," *Wiley, New York*, 1987.

[83] C. E. Shannon, "A mathematical theory of communication," *ACM SIGMOBILE Mobile Computing and Communications Review*, vol. 5, no. 1, pp. 3–55, 2001.

[84] S. Tzoumas, N. Deliolanis, S. Morscher, and V. Ntziachristos, "Unmixing molecular agents from absorbing tissue in multispectral optoacoustic tomography," *IEEE transactions on medical imaging*, vol. 33, no. 1, pp. 48–60, 2014.

[85] N. Keshava and J. F. Mustard, "Spectral unmixing," *IEEE signal processing magazine*, vol. 19, no. 1, pp. 44–57, 2002.

[86] M. Xu and L. V. Wang, "Photoacoustic imaging in biomedicine," *Review of scientific instruments*, vol. 77, no. 4, p. 041101, 2006.

[87] S. Mandal, E. Nasonova, X. Deán-Ben, and D. Razansky, "Optimal self-calibration of tomographic reconstruction parameters in whole-body small animal optoacoustic imaging," *Photoacoustics*, vol. 2, no. 3, pp. 128 – 136, 2014.

[88] P. C. Hansen, *Rank-deficient and discrete ill-posed problems: numerical aspects of linear inversion*. SIAM, 1998.

[89] P. C. Hansen, "Regularization tools: A matlab package for analysis and solution of discrete ill-posed problems," *Numerical algorithms*, vol. 6, no. 1, pp. 1–35, 1994.

[90] S. R. Arridge and J. C. Schotland, "Optical tomography: forward and inverse problems," *arXiv*, vol. 123010, no. 25, p. 70, 2009.

[91] S. L. Jacques, "Optical properties of biological tissues: a review," *Physics in medicine and biology*, vol. 58, no. 11, p. R37, 2013.

[92] T. Jetzfellner, D. Razansky, A. Rosenthal, R. Schulz, K.-H. Englmeier, and V. Ntziachristos, "Performance of iterative optoacoustic tomography with experimental data," *Applied Physics Letters*, vol. 95, no. 1, p. 013703, 2009.

[93] S. Mandal, X. L. Deán-Ben, and D. Razansky, "Visual quality enhancement in optoacoustic tomography using active contour segmentation priors," *IEEE Transactions on Medical Imaging*, vol. 35, pp. 2209–2217, Oct 2016.

[94] J. A. Noble and D. Boukerroui, "Ultrasound image segmentation: a survey," *IEEE Transactions on medical imaging*, vol. 25, no. 8, pp. 987–1010, 2006.

[95] R. B. Schulz, A. Ale, A. Sarantopoulos, M. Freyer, E. Soehngen, M. Zientkowska, and V. Ntziachristos, "Hybrid system for simultaneous fluorescence and x-ray computed tomography," *IEEE transactions on medical imaging*, vol. 29, no. 2, pp. 465–473, 2010.

[96] V. Schulz, I. Torres-Espallardo, S. Renisch, Z. Hu, N. Ojha, P. Börnert, M. Perkuhn, T. Niendorf, W. Schäfer, H. Brockmann, *et al.*, "Automatic, three-segment, mr-based attenuation correction for whole-body pet/mr data," *European journal of nuclear medicine and molecular imaging*, vol. 38, no. 1, pp. 138–152, 2011.

[97] M. Schweiger and S. Arridge, "Optical tomographic reconstruction in a complex head model using a priori region boundary information," *Physics in medicine and biology*, vol. 44, no. 11, p. 2703, 1999.

[98] X. L. Deán-Ben, R. Ma, A. Rosenthal, V. Ntziachristos, and D. Razansky, "Weighted model-based optoacoustic reconstruction in acoustic scattering media," *Physics in medicine and biology*, vol. 58, no. 16, p. 5555, 2013.

[99] M. S. Singh and P. K. Yalavarthy, "Born-ratio type data normalization improves quantitation in photoacoustic tomography," in *SPIE Medical Imaging*, pp. 90401T–90401T, International Society for Optics and Photonics, 2014.

[100] T. Jetzfellner, A. Rosenthal, A. Buehler, K.-H. Englmeier, D. Razansky, and V. Ntziachristos, "Multispectral optoacoustic tomography by means of normalized spectral ratio," *Optics letters*, vol. 36, no. 21, pp. 4176–4178, 2011.

[101] X. L. Deán-Ben, V. Ntziachristos, and D. Razansky, "Statistical optoacoustic image reconstruction using a-priori knowledge on the location of acoustic distortions," *Applied Physics Letters*, vol. 98, no. 17, p. 171110, 2011.

[102] M. Kass, A. Witkin, and D. Terzopoulos, "Snakes: Active contour models," *International journal of computer vision*, vol. 1, no. 4, pp. 321–331, 1988.

[103] R. Delgado-Gonzalo, V. Uhlmann, D. Schmitter, and M. Unser, "Snakes on a plane: A perfect snap for bioimage analysis.," *IEEE Signal Process. Mag.*, vol. 32, no. 1, pp. 41–48, 2015.

[104] B. Sumengen and B. Manjunath, "Multi-scale edge detection and image segmentation," in *European signal processing conference (EUSIPCO)*, Citeseer, 2005.

[105] J. Canny, "A computational approach to edge detection," *Pattern Analysis and Machine Intelligence, IEEE Transactions on*, no. 6, pp. 679–698, 1986.

[106] M. Tabb and N. Ahuja, "Multiscale image segmentation by integrated edge and region detection," *Image Processing, IEEE Transactions on*, vol. 6, no. 5, pp. 642–655, 1997.

[107] W. Ma and B. Manjunath, "Edgeflow: a technique for boundary detection and image segmentation," *Image Processing, IEEE Transactions on*, vol. 9, no. 8, pp. 1375–1388, 2000.

[108] F. Bergholm, "Edge focusing," *IEEE Transactions on Pattern Analysis and Machine Intelligence*, vol. 9, no. 6, pp. 726–741, 1987.

[109] M. Lynch, O. Ghita, and P. Whelan, "Segmentation of the left ventricle of the heart in 3-d+ t mri data using an optimized nonrigid temporal model," *Medical Imaging, IEEE Transactions on*, vol. 27, no. 2, pp. 195–203, 2008.

[110] T. McInerney and D. Terzopoulos, "Deformable models in medical image analysis: a survey," *Medical image analysis*, vol. 1, no. 2, pp. 91–108, 1996.

[111] H. Biilthoff, J. Little, and T. Poggio, "A parallel algorithm for real-time computation of optical flow," *Nature*, vol. 337, no. 6207, pp. 549–553, 1989.

[112] R. C. Gonzalez and R. E. Woods, "Image processing," *Digital image processing*, vol. 2, 2007.

[113] T. F. Chan and L. A. Vese, "Active contours without edges," *IEEE Transactions on image processing*, vol. 10, no. 2, pp. 266–277, 2001.

[114] S. Lankton and A. Tannenbaum, "Localizing region-based active contours," *IEEE transactions on image processing*, vol. 17, no. 11, pp. 2029–2039, 2008.

[115] V. Caselles, R. Kimmel, and G. Sapiro, "Geodesic active contours," *International journal of computer vision*, vol. 22, no. 1, pp. 61–79, 1997.

[116] B. E. Treeby and B. T. Cox, "k-wave: Matlab toolbox for the simulation and reconstruction of photoacoustic wave fields," *Journal of biomedical optics*, vol. 15, no. 2, pp. 021314–021314, 2010.

[117] R. Kimmel, *Numerical geometry of images: Theory, algorithms, and applications*. Springer Science & Business Media, 2012.

[118] L. R. . Dice, "Measures of the Amount of Ecologic Association Between Species," *Ecology*, vol. 26, no. 3, pp. 297–302, 1945.

[119] L. Wang, S. L. Jacques, and L. Zheng, "Mcml—monte carlo modeling of light transport in multi-layered tissues," *Computer methods and programs in biomedicine*, vol. 47, no. 2, pp. 131–146, 1995.

[120] B. T. Cox, S. R. Arridge, K. P. Köstli, and P. C. Beard, "Two-dimensional quantitative photoacoustic image reconstruction of absorption distributions in scattering media by use of a simple iterative method," *Applied Optics*, vol. 45, no. 8, pp. 1866–1875, 2006.

[121] T. Harrison, P. Shao, and R. J. Zemp, "A least-squares fixed-point iterative algorithm for multiple illumination photoacoustic tomography," *Biomedical optics express*, vol. 4, no. 10, pp. 2224–2230, 2013.

[122] X. L. Deán-Ben, A. Buehler, D. Razansky, and V. Ntziachristos, "Estimation of optoacoustic contrast agent concentration with self-calibration blind logarithmic unmixing," *Physics in medicine and biology*, vol. 59, no. 17, p. 4785, 2014.

[123] X. L. Deán-Ben, A. C. Stiel, Y. Jiang, V. Ntziachristos, G. G. Westmeyer, and D. Razansky, "Light fluence normalization in turbid tissues via temporally unmixed multispectral optoacoustic tomography," *Optics letters*, vol. 40, no. 20, pp. 4691–4694, 2015.

[124] A. Kienle and M. S. Patterson, "Improved solutions of the steady-state and the time-resolved diffusion equations for reflectance from a semi-infinite turbid medium," *JOSA A*, vol. 14, no. 1, pp. 246–254, 1997.

[125] M. Schweiger, S. Arridge, M. Hiraoka, and D. Delpy, "The finite element method for the propagation of light in scattering media: boundary and source conditions," *Medical physics*, vol. 22, no. 11, pp. 1779–1792, 1995.

[126] W. Bangerth, R. Hartmann, and G. Kanschat, "deal.II — a General Purpose Object Oriented Finite Element Library," *ACM Trans. Math. Softw.*, vol. 33, no. 4, p. 24, 2007.

[127] S. Mandal, P. Viswanath, N. Yeshaswini, X. L. Dean-Ben, and D. Razansky, "Multiscale edge detection and parametric shape modeling for boundary delineation in optoacoustic images," in *Engineering in Medicine and Biology Society (EMBC), 2015 37th Annual International Conference of the IEEE*, pp. 707–710, IEEE, 2015.

[128] S. L. Jacques, "Coupling 3d monte carlo light transport in optically heterogeneous tissues to photoacoustic signal generation," *Photoacoustics*, vol. 2, no. 4, pp. 137–142, 2014.

[129] S. Zackrisson, S. van de Ven, and S. Gambhir, "Light in and sound out: emerging translational strategies for photoacoustic imaging," *Cancer research*, vol. 74, no. 4, pp. 979–1004, 2014.

[130] W. Song, Z. Tang, D. Zhang, N. Burton, W. Driessen, and X. Chen, "Comprehensive studies of pharmacokinetics and biodistribution of indocyanine green and liposomal indocyanine green by multispectral optoacoustic tomography," *RSC Advances*, vol. 5, no. 5, pp. 3807–3813, 2015.

[131] I. Stoffels, S. Morscher, I. Helfrich, U. Hillen, J. Leyh, N. C. Burton, T. C. Sardella, J. Claussen, T. D. Poeppel, H. S. Bachmann, *et al.*, "Metastatic status of sentinel lymph nodes in melanoma determined noninvasively with multispectral optoacoustic imaging," *Science Translational Medicine*, vol. 7, no. 317, pp. 317ra199–317ra199, 2015.

[132] M. Xu, Y. Xu, and L. V. Wang, "Time-domain reconstruction algorithms and numerical simulations for thermoacoustic tomography in various geometries," *IEEE Transactions on biomedical engineering*, vol. 50, no. 9, pp. 1086–1099, 2003.

[133] A. Rosenthal, V. Ntziachristos, and D. Razansky, "Acoustic inversion in optoacoustic tomography: A review," *Current medical imaging reviews*, vol. 9, no. 4, pp. 318–336, 2013.

[134] T. L. Szabo, *Diagnostic Ultrasound Imaging: Inside Out.* San Diego (USA): Elsevier Academic Press, 2004.

[135] X. L. Deán-Ben, D. Razansky, and V. Ntziachristos, "The effects of acoustic attenuation in optoacoustic signals," *Physics in Medicine and Biology*, vol. 56, no. 18, pp. 6129–6148, 2011.

[136] Y. Xu and L. V. Wang, "Effects of acoustic heterogeneity in breast thermoacoustic tomography," *IEEE Transactions on ultrasonics, ferroelectrics and frequency control*, vol. 50, no. 9, pp. 1134–1146, 2003.

[137] A. Rosenthal, V. Ntziachristos, and D. Razansky, "Model-based optoacoustic inversion with arbitrary-shape detectors," *Medical physics*, vol. 38, no. 7, pp. 4285–4295, 2011.

[138] D. Queirós, X. L. Déan-Ben, A. Buehler, D. Razansky, A. Rosenthal, and V. Ntziachristos, "Modeling the shape of cylindrically focused transducers in three-dimensional optoacoustic tomography," *Journal of biomedical optics*, vol. 18, no. 7, pp. 076014–076014, 2013.

[139] A. Dima, N. C. Burton, and V. Ntziachristos, "Multispectral optoacoustic tomography at 64, 128, and 256 channels.," *Journal of biomedical optics*, vol. 19, p. 36021, mar 2014.

[140] Y. Hristova, P. Kuchment, and L. Nguyen, "Reconstruction and time reversal in thermoacoustic tomography in acoustically homogeneous and inhomogeneous media," *Inverse Problems*, vol. 24, no. 5, p. 055006, 2008.

[141] B. R. Hunt, "Super-resolution of images: Algorithms, principles, performance," *International Journal of Imaging Systems and Technology*, vol. 6, pp. 297–304, 1995.

[142] M. Irani and S. Peleg, "Improving resolution by image registration," *CVGIP: Graphical models and image processing*, 1991.

[143] M. Kang and S. Chaudhuri, "Super-resolution image reconstruction," *Signal Processing Magazine, IEEE*, pp. 21–36, 2003.

[144] J. Kennedy and O. Israel, "Super-resolution in PET imaging," *Medical Imaging, ...*, vol. 25, no. 2, pp. 137–147, 2006.

[145] E. Betzig, G. H. Patterson, R. Sougrat, O. W. Lindwasser, S. Olenych, J. S. Bonifacino, M. W. Davidson, J. Lippincott-Schwartz, and H. F. Hess, "Imaging intracellular fluorescent proteins at nanometer resolution.," *Science (New York, N.Y.)*, vol. 313, pp. 1642–5, sep 2006.

[146] K. Christensen-Jeffries, R. J. Browning, M.-X. Tang, C. Dunsby, R. J. Eckersley, S. S. Member, R. J. Browning, M.-X. Tang, C. Dunsby, R. J. Eckersley, and S. S. Member, "In Vivo Acoustic Super-Resolution and Super-Resolved Velocity Mapping Using Microbubbles.," *IEEE transactions on medical imaging*, vol. 0062, pp. 433–440, sep 2014.

[147] S. C. Park, M. K. Park, and M. G. Kang, "Super-resolution image reconstruction: a technical overview," *IEEE signal processing magazine*, vol. 20, no. 3, pp. 21–36, 2003.

[148] A. Gholipour, J. A. Estroff, and S. K. Warfield, "Robust super-resolution volume reconstruction from slice acquisitions: application to fetal brain mri," *IEEE transactions on Medical Imaging*, vol. 29, no. 10, pp. 1739–1758, 2010.

[149] R. Z. Shilling, T. Q. Robbie, T. Bailloeul, K. Mewes, R. M. Mersereau, and M. E. Brummer, "A super-resolution framework for 3-d high-resolution and high-contrast imaging using 2-d multislice mri," *IEEE Transactions on Medical Imaging*, vol. 28, no. 5, pp. 633–644, 2009.

[150] G. Wang, M. W. Vannier, M. W. Skinner, M. G. Cavalcanti, and G. W. Harding, "Spiral ct image deblurring for cochlear implantation," *IEEE transactions on medical imaging*, vol. 17, no. 2, pp. 251–262, 1998.

[151] E. Plenge, D. H. Poot, M. Bernsen, G. Kotek, G. Houston, P. Wielopolski, L. van der Weerd, W. J. Niessen, and E. Meijering, "Super-resolution methods in mri: Can they improve the trade-off between resolution, signal-to-noise ratio, and acquisition time?," *Magnetic resonance in medicine*, vol. 68, no. 6, pp. 1983–1993, 2012.

[152] M. D. Robinson, S. J. Chiu, J. Lo, C. Toth, J. Izatt, and S. Farsiu, "New applications of super-resolution in medical imaging," *Super-Resolution Imaging*, vol. 2010, pp. 384–412, 2010.

[153] E. Betzig, S. W. Hell, and W. E. Moerner, "The nobel prize in chemistry 2014," *Nobel Media AB*, 2014.

[154] H. Greenspan, "Super-Resolution in Medical Imaging," *The Computer Journal*, vol. 52, pp. 43–63, feb 2008.

[155] U. Mudenagudi, S. Banerjee, and P. K. Kalra, "Space-time super-resolution using graph-cut optimization," *IEEE Transactions on Pattern Analysis and Machine Intelligence*, vol. 33, no. 5, pp. 995–1008, 2011.

[156] J. Yang, J. Wright, T. S. Huang, and Y. Ma, "Image super-resolution via sparse representation.," *IEEE transactions on image processing : a publication of the IEEE Signal Processing Society*, vol. 19, pp. 2861–73, nov 2010.

[157] P. Cheeseman, B. Kanefsky, R. Kraft, J. Stutz, and R. Hanson, "Super-resolved surface reconstruction from multiple images," in *Maximum Entropy and Bayesian Methods*, pp. 293–308, Springer, 1996.

[158] A. Buehler, X. L. Dean-Ben, D. Razansky, and V. Ntziachristos, "Volumetric optoacoustic imaging with multi-bandwidth deconvolution," *IEEE transactions on medical imaging*, vol. 33, no. 4, pp. 814–821, 2014.

[159] P. K. Upputuri, Z.-B. Wen, Z. Wu, and M. Pramanik, "Super-resolution photoacoustic microscopy using photonic nanojets: a simulation study," *Journal of Biomedical Optics*, vol. 19, p. 116003, 2014.

[160] O. M. Viessmann, R. J. Eckersley, K. Christensen-Jeffries, M. X. Tang, and C. Dunsby, "Acoustic super-resolution with ultrasound and microbubbles.," *Physics in medicine and biology*, vol. 58, pp. 6447–58, sep 2013.

[161] J. Vogel, T. Lasser, J. Gardiazabal, and N. Navab, "Trajectory optimization for intra-operative nuclear tomographic imaging," *Medical Image Analysis*, vol. 17, no. 7, pp. 723–731, 2013.

[162] S. Farsiu, M. D. Robinson, M. Elad, and P. Milanfar, "Fast and robust multiframe super resolution," *IEEE transactions on image processing*, vol. 13, no. 10, pp. 1327–1344, 2004.

[163] A. Rueda, N. Malpica, and E. Romero, "Single-image super-resolution of brain mr images using overcomplete dictionaries," *Medical image analysis*, vol. 17, no. 1, pp. 113–132, 2013.

[164] H. He, K. He, and G. Zou, "A lorentzian stochastic estimation for video super resolution with lorentzian gradient constraint," *IEEE Transactions on Consumer Electronics*, vol. 58, pp. 1294–1300, nov 2012.

[165] F. Zhou, W. Yang, and Q. Liao, "A coarse-to-fine subpixel registration method to recover local perspective deformation in the application of image super-resolution," *IEEE Transactions on Image Processing*, vol. 21, no. 1, pp. 53–66, 2012.

[166] E. Shechtman, Y. Caspi, and M. Irani, "Space-time super-resolution," *IEEE Transactions on Pattern Analysis and Machine Intelligence*, vol. 27, no. 4, pp. 531–545, 2005.

[167] W. Luo, Y. Zhang, A. Feizi, Z. Göröcs, and A. Ozcan, "Pixel super-resolution using wavelength scanning," *Light: Science & Applications*, vol. 5, no. 4, p. e16060, 2015.

[168] X. L. Deán-Ben and D. Razansky, "Portable spherical array probe for volumetric real-time optoacoustic imaging at centimeter-scale depths," *Optics express*, vol. 21, no. 23, pp. 28062–28071, 2013.

[169] C. L. Shehan, *The Wiley Blackwell Encyclopedia of Family Studies, 4 Volume Set*, vol. 4. John Wiley & Sons, 2016.

[170] G. Gunarathne, "Breaking through the speed barrier—advancements in high-speed imaging," in *Advancements and Breakthroughs in Ultrasound Imaging*, InTech, 2013.

[171] A. Krivanek and M. Sonka, "Ovarian ultrasound image analysis: Follicle segmentation," *IEEE transactions on medical imaging*, vol. 17, no. 6, pp. 935–944, 1998.

[172] H. Zheng, X.-L. Chen, C.-Q. Zhu, D.-H. Li, Q.-Y. Chen, and J.-G. Xu, "Brilliant cresyl blue as a new red region fluorescent probe for determination of nucleic acids," *Microchemical journal*, vol. 64, no. 3, pp. 263–269, 2000.

[173] J. Ripoll, B. Koberstein-Schwarz, and V. Ntziachristos, "Unleashing optics and optoacoustics for developmental biology," *Trends in biotechnology*, vol. 33, no. 11, pp. 679–691, 2015.

[174] G. R. Pereira, P. L. Lorenzo, G. F. Carneiro, S. Bilodeau-Goeseels, J. P. Kastelic, A. Esteller-Vico, M. Lopez-Bejar, and I. K. Liu, "Selection of developmentally competent immature equine oocytes with brilliant cresyl blue stain prior to in vitro maturation with equine growth hormone," *Zygote*, vol. 22, no. 04, pp. 500–504, 2014.

[175] B. Manjunatha, P. Gupta, M. Devaraj, J. Ravindra, and S. Nandi, "Selection of developmentally competent buffalo oocytes by brilliant cresyl blue staining before ivm," *Theriogenology*, vol. 68, no. 9, pp. 1299–1304, 2007.

[176] L. Katska-Ksiazkiewicz, J. Opiela, and B. Rynska, "Effects of oocyte quality, semen donor and embryo co-culture system on the efficiency of blastocyst production in goats," *Theriogenology*, vol. 68, no. 5, pp. 736–744, 2007.

[177] J. Su, Y. Wang, R. Li, H. Peng, S. Hua, Q. Li, F. Quan, Z. Guo, and Y. Zhang, "Oocytes selected using bcb staining enhance nuclear reprogramming and the in vivo development of scnt embryos in cattle," *PloS one*, vol. 7, no. 4, p. e36181, 2012.

[178] R. C. Stanton, "Glucose-6-phosphate dehydrogenase, nadph, and cell survival," *IUBMB life*, vol. 64, no. 5, pp. 362–369, 2012.

[179] J. M. Nascimento and J. M. Dias, "Vertex component analysis: A fast algorithm to unmix hyperspectral data," *IEEE transactions on Geoscience and Remote Sensing*, vol. 43, no. 4, pp. 898–910, 2005.

[180] X. L. Deán-Ben, N. C. Deliolanis, V. Ntziachristos, and D. Razansky, "Fast unmixing of multispectral optoacoustic data with vertex component analysis," *Optics and Lasers in Engineering*, vol. 58, pp. 119–125, 2014.

[181] P. Viswanath, T. Weiser, P. Chintala, S. Mandal, and R. Dutta, "Grading of mammalian cumulus oocyte complexes using machine learning for in vitro embryo culture," in *Biomedical and Health Informatics (BHI), 2016 IEEE-EMBS International Conference on*, pp. 172–175, IEEE, 2016.

[182] H. He, S. Mandal, A. Buehler, X. L. Deán-Ben, D. Razansky, and V. Ntziachristos, "Improving optoacoustic image quality via geometric pixel super-resolution approach," *IEEE transactions on medical imaging*, vol. 35, no. 3, pp. 812–818, 2016.

[183] H.-C. A. Lin, R. Dutta, S. Mandal, A. Kind, A. Schnieke, and D. Razansky, "Advancing ovarian folliculometry with selective plane illumination microscopy," *Scientific Reports*, vol. 6, 2016.

[184] J. Griffin, B. R. Emery, I. Huang, C. M. Peterson, and D. T. Carrell, "Comparative analysis of follicle morphology and oocyte diameter in four mammalian species (mouse, hamster, pig, and human)," *Journal of Experimental & Clinical Assisted Reproduction*, vol. 3, no. 1, p. 2, 2006.

[185] L. Pfeifer, L. Siqueira, G. Adams, R. Pierson, and J. Singh, "In vivo imaging of cumulus-oocyte-complexes and small ovarian follicles in cattle using ultrasonic biomicroscopy," *Animal reproduction science*, vol. 131, no. 1, pp. 88–94, 2012.

[186] E. Rodrıguez-González, M. Lopez-Bejar, E. Velilla, and M. Paramio, "Selection of prepubertal goat oocytes using the brilliant cresyl blue test," *Theriogenology*, vol. 57, no. 5, pp. 1397–1409, 2002.

[187] M. Pujol, M. López-Béjar, and M.-T. Paramio, "Developmental competence of heifer oocytes selected using the brilliant cresyl blue (bcb) test," *Theriogenology*, vol. 61, no. 4, pp. 735–744, 2004.

[188] V. Chandrakanthan, A. Li, O. Chami, and C. O'Neill, "Effects of in vitro fertilization and embryo culture on trp53 and bax expression in b6 mouse embryos," *Reproductive Biology and Endocrinology*, vol. 4, no. 1, p. 61, 2006.

[189] Y. Morita and J. L. Tilly, "Oocyte apoptosis: like sand through an hourglass," *Developmental biology*, vol. 213, no. 1, pp. 1–17, 1999.

[190] R. Dutta, S. Li, K. Fischer, A. Kind, T. Flisikowska, K. Flisikowski, O. Rottmann, and A. Schnieke, "Non-invasive assessment of porcine oocyte quality by supravital staining of cumulus–oocyte complexes with lissamine green b," *Zygote*, vol. 24, no. 03, pp. 418–427, 2016.

[191] J. Van Blerkom, "The influence of intrinsic and extrinsic factors on the developmental potential and chromosomal normality of the human oocyte," *Journal of the Society for Gynecologic Investigation*, vol. 3, no. 1, pp. 3–11, 1996.

[192] J. Kwee, M. E. Elting, R. Schats, J. McDonnell, and C. B. Lambalk, "Ovarian volume and antral follicle count for the prediction of low and hyper responders with in vitro fertilization," *Reproductive Biology and Endocrinology*, vol. 5, no. 1, p. 9, 2007.

[193] L. A. Torre, F. Bray, R. L. Siegel, J. Ferlay, J. Lortet-Tieulent, and A. Jemal, "Global cancer statistics, 2012," *CA: a cancer journal for clinicians*, vol. 65, no. 2, pp. 87–108, 2015.

[194] A. Wojnar, B. Pula, M. Podhorska-Okolow, and P. Dzikegiel, "Discrepancies between her2 assessment from core needle biopsies and surgical specimens of invasive ductal breast carcinoma," *Adv Clin Exp Med*, vol. 22, pp. 27–31, 2013.

[195] O. Trédan, C. M. Galmarini, K. Patel, and I. F. Tannock, "Drug resistance and the solid tumor microenvironment," *Journal of the National Cancer Institute*, vol. 99, no. 19, pp. 1441–1454, 2007.

[196] F. C. Galmarini, C. M. Galmarini, M. I. Sarchi, J. Abulafia, and D. Galmarini, "Heterogeneous distribution of tumor blood supply affects the response to chemotherapy in patients with head and neck cancer," *Microcirculation*, vol. 7, no. 6, pp. 405–410, 2000.

[197] C. Alberti, "From molecular imaging in preclinical/clinical oncology to theranostic applications in targeted tumor therapy," *Eur Rev Med Pharmacol Sci*, vol. 16, no. 14, pp. 1925–1933, 2012.

[198] A. Ale, V. Ermolayev, E. Herzog, C. Cohrs, M. H. De Angelis, and V. Ntziachristos, "Fmt-xct: in vivo animal studies with hybrid fluorescence molecular tomography-x-ray computed tomography," *Nature methods*, vol. 9, no. 6, pp. 615–620, 2012.

[199] H. S. Alshetaiwi, S. Balivada, T. B. Shrestha, M. Pyle, M. T. Basel, S. H. Bossmann, and D. L. Troyer, "Luminol-based bioluminescence imaging of mouse mammary tumors," *Journal of Photochemistry and Photobiology B: Biology*, vol. 127, pp. 223–228, 2013.

[200] X.-J. Han, L.-F. Sun, Y. Nishiyama, B. Feng, H. Michiue, M. Seno, H. Matsui, and K. Tomizawa, "Theranostic protein targeting erbb2 for bioluminescence imaging and therapy for cancer," *PloS one*, vol. 8, no. 9, p. e75288, 2013.

[201] J. Condeelis and J. E. Segall, "Intravital imaging of cell movement in tumours," *Nature Reviews Cancer*, vol. 3, no. 12, pp. 921–930, 2003.

[202] S. Mallidi, S. Kim, A. Karpiouk, P. P. Joshi, K. Sokolov, and S. Emelianov, "Visualization of molecular composition and functionality of cancer cells using nanoparticle-augmented ultrasound-guided photoacoustics," *Photoacoustics*, vol. 3, no. 1, pp. 26–34, 2015.

[203] N. Beziere, N. Lozano, A. Nunes, J. Salichs, D. Queiros, K. Kostarelos, and V. Ntziachristos, "Dynamic imaging of {PEGylated} indocyanine green (icg) liposomes within the tumor microenvironment using multi-spectral optoacoustic tomography (msot)," *Biomaterials*, vol. 37, pp. 415 – 424, 2015.

[204] L. Kirscher, X. L. Deán-Ben, M. Scadeng, A. Zaremba, Q. Zhang, C. Kober, T. F. Fehm, D. Razansky, V. Ntziachristos, J. Stritzker, *et al.*, "Doxycycline inducible melanogenic vaccinia virus as theranostic anti-cancer agent," *Theranostics*, vol. 5, no. 10, p. 1045, 2015.

[205] J. A. Bertout, S. A. Patel, and M. C. Simon, "The impact of o2 availability on human cancer," *Nature Reviews Cancer*, vol. 8, no. 12, pp. 967–975, 2008.

[206] S. Yitta, B. N. Joe, D. J. Wisner, E. R. Price, and N. M. Hylton, "Recognizing artifacts and optimizing breast mri at 1.5 and 3 t," *American Journal of Roentgenology*, vol. 200, no. 6, pp. W673–W682, 2013.

[207] T. Bäuerle, D. Komljenovic, M. R. Berger, and W. Semmler, "Multi-modal imaging of angiogenesis in a nude rat model of breast cancer bone metastasis using magnetic resonance imaging, volumetric computed tomography and ultrasound," *JoVE (Journal of Visualized Experiments)*, no. 66, pp. e4178–e4178, 2012.

[208] J. Kim, S. Park, Y. Jung, S. Chang, J. Park, Y. Zhang, J. F. Lovell, and C. Kim, "Programmable real-time clinical photoacoustic and ultrasound imaging system," *Scientific reports*, vol. 6, 2016.

[209] E. Mercep, G. Jeng, S. Morscher, P.-C. Li, and D. Razansky, "Hybrid optoacoustic tomography and pulse-echo ultrasonography using concave arrays," *IEEE transactions on ultrasonics, ferroelectrics, and frequency control*, vol. 62, no. 9, pp. 1651–1661, 2015.

[210] F. M. Brochu, J. Brunker, J. Joseph, M. R. Tomaszewski, S. Morscher, and S. E. Bohndiek, "Towards quantitative evaluation of tissue absorption coefficients using light fluence correction in optoacoustic tomography," *IEEE Transactions on Medical Imaging*, vol. 36, no. 1, pp. 322–331, 2017.

List of Peer-Reviewed Publications

Journals and Magazines

[1] **S. Mandal**, X. L. Dean-Ben, N. C. Burton and D. Razansky, "Extending Biological Imaging to the Fifth Dimension: Evolution of volumetric small animal multispectral optoacoustic tomography.," in *IEEE Pulse*, vol. 6, no. 3, pp. 47-53, May-June 2015.

[2] **S. Mandal***, E. Nasonova*, X. L. Deán-Ben, and D. Razansky, "Optimal self-calibration of tomographic reconstruction parameters in whole-body small animal optoacoustic imaging," *Photoacoustics*, 2(3), pp.128-136.

[3] H. He, **S. Mandal**, A. Buehler, X. L. Deán-Ben, D. Razansky and V. Ntziachristos, "Improving Optoacoustic Image Quality via Geometric Pixel Super-Resolution Approach," in *IEEE Transactions on Medical Imaging*, vol. 35, no. 3, pp. 812-818, March 2016.

[4] **S. Mandal**, X. L. Deán-Ben and D. Razansky, "Visual Quality Enhancement in Optoacoustic Tomography Using Active Contour Segmentation Priors," in *IEEE Transactions on Medical Imaging*, vol. 35, no. 10, pp. 2209-2217, Oct. 2016.

[5] H.C.A. Lin*, R. Dutta*, **S. Mandal**, A. Kind, A. Schnieke and D. Razansky, "Advancing ovarian folliculometry with selective plane illumination microscopy," *Scientific Reports* 6, 2016.

[6] V. Ermolayev*, X. Dean-Ben*, **S. Mandal**, V. Ntziachristos, and D. Razansky, "Simultaneous visualization of tumour oxygenation, neovascularization and contrast agent perfusion by real-time three-dimensional optoacoustic tomography," *European Radiology*, 26(6), pp.1843-1851.

Indexed Conference Proceedings

[1] **S. Mandal**, X. L. Deán-Ben, and D. Razansky, "Automated calibration of temporal changes in the speed of sound in optoacoustic tomography," *Proc. SPIE,* vol. 8800. p. 88000K–88000K–5, 2013.

[2] **S. Mandal**, E Nasonova, XL Deán-Ben and D Razansky," Fast calibration of speed-of-sound using temperature prior in whole-body small animal optoacoustic

'*' indicates equal contributions

imaging", *Proc. SPIE 9323, Photons Plus Ultrasound: Imaging and Sensing 2015*, 93232Q (March 11, 2015)

[3] **S. Mandal**, P. Viswanath, N. Yeshaswini, X. Deán-Ben and D. Razansky, "Multiscale edge detection and parametric shape modeling for boundary delineation in optoacoustic images," *2015 37th Annual International Conference of the IEEE Engineering in Medicine and Biology Society (EMBC)*, Milan, 2015, pp. 707-710.

[4] H He, **S. Mandal**, A. Buehler, D Razansky, V Ntziachristos, "Geometrical super-resolution for planer optoacoustic imaging," *Proc. SPIE, European Conferences on Biomedical Optics 2015*, (June 21-26, 2015)

[5] P. S. Viswanath, T. Weiser, P. Chintala, **S. Mandal** and R. Dutta, "Grading of mammalian cumulus oocyte complexes using machine learning for in vitro embryo culture," *2016 IEEE-EMBS International Conference on Biomedical and Health Informatics (BHI)*, Las Vegas, NV, 2016, pp. 172-175

[6] H.C.A. Lin*, R. Dutta*, **S. Mandal**, A. Kind, A. Schnieke, and D. Razansky, "Light-sheet microscopy for quantitative ovarian folliculometry," *Proc. SPIE,* vol. 10043. p. 100430K–100430K–7, 2017.

Manuscripts in Review/ Preparation

[1] R. Dutta*, **S. Mandal***, H.C.A. Lin, A. Kind, A. Schnieke and D. Razansky, "Multispectral optoacoustic tomography enables non-destructive imaging of mammalian ovarian follicles for artificial reproduction," *Royal Society Interface,* (In review - submitted Nov 2016)

[2] J Prakash*, **S. Mandal***, D Razansky and V Ntziachristos, "Maximum entropy based non-negative optoacoustic tomographic image reconstruction." (In preparation)

List of Figures

Acronyms

AF	Autofocussing.
ANSI	American National Standards Institute.
ART	Artificial reproductive technology.
BCB	Brilliant cresyl blue.
BcL	B-cell lymphoma.
BTV	Bilateral total variation.
BW	Body weight.
CASP	Critical Assessment of protein Structure Prediction.
CG	Consistent Gradient.
CNR	Contrast to noise (ratio).
CoC	Cumulus oocycte complexes.
CT	Computed tomography.
DM	Dice (coefficient) metric.
DNA	Deoxyribonucleic acid.
DPBS	Dulbecco's phosphate-buffered saline.
FBP	Filtered back-projection.
FEM	Finite element model.
FMT	Fluorescence molecular tomography.
FoV	Field of view.
FVM	Finite volume model.
FWHM	Full width half maximum.
G6PDH	Glucose-6-phosphate dehydrogenase.
GoF	Goodness of fit.
I.V.	Intra-venous.
ICG	Indocyanine Green.
IMMI	Interpolated model matrix inversion.
IVF	In vitro fertilization.
Lipo-ICG	Liposomal Indocyanine Green.
LR	Low resolution.

LSQR	Least squares decomposition.
meanPD	Mean perpendicular distance.
MPE	Maximum permissible units.
MRI	Magnetic resonance imaging.
MSOT	Multispectral Optoacoustic Tomography.
NIR	Near infra-red.
OA	Optoacoustics.
OAT	Optoacoustic tomography.
OD	Optical density.
OPO	Optical parametric oscillator.
PCR	Polymerase chain reaction.
PET	Positron Emission Tomography.
POCS	Projection onto convex sets.
PSR	Pixel super-resolution.
RMS	Root mean square.
ROI	Region of interest.
SNR	Signal to noise (ratio).
SoS	Speed of sound.
SPIM	Selective plane illumination microscopy.
SR	Super-resolution.
ToF	Time of flight.
TUNEL	Terminal deoxynucleotidyl transferase (TdT) dUTP Nick-End Labeling.
USAF	United States Air Force (resolution phantom).
VCA	Vertex component analysis.
vMSOT	Volumetric Multispectral Optoacoustic Tomography.

Declaration

I hereby declare that the thesis submitted is my own unaided work. All direct or indirect sources used are acknowledged as references.
I am aware that the thesis in digital form can be examined for the use of unauthorized aid and in order to determine whether the thesis as a whole or parts incorporated in it may be deemed as plagiarism. For the comparison of my work with existing sources I agree that it shall be entered in a database where it shall also remain after examination, to enable comparison with future theses submitted. Further rights of reproduction and usage, however, are not granted here.
This dissertation was not previously presented to another examination board and has not been published.

Ich erkläre hiermit ehrenwörtlich, dass ich die vorliegende Arbeit selbständig angefertigt habe. Die aus fremden Quellen direkt und indirekt übernommenen Gedanken sind als solche kenntlich gemacht.
Ich weiß, dass die Arbeit in digitalisierter Form daraufhin überprüft werden kann, ob unerlaubte Hilfsmittel verwendet wurden und ob es sich – insgesamt oder in Teilen – um ein Plagiat handelt. Zum Vergleich meiner Arbeit mit existierenden Quellen darf sie in eine Datenbank eingestellt werden und nach der Überprüfung zum Vergleich mit künftig eingehenden Arbeiten dort verbleiben. Weitere Vervielfältigungs- und Verwertungsrechte werden dadurch nicht eingeräumt.
Die Arbeit wurde weder einer anderen Prüfungsbehörde vorgelegt noch veröffentlicht.

Subhamoy Mandal

Biography

Subhamoy Mandal (StM'04, GSM'08, M'16) is currently a DAAD PhD Scholar with the Chair of Biological Imaging at TU München, and the Institute of Biological and Medical Imaging at Helmholtz Zentrum München. He received his MS (by research) from the Indian Institute of Technology Kharagpur, and B.E. in Biomedical Engineering from Manipal University, Karnataka, India. His areas of interest are Medical Signal and Image Processing, Medical Imaging and DSP/GPU based algorithm design. He is a recipient of the prestigious DAAD PhD Scholarships and is a member of TUM Graduate School of Bioengineering.

Subhamoy is an active Member of IEEE, and is a recipient of Computer Society's Richard E. Merwin Student Scholarship. He was the 2013-14 Student Rep and AdCom member of IEEE Engineering in Medicine and Biology (EMB) Society, 2010-12 Chair, IEEE Education Society Student Activity Committee (IEEE EdSocSAC), and was awarded the IEEE Student Leadership Award (conferred by EdSoc) in 2013 for his contributions, He was the Founding Chair, IEEE EMB Student Club of IIT Kharagpur, which has been awarded the Best New Student Club/Chapter Award 2010 by IEEE EMBS Student and Member Activity Committee. He has been a Member of IEEE Ad-hoc Committee on Social Media Policy performing under the aegis of the IEEE Board of Directors, and also actively volunteered with the IEEE Student Branches at IIT Kharagpur(Treasurer 2009-10) and MIT Manipal.

Subhamoy has been closely associated with several corporate organizations including Philips, GE and Microsoft. During his internships with Philips BOP and the master's thesis, he has focused on developing low cost point of care technologies to address healthcare challenges of emerging economies. At GE Global Research his primary area of focus has been Magnetic Resonance Imaging (MRI) and its application in Brain Iron Quantification, leading to early diagnosis of Alzheimer's and other neurodegenerative diseases.

His goal is to achieve success in innovating technical and user friendly solutions using expertise of Biomedical engineering and domain knowledge of Medical Sciences by synchronized efforts in a collective venture.